AN INVESTIGATION INTO THE FRICTION STIR WELDING OF AL 6061 AND AL 6061/SiC/17.5p USING DIAMOND COATINGS

By

Tracie Prater

Thesis

Submitted to the Faculty of the

Graduate School of Vanderbilt University

in partial fulfillment of the requirements

for the degree of

MASTER OF SCIENCE

in

Mechanical Engineering

August, 2008

Nashville, Tennessee

Approved:

Professor Alvin M. Strauss

Professor George E. Cook

To my mother, grandmother, and Mrs. Beulah Hall

ACKNOWLEDGEMENTS

I would like to take this opportunity to briefly recognize the myriad of people and agencies which have helped me with this research during the paSt two years. My research advisors, Drs. Al Straus and George E. Cook; Dr. Jim Davidson and Mick Howell of the Diamond Fabrication Laboratory at Vanderbilt University; my labmates Paul Fleming, David Lammlein, Thomas Bloodworth, and Paul Sinclair; Andrew Bouchard for assistance with CAD; the Vanderbilt University machine shop; Estevan Bunker for the photos and much of the information on experimental procedure; Midwest Tungsten of Chicago, Illinois; sp3 for diamond coatings; DWA Composites of Chatsworth, California for donated material; NASA Space Grant, which provided financial support throughout this project; the NASA Academy program; Drs. Frank Six, Alan Chow, and Art Nunes at Marshall Space Flight Center in Huntsville, Alabama for the opportunities they have given me; Drs. Jerry Cook and Garrett Yoder, my undergraduate physics professors; my family, friends, and pets for their patience and support.

TABLE OF CONTENTS

LIST OF TABLES

Table Page

LIST OF FIGURES

LIST OF ABBREVIATIONS

Symbol	
fr	feed rate
Fx	Translational force
Fy	transverse force
Fz	axial force
Mz	Moment about z axis
k	thermal conductivity
ρ	Density
Cp	specific heat at constant pressure
T	Temperature
ω	rotational velocity (spindle speed)
YS	yield strength
UTS	ultimate tensile strength
CVD	Chemical Vapor Deposition
FEA	Finite Element Analysis
FEM	Finite Element Method

CHAPTER I

INTRODUCTION

1.1 Overview of the FSW Process

The Friction Stir Welding (FSW) process was developed by The Welding Institute (TWI) of Cambridge, England in 1991 [1]. FSW is a mechanical, solid-state joining process which has been proven as a viable joining method for many different joining configurations including lap joints, T joints, fillet joints, and butt joints [2]. FSW is currently employed in the railway, aerospace, and maritime industries. A pictorial representation of the steps in Friction Stir Welding process is provided in Figure 1. .

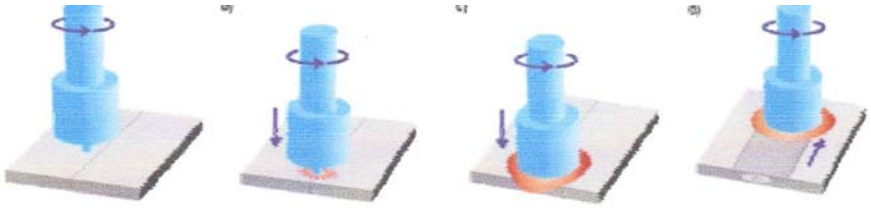

Figure 1 Illustration of FSW process [3]

In traditional FSW, a cylindrical steel tool rotates with an angular velocity, ώ, and is plunged into the material to be welded (referred to as the workpiece). This rotation generates a considerable amount of heat due to friction, resulting in the plastic deformation of the material. The rotating tool remains stationary while the workpiece is advanced by a table driven at a feed rate, f_r. f_r is usually specified in inches per minute

(ipm), while ώ has units of revolutions per minute (rpm). During an FSW process, the forces in the x, y, and z directions as well as the moment about the z axis are recorded. F_x is the translational force, F_y is the transverse force, and F_z is the axial force. Forces are measured in Newtons; the moment is in units of Newton-meters.

Friction Stir Welding has several distinct advantages over traditional arc welding. FSW generates no fumes, results in reduced distortion and improved weld quality for the proper parameters, is adaptable to all positions, and is relatively quiet. The major variables of interest in any FSW process are rotation (spindle) speed, travel speed (feed rate), tool orientation/position (tilt angle), plunge depth, tool material, tool geometry, and workpiece material [2].

1.2 FSW Tools

Most FSW tools consist of two distinct cylindrical sections: the shoulder and pin (in order of decreasing radius). A profile of such a tool is shown in Figure 2 with the parts of the tool clearly labeled.

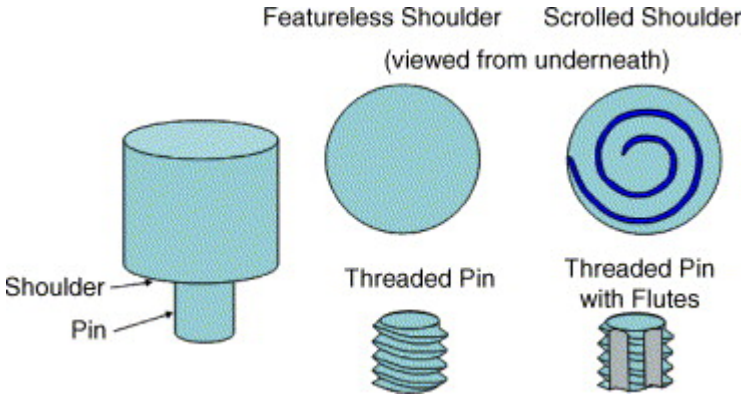

Figure 2 Typical FSW tool geometry [2]

The pin is plunged into the workpiece and the shoulder maintains contact with the workpiece surface. This shoulder contact functions to generate frictional heat as the pin "stirs" the material to be welded [2]. The shape, material, and structure of the FSW tool is dictated by the workpiece material, the desired quality of the weld, and the rotation and/or traversing speed. The geometry of the pin may be cylindrical, square, or even conical. Additionally, threads (similar to those found on a screw) may be machined into the pin to better facilitate material flow and prevent the formation of wormholes and other weld defects. In the welding of Aluminum or Aluminum alloys, the most common choice of tool material is steel: at the proper parameters, it produces good quality, robust welds and the tool has a slow wear rate. However, if a steel tool is used to weld more abrasive materials such as Metal Matrix Composites, tool wear becomes a significant issue due to the presence of abrasive particles and the strength of the material to be welded [2]. Tools made of more exotic materials such as Molybdenum (Mo), Tungsten (W), and Tungsten Carbide (WC) can be implemented to reduce or eliminate the tool wear and distortion which is common in steel tools at high forces and/or rotation speeds. The properties of some common FSW tool materials are summarized in Table 1.

Table 1 Tool Material Properties [4]

Material	Modulus of Elasticity (GPa)	Max. working temperature (Celsius)	Density (g/cm^3)
h-13 tool steel	195 Gpa	537	7.72
Molybdenum (pure)	330 Gpa	2617	10.22
Tungsten	400 Gpa	3370	19.2
Tungsten Carbide	650 Gpa	2800	15.7

The VU Welding Laboratory currently has tools of Molybdenum and h-13 steel. These are the base tool materials which will be considered in the subsequent investigation.

1.3 FSW Workpieces with Emphasis on Metal Matrix Composites (MMCs)

Currently, our laboratory work is exclusively concerned with the joining of Aluminum alloys in a flat plate configuration. This includes butt welds, lap welds, and T-joint welds. As previously discussed, steel tools with cylindrical geometries are sufficient for this work. An emerging area of FSW research is the welding of Metal Matrix Composites (MMCs). The structure of MMCs as well as the particular issues that arise when joining these materials will now be discussed in detail.

Aluminum Metal Matrix Composites (Al-MMCs) are used in many naval, military, and aerospace structures. A MMC material is comprised of two parts: a continuous metal matrix (the material in larger abundance, usually Aluminum) and the reinforcing particles dispersed throughout the matrix (typically SiC or B_4C in concentrations of 10-30%). Examples of MMCs with industrial applications are $6061/Al_2O_3/10_w$, $2618/ Al_2O_3/15_w$, $7075/ Al_2O_3/15_w$, 2124/SiC/25p, and 6092/SiC/17.5p. Al-MMCs are categorized according to a classification scheme developed by the Aluminum Association [5]. For instance, in $7075/ Al_2O_3/15_w$, 7075 indicates that the matrix is 7075 Aluminum, the Al_2O_3 designates that the reinforcement is Aluminum (III) Oxide, and the 15 specifies the percent of reinforcement present in the material. The p or w subscript indicates the form of the reinforcement; p corresponds to particulate, while w corresponds to whiskers [5].

The high-strength properties associated with MMCs make them difficult to join and are a limiting factor in the consideration of possible processes. Friction Stir Welding (FSW) has not traditionally been used for MMC welds because the strength and structure of the material results in significant tool wear and distortion in the finished weld (particularly in the heat-affected zone). Since the density of the reinforcement differs from the density of the matrix material (ex. $\rho_{Al} = 2.7$ g/cm^3 < $\rho_{SiC} = 3.2$ g/cm^3), the particles may tend to separate from one another during welding, resulting in inconsistencies within the finished weld [2]. This is referred to as macrosegregation. This is undesirable because it can lead to an unfavorable stress distribution in the weld, possibly resulting in structural deficiency or even failure. The high strength to weight ratio of MMCs and their resistance to wear, properties which make them attractive for structural applications, also make them difficult to join. When an MMC is welded using a standard steel tool, the result is usually excessive tool wear, cracking, and poor weld quality. Al-MMCs with high reinforcement percentages (greater than thirty percent) exhibit behavior typical of ceramics, making the welding of joints with these materials particularly difficult [2].

Friction Stir Welding (FSW) may prove a viable alternative to standard fusion welding of MMCs. Characteristics of MMC joints welded using fusion techniques such as TIG welding are usually characterized by incomplete mixing, porosity, and the presence of a Al_4C_3 phase. Previous studies of joining the MMCs 6092Al-SiC, A339-SiC, 6061Al-Al203, and 7093Al-SiC have demonstrated the high-quality welds can be produced using FSW, but in order for the process to be used on a large scale some mechanism must be developed to combat the problem of tool wear [2]. A study by

Nelson reports that even for an h13 steel tool heat treated to 52 on the Rockwell hardness scale, the tool wear is so dramatic that no threads are left after only 254 mm (ten inches) of weld [6]. The mechanism proposed in this study to reduce the aforementioned problem of tool wear is the use of a Molydenum tool coated with diamond by a Chemical Vapor Deposition (CVD) method. Previous work on FSW tool coatings and FSW of MMCs will be examined in the literature review of chapter II.

1.4 Diamond Coating by CVD (Chemical Vapor Deposition)

Diamond is an allotrope of Carbon. This means that diamond differs from Carbon only by virtue of its molecular configuration, which consists of two smaller face centered cubic (fcc) lattices offset by the vector (¼, ¼, ¼) from the two carbon atoms which form the structural basis [7]. The crystalline structure of diamond is shown in Figure 3.

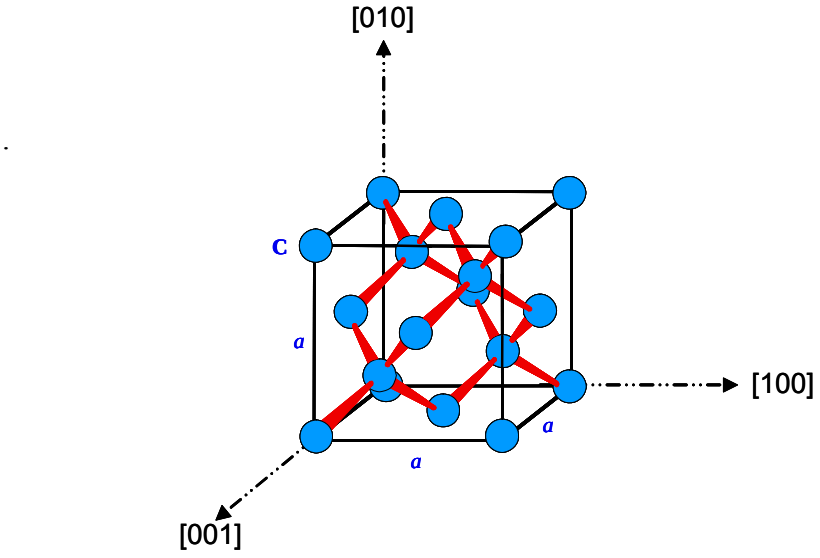

Figure 3 Unit cube for diamond. The lattice constant a = .356 nm [7].

The advantages of diamond as a coating are evident in its unique properties. The properties of diamond are summarized in Table 2.

Table 2 Properties of diamond [8]

Property	Diamond
Hardness	10 (Mohs scale)
Thermal Conductivity	20 W cm^{-1} K^{-1}
Thermal Expansion Coefficient	1.1 x 10^{-6} K^{-1}
Melting point	4000 ^{o}C

The most obvious advantage is diamond's extreme hardness, which has already been successfully exploited in many manufacturing applications to reduce tool wear. As we noted in section 1.3, previous studies have pinpointed tool wear as the primary limiting factor in FSW of MMCs. Diamond also has the highest thermal conductivity of any solid material at room temperature. This suggests that a diamond-coated FSW tool would function as a heat sink and that the majority of the frictional heat generated by the contact between the tool and the workpiece would be absorbed by the tool. The implications of this as well as any parametric adjustments which are needed to compensate for this effect will be addressed in subsequent chapters. Diamond's small thermal coefficient of expansion makes it ideal for temperature cycling. In the course of a weld cycle, the temperature which the tool encounters will vary from room temperature to upwards of 500 degrees Celsius (depending on workpiece material, tool material, travel speed, rotation rate, tool geometry, and length of weld). The cyclical heating and

cooling of the tool which occurs with each weld make coatings with low thermal expansion coefficients (such as diamond) good candidates for FSW applications.

The rarity and cost of natural diamond has spurred the development of deposition methods that can be used to "grow" diamond in a laboratory environment. The Chemical Vapor Deposition (CVD) process involves the synthesis of diamond particles from a carbon-based gas (in this case, Methane) through a complex reaction process. Once the reactants, CH_4 and H_2, are dispersed into the microwave chamber, the presence of high temperature conditions leads to the two governing activation reactions which appear in Figure 4:

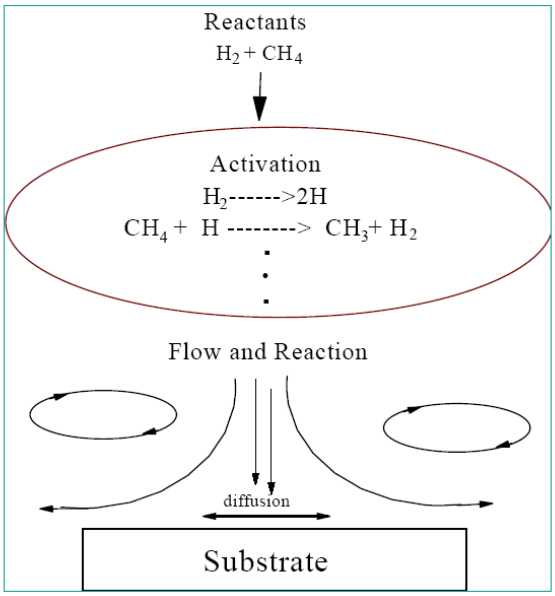

Figure 4 CVD reaction process [9]

In the first reaction, Hydrogen gas dissociates into 2 atoms of Hydrogen ($H_2 \rightarrow 2H$). Then Methane combines with a Hydrogen atom to yield a methyl hydrocarbon and Hydrogen gas ($CH_4 + H \rightarrow CH_3 + H_2$) [10]. Over time in the high-energy plasma

environment, these chemical interactions lead to diamond formation and deposition on the substrate. The exact mechanism(s) for CVD diamond coating is a subject of current research, as it is very difficult to characterize reactions which occur at such a minute level. One possible explanation for the diffusion/nucleation/growth process is shown in Figure 5.

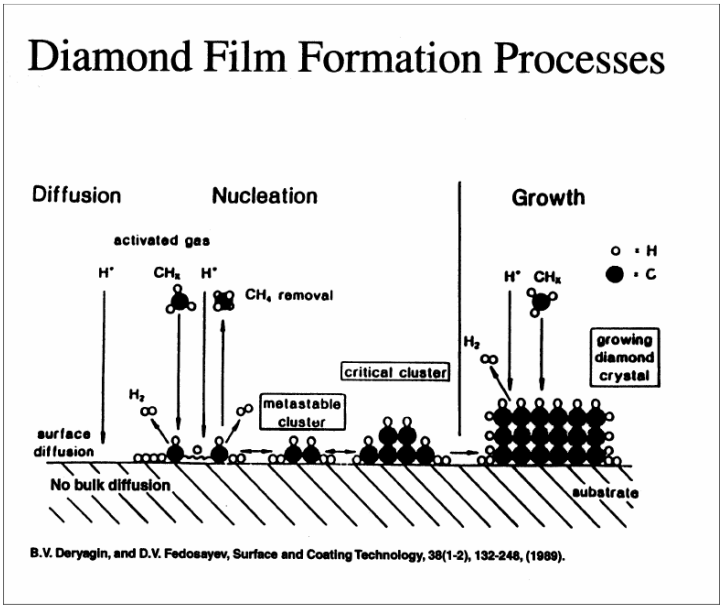

Figure 5 Diamond formation process [10]

In the model shown above, available Carbon coalesces into a carbide layer on the substrate surface, and the transport rate of Carbon is reduced [11]. A diamond nucleus is formed when the surface concentration has reached a "critical level" or the surface layer has grown to "critical size" [11]. Though it is a promising area of research, the specifics of the formation process lie beyond the scope of this study; our primary focus is the application of CVD technology to FSW.

The tools used in this report were coated using the Microwave (MW) Plasma Enhanced (PE) CVD machine in the Vanderbilt University Diamond Technology Laboratory. We additionally employed the services of sp3, a company which specializes in diamond coatings for industrial applications. A schematic of the CVD system used at the VU Diamond Laboratory is presented in Figure 6.

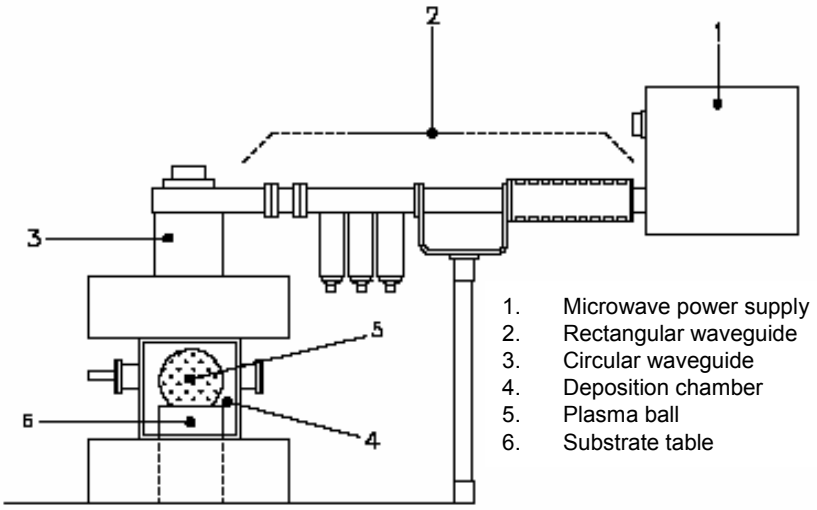

Figure 6 Schematic of MW CVD Reactor [12]

The microwave supplies power of 5000 W and interfaces with rectangular and circular wave guides through a dielectric window [12]. The substrate, which is placed on a small table inside the deposition chamber, experiences temperatures between 800 and 850 degrees Celsius during the coating process [12]. The pressure of the chamber is maintained at 120 torr [12]. The dimensions of the coating chamber necessitated a modification in our FSW tool design. The design adjustment which enabled tools to fit

inside the chamber for coating will be discussed at length in the chapter on experimental setup.

Additionally, the harsh environment of the deposition chamber imposes specific demands on the choice of substrate material. The substrate must be able to not just withstand the high temperatures and pressure associated with the coating process, but to do so without compromising the integrity of the base material. An ideal substrate candidate does not contain carbon (thus eliminating the potential of carbon carbon interaction) and has a coefficient of thermal expansion comparable to that of diamond [13]. The choice of substrate is critical: the quality of the resultant coating depends largely on the properties of the substrate itself.

1.5 Microstructural Zones

A typical FSW weld produces four distinct microstructural zones: the heat-affected zone (HAZ), the thermal mechanically affected zone (TMAZ), the weld nugget, and the unaffected zone (also known as parent material). The unaffected zone is exactly what its name implies: the material in this region is unaffected by the joining process and thus retains the mechanical properties associated with the workpiece material. The HAZ is characterized by a change in the microstructure due to heating and plastic deformation. The TMAZ is the site of plastic deformation. The weld nugget is the region of the weld in which the pin contacts the workpiece and thus is the area in which heat and plastic deformation are most pronounced. The weld nugget is also a site of recrystallization. A visual representation of the four weld zones appears in Figure 7.

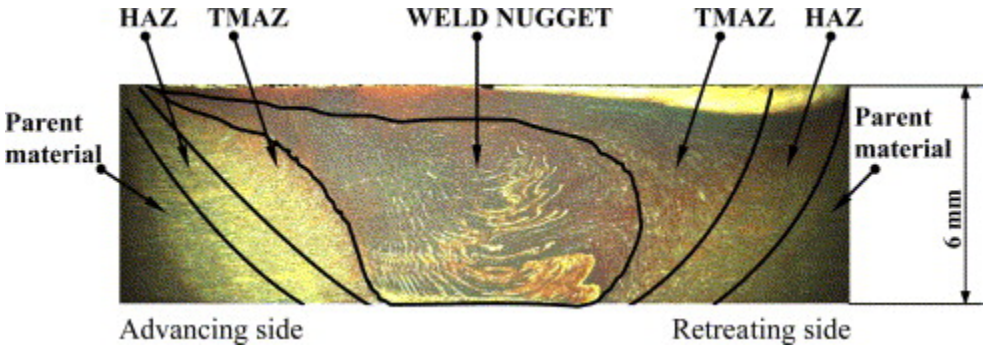

Figure 7 Weld zones in FSW: unaffected zone, HAZ, TMAZ, and weld nugget [14]

CHAPTER II

LITERATURE REVIEW

In this chapter, we will consider previous friction stir welding research on the parameterization of joining Metal Matrix Composites. Additionally, we will review studies concerning the use of coatings to reduce tool wear in the welding of superabrasive materials. Special emphasis is placed on joining Aluminum alloy series MMCs with varying percentages of SiC reinforcement, since this is the same material that was used in our research.

The motivation behind investigating friction stir welding as a method for joining MMCs is explicated in the Storjohann, et al. article "Fusion and Friction Stir Welding of Aluminum-Metal Matrix Composites," which provides a full assessment of the problems inherent in welding MMCs using traditional fusion techniques. Storjohann et al. utilize three different fusion methods to weld Aluminum composites reinforced with SiC whiskers: gas tungsten arc (GTA), electron beam (EB), and Nd-YAG continuous wave laser beam (LB). The authors compare these welds with those produced using FSW to determine what effect, if any, the solid state method has on weld quality. As noted in the literature pertaining to joining MMCs, the problem with fusion methods lies in the formation of an Al_4C_3 phase as a result of the interaction between the SiC reinforcement and molten aluminum. The authors postulate that the amount of Al_4C_3 present in a resultant weld is closely related to the peak weld temperature (i.e. a higher temperature produces a greater abundance of Al_4C_3). Since FSW is a lower temperature process that

does not melt the workpiece material, it is hypothesized that the FSW welds will have a smaller concentration of the deleterious Aluminum Carbide phase [15]. The materials Storjohann et al. used in his paper were 4 mm (approximately 5/32") thick plates of Aluminum 2124 alloy with twenty percent SiC whisker reinforcement. The heat input per unit length (referred to as the energy density) was 4200 J/in for GTA, 150 J/in for EB, and 2750 J/in for LB. The FSW parameters were a rotation speed of 500 RPM and a travel speed of 2 ipm. In analyzing the welds, the authors were primarily concerned with how the joining process would affect the orientation of the SiC reinforcements. It is their belief that favorable mechanical properties in the finished joint are largely dependent upon the post-weld distribution of the reinforcement particles.

In microstructural analyses of the fusion welds, Storjohann, et al. observe varying degrees of porosity in the HAZ region for all three methods. These porosities exhibit elongation in the x-direction, which the authors attribute to the tensile stresses the particles are subjected to during the weld cycle. In the fusion zone (FZ), there is complete dissolution of the SiC whiskers due to heating. The authors conclude that the formation of the Al_4C_3 phase is an inevitable consequence of fusion welding. The effect can be minimized by the careful control of heat input, but even the process with the lowest heat input per unit length (EB) shows evidence of Al_4C_3. The optical micrographs which appear in Figure 8 demonstrate the degree to which the Al_4C_3 phase occurs in the fusion welding processes considered by Storjohann, et al. It should be noted that even though the LB process has a smaller heat input than GTA, there is greater penetration due to the high laser absorption coefficient of the SiC whiskers.

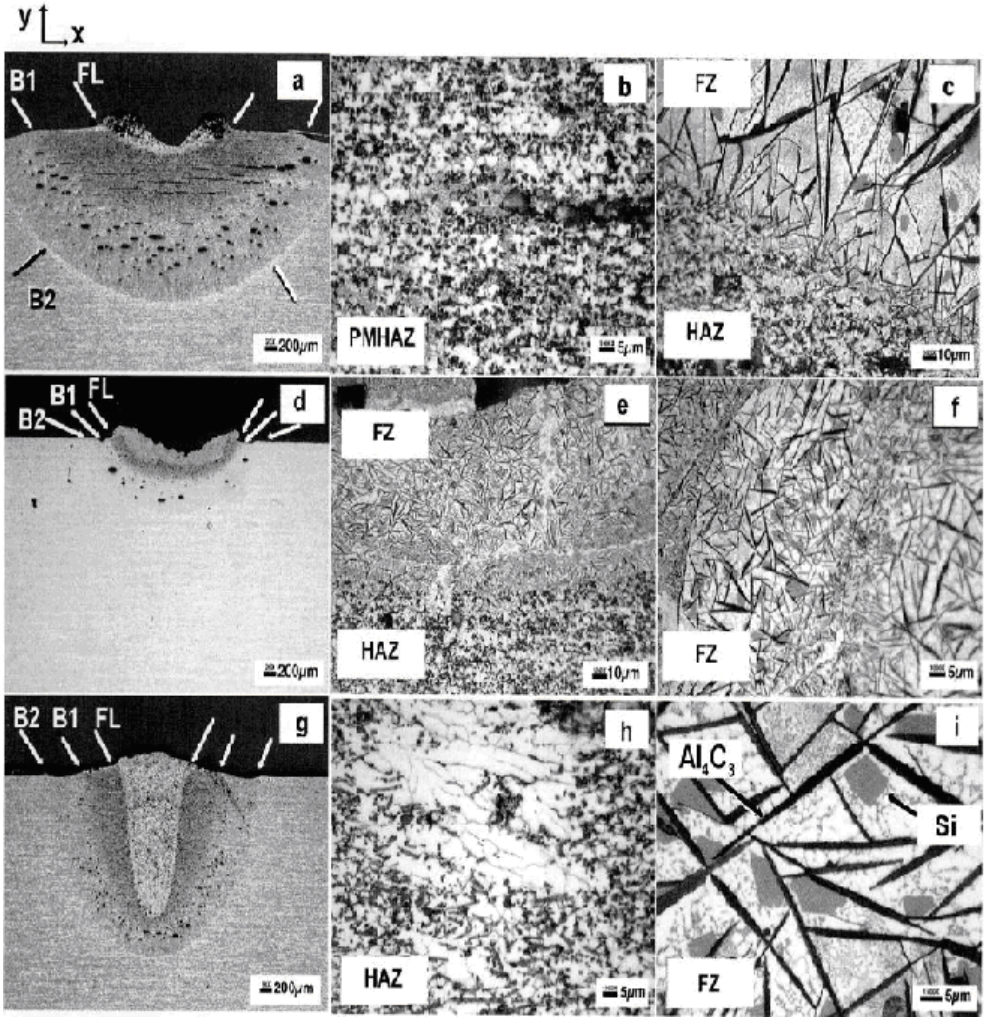

Figure 8. Fusion xelds of Al MMCs with SiC reinforcement. a-c are GTA, d-f are EB, and g-i are LB. The needle-like formations in c, f, and i are the Al_3C_4 phase [15].

The authors compare the above welds with those performed using FSW to gain insight into how and/or why FSW may offer an advantage over other processes. In the macrographs of the FSW welds which appear in Figure 9, Storjohann et al. point out that almost all the SiC whiskers are aligned in the direction of the weld line (z), which is also

the direction of metal flow. As we move away from the joint line, the whisker orientations gravitate towards the x-direction.

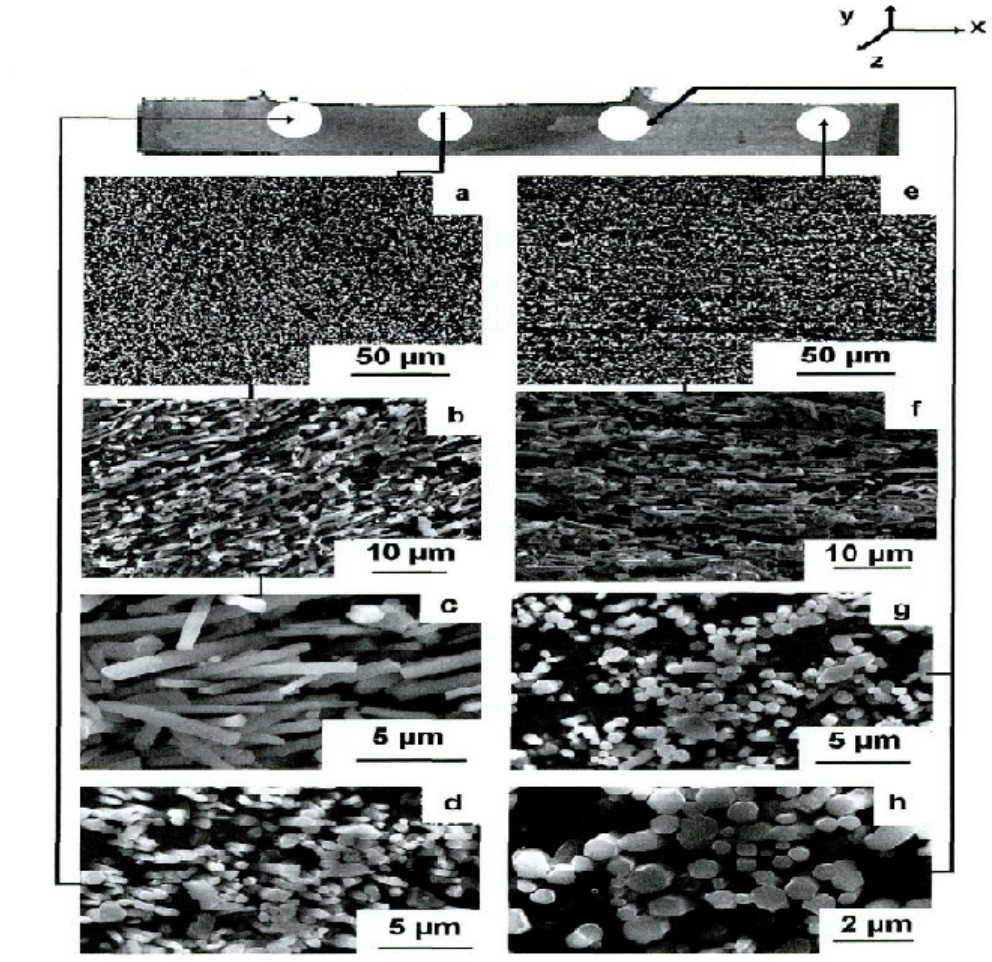

Figure 9. Spatial orientations of SiC whiskers in various regions of the FSW weld. Deep etching was done using an electrolytic process [15].

Storjohann et al. argue that the whisker alignment present in the FSW welds is preferred to that observed in the fusion welds. The more uniform microstructure of the FSW welds may indicate that there have been smaller changes to the parent material, which may translate into improved mechanical properties at the joint. Though the authors conducted no tensile testing to verify this hypothesis, they contend that Friction Stir Welding is well-suited for this application due to the absence of melted Aluminum in

the weld, which reacts with SiC in fusion welds to form the Al_4C_3 phase. Though work by Ellis has demonstrated that the formation of Al_4C_3 can be avoided in GTA welds, it requires careful control of the energy density [15]. Similarly, a study by Dahotre, et al. indicates that pulsing in laser welds reduces the accumulation of Al_4C_3 [16]. We should note that the Al_4C_3 phase is still observed in FSW welds of Al-MMCs, albeit it in significantly smaller quantities than in fusion welds. The degree to which this deleterious phase affects FSW joint properties is an area of current research.

In related research, Storjohann, et al. attempt to quantify the amount of Al_4C_3 formed as a function of weld temperature. They conclude that as the temperature increases and/or exceeds the melting point of the Aluminum, the reaction which transforms SiC into Al_4C_3 increases in rate. For this reason, it is desirable to keep the temperature of the workpiece below the melting point. This explains Storjohann's et al. previous assertion that solid state welding processes have great potential to lessen (or in some cases eliminate) the presence of Al_4C_3 in the completed joint.

The Storjohann paper, with its emphasis on Al_4C_3, establishes the motivation behind using FSW to join MMCs. The earliest feasibility studies on FSW of Aluminum MMCs with SiC reinforcements were conducted at NASA's Marshall Space Flight Center (MSFC) in the late 1990s. In a technical memorandum entitled "Friction Stir Welding for Aluminum Metal Matrix Composites" from 1999, Lee et al. assess using FSW to weld Aluminum MMCs reinforced with varying percentages of discontinuous SiC particulate (as opposed to the whisker reinforcements used in the Storjohann paper) [17]. Lee et al. reiterate the advantages FSW may offer for this application, placing particular emphasis on lower thermal energy requirements and the absence of undesirable

chemical reactions. Additionally, Lee points out that the FSW process is much less reliant on human/operator expertise than fusion methods such as GTA [17].

The NASA investigation used FSW tools with a 0.475" diameter shoulder and a 0.120" long pin with 10-24 left handed threads, whose dimensions were based on the results of computer simulations. These tools were used to weld flat-plate configurations of specimens measuring 0.125" in thickness. It is unusual for researchers to divulge tool geometry in publications, as this is often considered proprietary information and is closely guarded by the company or organization sponsoring the research. The tool for this report, however, was independently designed by the co-author, so disclosure is not an issue in this instance.

Since the authors anticipated tool wear in welding MMCs, the performance of tools made of h-13 steel hardened to 55 on the Rockwell Hardness scale were compared against tools of identical geometry coated with B_4C, a material which has a hardness value slightly less than that of diamond. The tools were used to perform butt welds of 6092 Aluminum alloy with 17.5 percent SiC particle reinforcement. The properties of this material, which are comparable to those of the MMCs used in our own investigation, are summarized in Table 3.

Table 3. Properties of Al 6092/SiC/17.5p [17].

Property	Value/Description
Material Descriptor	6092/SiC/17.5p–T6
Reinforcement Type	17.5% SiC Particulates
Density (lb/in^3)	0.101
Ultimate tensile strength (ksi)	67
Yield strength (ksi)	57
Elongation (percent)	8
CTE (ppm/F)	9.3
Hardness (Rockwell "B")	82
Temper	T–6

Lee et al. used the h-13 tools to generate a parameter set for the FSW of this particular MMC. They found that optimal welds were achieved at the parameters summarized in Table 4 on the following page. Welds performed with steel tools at these parameters were then compared with the welds performed with the coated tools to determine whether the B_4C coating reduced tool wear and/or enhanced joint properties. It should be noted that low rotation and travel speeds are typical for MMC welds. Slow speeds are required to generate the sufficient heating in the MMC workpiece that is required to produce a robust weld; the caveat is that this increased welding time also results in increased wear. In this regard, researchers must negotiate a compromise between the optimization of weld quality and the minimization of tool wear. Additionally, the excessive energy input associated with the necessary slower parameters may cause the workpiece to weld to the backing anvil, a problem encountered by Ding et al. in this study.

Table 4. Empirically derived parameters for FSW of Al 6092/SiC/17.5p [17].

FSW Parameters	Value	Description
Travel speed	4 ipm	Inch-per-minute horizontal speed
Rotating speed	1,350 rpm	Rotating speed of pin tool
Lead angle	2.5 deg	Pin tool's tilting angle from vertical plane
Plunge depth	0.010 in.	Shoulder length plunges below crown side
Penetration ligament	0.005 in.	Distance between tip of pin and backing anvil

A comparison of the weld macrographs showed that the coated tool reduced the coarseness on the crown side of the weld, an imperfection caused by the failure of the SiC particles to adhere to the Aluminum matrix in the finished joint. The increased hardness of the B_4C coated tool facilitates more favorable interaction of the matrix and reinforcement, but the coarseness reappears as the coating wears off. Macrographs of FSW welds with the coated and uncoated tools are presented, but little discussion is devoted to a qualitative comparative assessment. That authors do however, note evidence of particle segregation in the FSW microstructures. Figure 10 illustrates the HAZ microstructure at a magnification of 400X. The SiC particles in the finished weld, which appear darker than the surrounding material, are reduced in size and are concentrated at the edge of the HAZ (indicating that the action of the probe results in shape-alteration as well as dispersal).

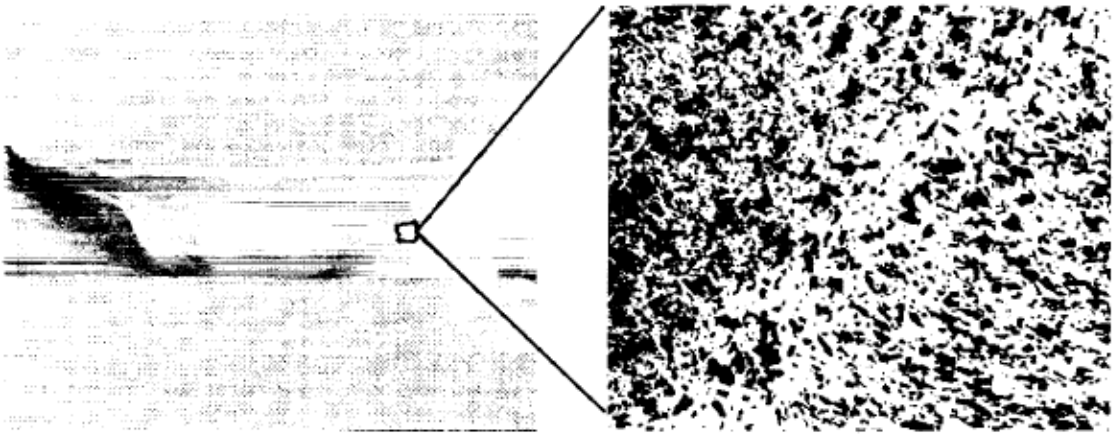

Figure 10 Particle distribution in HAZ [17]

The quantification of the particle segregation phenomenon in addition to its effect on the mechanical properties of the joint is beyond the scope of the NASA report. The correlation of particle segregation with tool geometry and/or weld parameters is a subject which requires further research.

The tensile strength measurements for welds performed using the uncoated and coated tools are compared in Tables 5 and 6.

Table 5 Average joint properties for welds using uncoated tool [17]

Joint Property	As-Welded	Heat Treated
Modulus (Msi)	11.13	12.28
Yield strength (ksi)	27.7	49.1
Tensile strength (ksi)	41.4	57.7
2-in. elongation (%)	2.49	2.07

Table 6 Average joint properties for welds using B_4C coated tool [17]

Joint Property	As-Welded	Heat Treated
Modulus (Msi)	10.44	12.83
Yield strength (ksi)	27.4	55.1
Tensile strength (ksi)	43.5	61.9
2-in. elongation (%)	2.72	2.00

In the as-welded condition, the coated tool results in an average tensile strength increase of only five percent. After heat treatment and age hardening, the average strength increase for the weld using the coated tool is approximately 7.3 percent. Joint efficiency is defined as the ratio of the tensile strength in the unwelded state to the tensile strength for the welded material. On average, the joint efficiency for the as-welded state is increased from 69% to 72.5% by using the coated tool. Post heat treatment, the joint efficiencies for welds performed using the uncoated and coated tools are 96% and 103%, respectively. Similarly, hardness values for the two weld sets were comparable For the parameters specified, it is apparent that the coating of the probe does not translate into increased strength or joint efficiency in the welds.

The issue of tool wear is only peripherally addressed in the NASA report. The authors state that after five feet of weld the tool wear is so severe that the probe must be adjusted or replaced. However, they do not elaborate on the variation of tool wear with weld parameters or compare the degree of wear for the coated and uncoated tools. There is also no evaluation of the effect of the coating on forces and torques. It is unclear whether the coated tool will significantly reduce any of the loads (typically 3000-10000 N, depending on tool geometry and weld parameters) associated with the FSW process.

The remainder of the NASA report focuses on the FSW of functionally gradient Al MMC to another composite, Al-Li 2195. Though the application for the work is never explicitly stated, the research may be related to the manufacturing of the architecture for the Constellation program, which requires circumferential joining of Al-Li 2195 composites by FSW methods. A functionally gradient material (FGM) is an MMC which has a high percentage reinforcement (often upwards of 50 percent) in the center of the plate, but significantly less near the weld line. The thickness of the FGM was 0.25 inches for all welds. All Al-MMC FGMs had a 50% SiC reinforcement at the center, but the percentage reinforcement at the edge varied from 5 to 50 percent. The Al-MMC FGMs were butt welded to Al-Li 2195 using a threaded probe with length 0.230 in and shoulder diameter 0.738 in [17]. The materials tested, weld parameters, and results are summarized in Table 7. The authors postulate that the probe breaks in the materials with higher levels of reinforcement at the edge may be due to extreme forces encountered during the course of the weld. These excessive forces can be attributed to the disparities in temperature and conductivity between the Al MMC FGM and the Al-Li 2195 composite

.

Table 7 Summary of results for butt welds of Al-MMC FGM to Al-Li 2195 [17]

Reinforcement at edge	Travel Speed (in)	Rotation Speed (rpm)	Plunge depth (in)	Results
5%	3.5	700	0.01	insufficient plunge depth
18.50%	3.5	700	0.015	Good surface finish
27%	3.5 to 4	700	0.015	probe broke 6 inches into weld
50%	3.5	700	0.015	probe broke after 1.5 inches of weld

As the findings above indicate, the "weldability" of a particular MMC may be a function of its percentage reinforcement. A feasibility study conducted on the joining of MMC flanges to Aluminum ducts concluded that FSW is practical only if the percentage reinforcement at the weld line is less than 25 percent by volume; beyond this, the material exhibits ceramic-like behavior, resulting in severe tool wear or breaking. This assertion is examined more thoroughly in related work conducted by Dr. Ravinder M. Diwan as part of an MSFC Faculty Fellowship [18]. Diwan's research report, entitled "Investigation of Friction Stir Welding of Aluminum Metal Matrix Composites" assesses the feasibility of long butt welds (up to 4 feet) of FGM MMCs. Such long welds are advantageous from a data acquisition standpoint in that they generate an abundance of steady-state load data and weldments for analysis. Since Diwan's experiments involve the joining of similar materials (both pieces to be joined are Al FGM MMCs with identical percentage reinforcements), the problems imposed by the dissimilar materials in the previous NASA study by Lee et al. may be avoided [17].

Diwan places the Al FGM MMCs into one of five categories based on their percentage of reinforcement. For categories I-III, the bulk of the plate is reinforced with SiC particles, while the edges are reinforced with Al_2O_3. Materials in categories IV and V have homogenous SiC reinforcement throughout. These classifications are summarized in Table 8.

Table 8 Categories of Al MMCs for Diwan study [18]

Category	% bulk SiC reinforcement	% Al_2O_3 edge reinforcement
I	40%	5%
II	40%	20%
III	40%	30%
IV	40%	0%
V	55%	0%

Welds were performed using a threaded tool (the dimensions of which are not disclosed) at a travel rate of 3 ipm, a rotation speed of 650 rpm, and a plunge depth of 0.01 inches. Additionally, three tool materials are considered: tool steel, ferro-tic, and satellite. Diwan found that T1 tool could successfully weld materials in categories I-III, but category IV resulted in the loss of threads (at the completion of the weld, an initially threaded probe would be reduced to a cylinder). Diwan states that Category V materials "appear to be unweldable" with any of the tools considered in his research.

Based on the microstructural analysis of the welds, Diwan concludes that acceptable welds for categories I, II, and III can be produced using any of the tool

materials considered. Diwan recommends further research into welding optimization of category I-III materials to reduce and/or eliminate any defects apparent in the microstructure. Category IV materials pose a significant problem: wear is severe regardless of the tool material and the probe is prone to break or fracture during the welding process. Though Diwan's research is only a broad study of MMC welds (the specifics of wear and microscopy observed during the investigation are scarce), it does corroborate the hypothesis that the weldability of an MMC is inversely proportional to its percentage reinforcement along the weld line. There also appears to be a threshold (around 50% reinforcement) beyond which MMCs cannot be welded using the proposed tools.

We now move away from feasibility studies and toward parameterization and the characterization of microstructural behavior for a range of composite materials. One such composite material that has been a focus of recent welding research is Al 6061/Al_2O_3/20p (which was previously considered by Diwan). In the paper "Friction stir welding of an AA6061/ Al_2O_3/20p reinforced alloy," Marzoli et al. establish a working envelope for this material and assess how joint efficiencies and microstructures are impacted by the choice of parameters [19]. Marzoli et al. performed FSW butt welds of the reinforced alloy using a tool with a 0.75" diameter shoulder and 0.3" diameter probe. The probe length, geometry, and tool material are not specified. The experimental weld matrix constructed by Marzoli, et al. appears in Figure 11. Spindle speed is plotted on the y-axis, while travel speed (in mm/min) appears on the x-axis. The blue circles indicate the parameters which produced a defect-free weld. Note that the operating window is narrow, including only rotation speeds from 475 rpm to 700 rpm and travel

speeds from 150 mm/min (approximately 6 ipm) to 300 mm/min (12 ipm). This welding envelope of slower parameters is characteristic of composite materials, which require increased energy input. The triangles represent a "process limit" beyond which not enough plastic deformation occurs to produce an acceptable weld. The red squares denote the robotic limits of the welding apparatus.

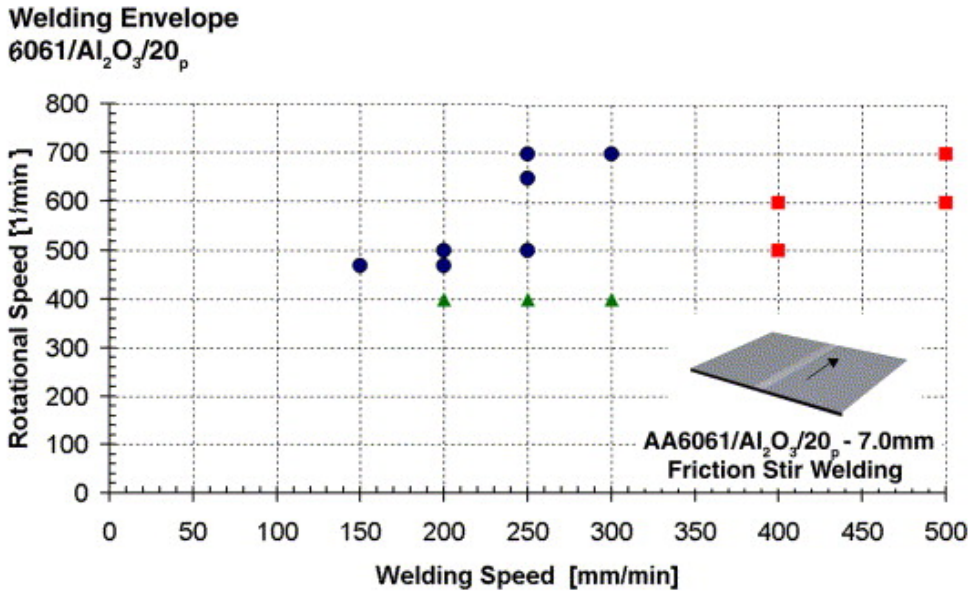

Figure 11 Welding envelope for 6061/Al_2O_3/20p [19]

To record temperature cycles, six type K thermocouples were embedded in the workpiece at increments of 0.4" and a distance of 0.6" from the weldline. A schematic of the thermocouple configuration as well as a plot of average temperature versus time is shown in Figure 12. The small length of weld (approximately 3 inches) calls into question the accuracy of the temperature profiles, as it is difficult to obtain robust steady state data for such a short weld. The choice of the smaller workpiece dimensions was most likely dictated by cost considerations.

The highest temperature, 250 degrees Celsius, is observed at T1, the thermocouple positioned closest to the start of the weld. This is because the higher energy input required to plasticize the material necessitates a gradual increase in welding speed. For instance, if the steady state travel speed is specified as 5 inches per minute, the tool will enter the weld at a slightly lower travel rate and "ramp up" to the steady state value. This is a common experimental technique in FSW and one we employ in our own laboratory work.

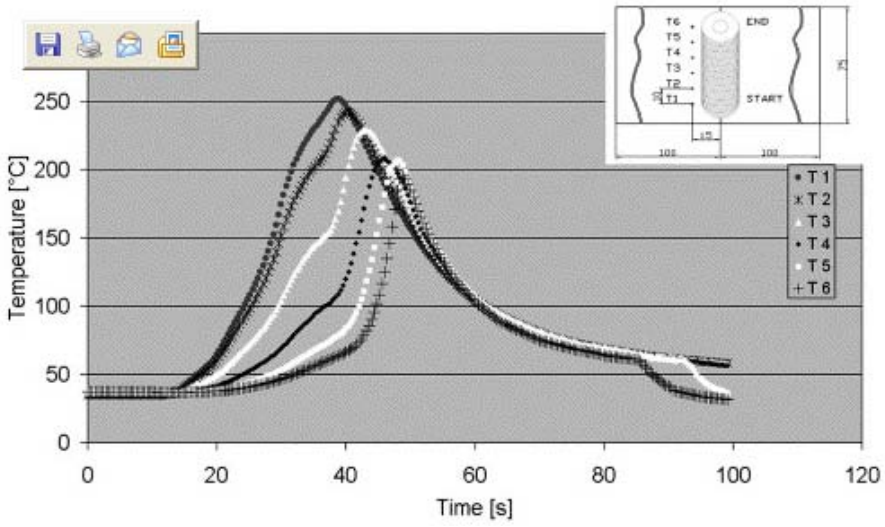

Figure 12 Thermal cycles [19]

Overall, the macrographs reveal only partial recrystallization, which can be attributed to the inhibition of material flow by the reinforcement particles. A wider nugget and TMAZ is a product of excess heat input There is also evidence of the formation of a precipitate (possibly an Al_2Cu phase or portions of the Al_2O_3 particles which have been scraped away by the tool). Particle distribution curves generated using ImageC software confirm the observations of Lee et. al. [17] In the finished weld, the

reinforcement particles are smaller and more rounded than in the parent material. Marzoli postulates that this reduction in particle size which comes about as a result of friction stir welding may actually function to enhance material properties.

Mechanical tests were used to assess whether the anomalies observed in the macrographs have any significant effect on weld integrity. Average yield strength (YS) and ultimate tensile strength (UTS) for the joints are compared in Table 9. Although the joint efficiency values are probably adequate for many industrial applications, they could be increased further by post-weld heat treatment. The authors note that all welds failed in the heat-affected zone; the relative weakness of the HAZ was corroborated by the results of microhardness testing across the joints.

Table 9 Summary of Tensile Test Results [19]

	YS (ksi)	UTS (ksi)
Base Al 6061/$A_{l2}O_3$/20p	40.18	51.49
Welded Al 6061/AL_2O_3/20p	33.94	36.4
Efficiency (%)	84.4	70.7

While the Marzoli research presents a good overview of the parameterization of FSW for MMCs, a more rigorous treatment of the effects of FSW on material microstructure and mechanical properties is presented by L. Ceschini in reference [20]. Ceschini considered butt welds of Aluminum 6061 reinforced with 20% Al_2O_3 particulate using a threaded tool with a 0.78” diameter shoulder and a 0.3” diameter pin (a geometry nearly identical to that used in the Marzoli paper). Samples from the cross-sections of the

welds were polished and etched using Keller's reagent. Subsequent measurements of surface roughness observed higher roughness values along the weld zone which can be attributed to shoulder contact. A close-up of an FSW welded joint is presented in Figure 13b. The labels L and T correspond to the longitudinal and transverse directions, respectively.

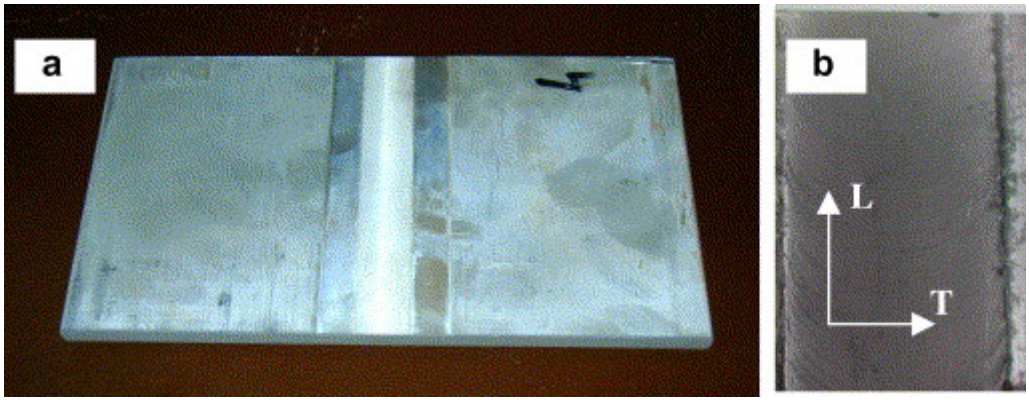

Figure 13 a) Butt weld of Al 6061/Al2O3/20p b) close-up of joint surface [20]

Although Ceschini et al. do not report the parameters the welds were performed at, it is presumed that they were chosen based on a previous parameterization study, since all welds were reported to be free of defects. Data compiled using the software Image Pro-Plus corroborates the observations of Marzoli et al. that FSW results in a significant decrease in particle size [19, 20]. In the Ceschini study, the average area of the particles decreased by approximately half, while their length was reduced by 42%. Additionally, particles in the weld zone are rounder than those in the parent material: Marzoli defines a shape factor which is 2.1 in the base material, but reduces to 1.9-2.0 in the weld zone [19]. It was also observed that FSW decreases the grain size of the Al 6061/Al_2O_3/20p by a factor of 1.5. Ceschini postulates that this smaller reduction in grain size

(unreinforced Al 6061 experiences a tenfold reduction in grain size after undergoing FSW) is due to the already fine microstructure of the composite material [20].

Tensile tests were performed in compliance with ASTM standards and strain was measured using an extensometer. On average, the ultimate tensile strength was 72% that of the parent material (this value for joint efficiency is consistent with the results of Marzoli tabulated in Table 9). Figure 14, taken from Ceschini, compares the stress-strain curves for the parent material and its FSW-welded counterpart.

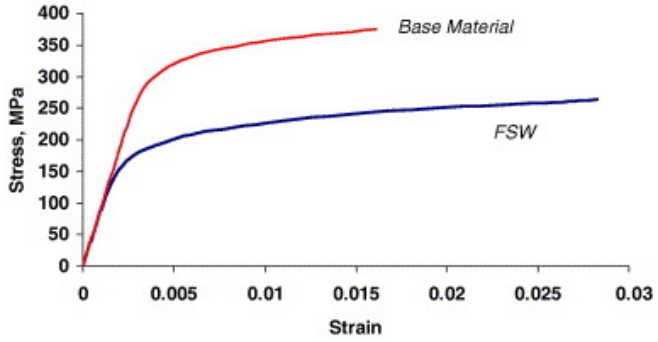

Figure 14 Stress-strain curves for unwelded and welded Al 6061/Al_2O_3/20p [20]

The constitutive relationship between stress (σ) and strain (ε) is $\sigma = k\,\varepsilon^n$, where n is the strain hardening exponent and k is a material-specific constant. From the plot in Figure 14 it is apparent that the FSW joined material has a larger value of n than its parent material, a result which implies that the FSW joint is able to withstand greater strain hardening. Ceschini relates this variation in n to the reduction in particle size: the reduced area of the reinforcement particles in the joint contributes to increased ductility, which in turn prolongs elongation.

Ceschini also subjected the welded samples to low-cycle fatigue tests. The results of these tests indicated that fatigue life was reduced in the FSW joints, an outcome that is consistent with the previous comparison of joint efficiency for the unwelded and welded samples. For low strain amplitudes, the fatigue life of the base material was twice as long as that of its FSW counterpart. For high strain amplitudes, the life span of the base material reached ten times that of the welded joint. Based on the plots of hysteresis loops at these different strain amplitudes, Ceschini concludes that the FSW composite undergoes increased plastic strain. He contends that this amplified strain, in conjunction with the non-homogeneity of the MMC, is responsible for the reduced fatigue life of the FSW joint.

Ceschini also examined the fracture surfaces after the fatigue tests had been performed. He proposes that there are three principal causes of fracture in the joint: I) fissuring of the reinforcement particles, II) desolidification along the particle/matrix boundaries, and III) void formation and enlargement within the matrix (a result of the aforementioned desolidification). SEM micrographs reveal that a type I fracture occurs in areas with larger particles, while distributions of smaller particles along the weld line primarily produce fractures of types II and III. Ceshini provides qualitative data in the form of micrographs to substantiate these observations, but does not characterize how fracture mechanisms are affected by weld parameters or tool geometry.

A comparable evaluation of the fracture behavior of Al 6061/Al_2O_3/20p is presented in the Cavliere et al. paper "Friction Stir Welding of Ceramic Particle Reinforced Aluminum Based Metal Matrix Composites." Though Cavalierie et. al. opt not to disclose tool dimensions (for this reason it may be misleading to directly compare

their results with those of the Ceschini study), they specify the tool rotation speed as 800 RPM and the travel rate as approximately 2 inches per minute. They record a slightly higher joint efficiency (84%-87%) than was reported in previous literature; this increased efficiency may be ascribed to the choice of weld parameters or the (unspecified) tool geometry used in the study. An examination of the microstructure of the welded samples reveals fracture behavior consistent with that characterized by Ceschini in reference [20]. Particle fracture along the matrix/particle interface (Ceshcini's "type II" fracture) can be seen clearly in Figure 15.

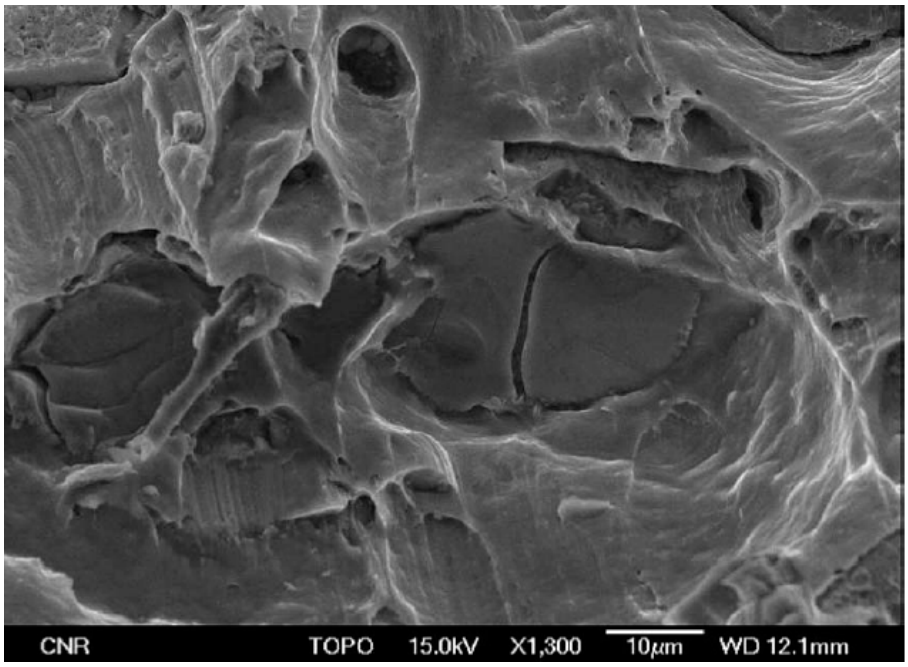

Figure 15 Particle fracture in FSW Al 6061/Al_2O_3/20p [21]

Similarly, the voids which may form in the matrix as a result of desolidification (and may initiate the "type III" fracture) are visible under magnification in Figure 16.

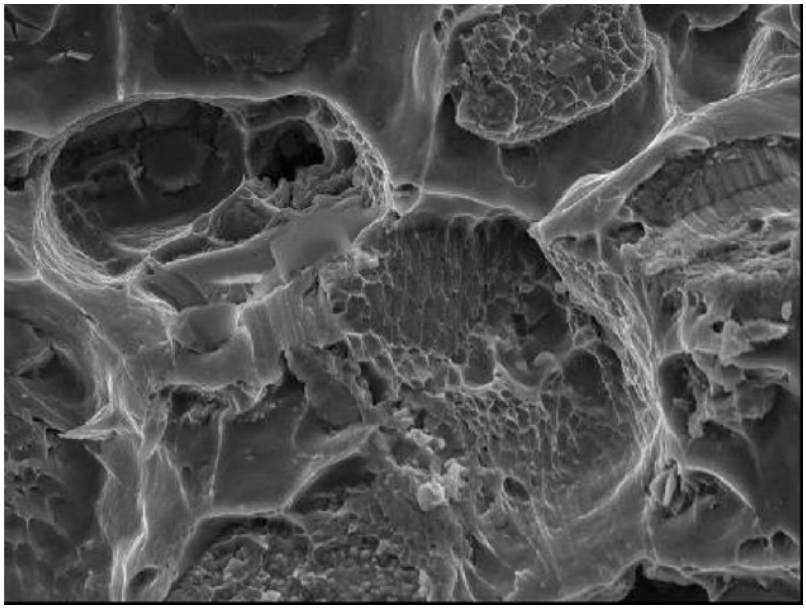

Figure 16 Voids in FSW Al 6061/Al_2O_3/20p [21]

Cavaliere considers a longitudinal section of the weld, observing that the amount of particle fracture is greatest along the centre and decreases "through the TMAZ and into the parent material" [21]. Interestingly, fracture occurs most often in the TMAZ, which Cavaliere postulates is an indicator of "very good plasticity properties [in the weld with] respect to the parent material" [21]. Cavaliere et al. explain this improved mechanical response along the weld line in terms of recrystallization: the strong centre of the weld is comprised of very fine dynamically recrystallized grains which are created by the stirring of the tool. As we move away from the weld centre, the grains are only partially recrystallized, resulting in decreased mechanical stability.

Although a substantial portion of the literature considered thus far has been devoted to 6000 series Aluminum Metal Matrix Composites with Al_2O_3 particle reinforcement, it is not without precedent to assume that the mechanical and microstructural behavior of this material in the as-welded state is analogous to that

exhibited by the composite investigated in our study (Al 6092/SiC/17.5p). In fact, the overall trends reported in the NASA study of Al 6092/SiC/17.5p are observed for nearly every variety of Aluminum MMC: severe tool wear, maximum joint efficiencies in the range of 70-80%, a narrow window of operating parameters, and changes in the pre and post-weld size and distributions of the reinforcement particles. It should be noted that although the magnitude of these phenomena may vary with weld parameters, tool geometry, and/or the type and amount of reinforcement, we can expect to detect them to some degree in the FSW of any composite material.

We will now consider two studies that are specific to Aluminum MMCs with SiC particle reinforcement. The first is an article by A.H. Feng et al. entitled "Effect of microstructural evolution on mechanical properties of AA2009/SiCp composite," which examines the effects of FSW on the Silicon Carbide reinforcement particles as well as the formation of precipitates within the weld nugget [22]. Feng et al. performed butt welds of ¼" Al 2009/SiC/15p plates using a threaded steel tool with a 1 inch diameter shoulder and .31 inch diameter probe. Samples were welded at 600 rpm at a travel speed of 2 ipm; a post weld heat treatment was subsequently used to harden samples to the T4 condition. Feng et al. used scanning electron microscopy (SEM) to capture images of the material microstructure before and after welding. From the SEM image of the parent material which appears in Figure 17a, it is apparent that the pre-weld state is characterized by "nonuniformly distributed SiC particles and coarse grains" [22]. Figure 17b shows the microstructure of the FSW joint: the particle distribution is more homogenous and the particle size has decreased by an average of 22 percent (as compared to the base material).

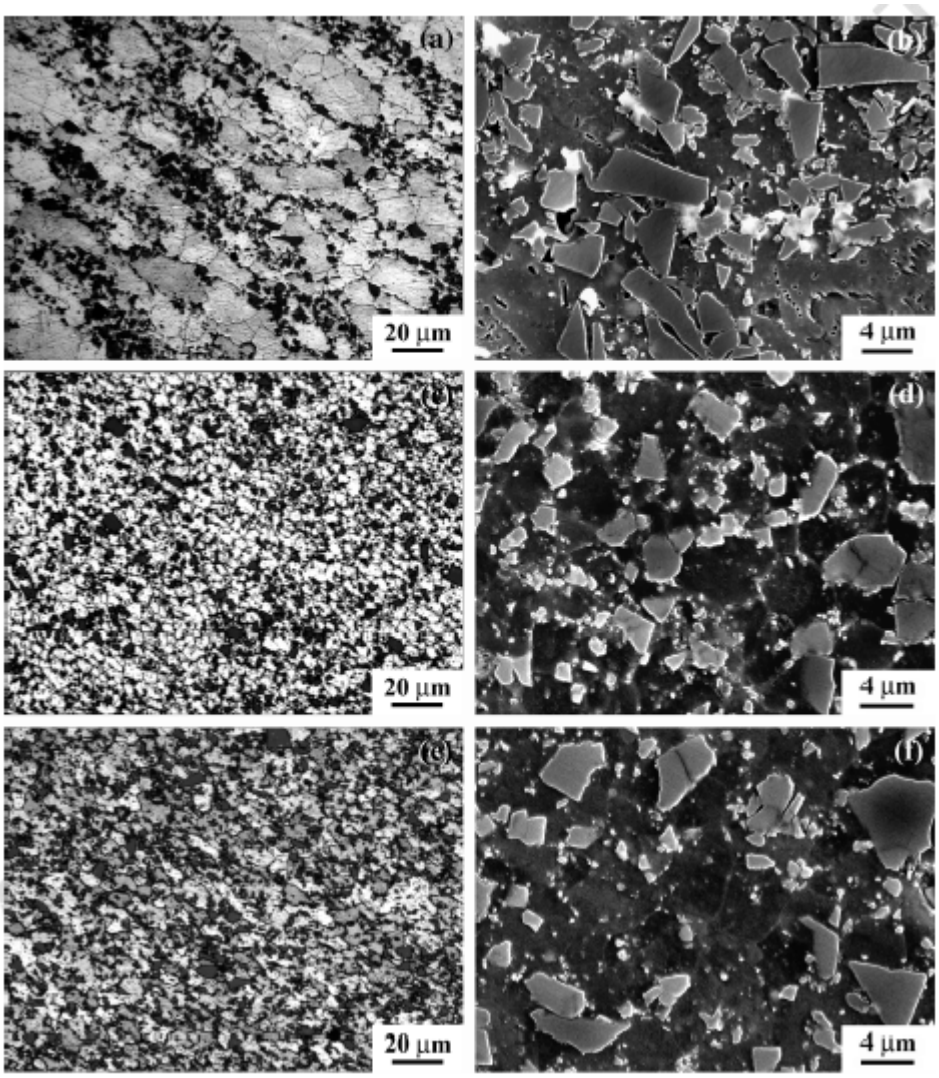

Figure 17 a) SiC particles in parent material (average size 5.4 μm) b) SiC particles in FSW joint (average size 4.2 μm) [22]

X-ray diffraction reveals the presence of two precipitate phases in the as-extruded material: Al_2CuMg and $CuAl_2$ (the latter corresponding to the theta phase which Storjahnn, et. al. found to be the principal hindrance to fusion welds of MMCs). Post FSW, there are no traces of $CuAl_2$ in the weld nugget. Since the overall effect of the theta phase is to weaken the joint, this observation corroborates Storjahnn's hypothesis that FSW welds of MMCs should in general be stronger than their fusion-welded

counterparts. Feng et al. do detect a θ'' phase (another form of the $CuAl_2$ precipitate), the magnitude of which is increased by post-weld heat treatment. However, Feng et al. do not characterize what effect, if any, this θ'' phase has on weld integrity or how its formation varies with weld parameters

The Feng research is significant in that the researchers were able to produce welds which surpassed the parent material in both yield strength (YS) and ultimate tensile strength (UTS), a result which had been lacking in previous research. In the best cases recorded by Feng, the FSW process increases the yield strength of the material by approximately fifty percent. Interestingly, the as-FSW joint loses some of its strength by virtue of the heat treatment process. When both the extruded and FSW composite are in the T4 condition, the YS and UTS of the parent material slightly exceeds that of the friction stir weld (this strength reduction is attributed to increased formation of the Cu_2FeAl_7 phase). These results are shown explicitly in Figure 18, which compares the UTS, YS, and elongation of Al 2009/SiC/15p pre and post weld.

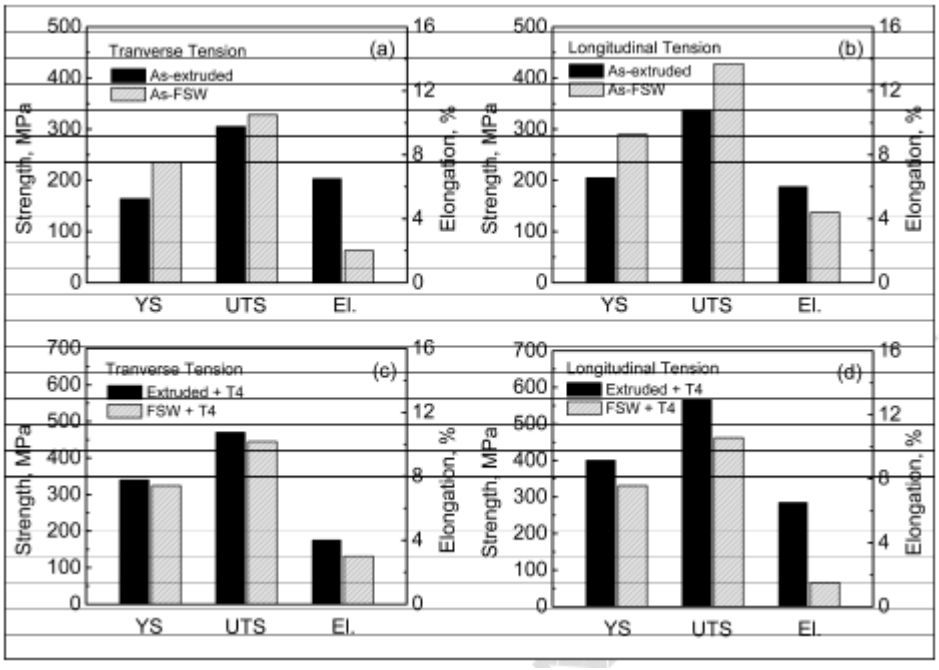

Figure 18 Comparison of yield strength, ultimate tensile strength, and elongation in transverse and longitudinal directions for as-extruded and as-FSW (top half) and as-extruded T4 and FSW T4 (bottom half) [22].

Feng discusses the microstructural evolution of the FSW composite at length. Since most of his analysis is beyond the scope of our own experimental investigation, we will summarize only the most apposite points. Feng contends that the FSW process enhances the SiC particle distribution. The rotation of the tool results in a "rounding off" of the particles, reducing and/or eliminating sharp edges which could produce stress concentrations. The recrystallization method by which the grain size reduction occurs is a matter of ongoing theoretical and experimental research. Although there are several proposed mechanisms in the literature, Feng seems to favor dynamic recrystallisation (DRX), based on the substantial decrease in grain size from the parent material to the nugget zone which is observed in FSW. In related research, Humphreys and Hatherly have developed a predictive model for post-weld grain size, D, as a function of volume

fraction, Fv, and initial particle diameter, d: $D = dFv^{-1/3}$ [23]. From this simple relationship, some obvious trends emerge: 1) the resultant FSW grain size is directly proportional to the grain size of the parent material and 2) the post weld grain size decreases with increasing volume fraction. When Feng et al. apply the Humphrey/Hatherly model to their research on 2009/SiC/15p, they find that it over-predicts the FSW grain size by approximately sixty percent. Feng ascribes this to the model's failure to account for the formation of precipitate and diffusion phenomena. Klug, et. al. have proposed an experimentally-based model to estimate the amount of Cu_2FeAl_7 formed in composites [24]. The Klug equation relates the intensity of fraction lines in XRD analysis to phase weight fractions (which can be obtained through mass spectroscopy). The limitation of the Klug model lies in its dependence on tool wear, a variable that is paramount to joining of MMCs yet is noticeably absent from the Klug formulation. Feng suggests that the Klug equation is most appropriate is best suited for scenarios in which tool wear is minimized by the use of "wear-resistant tool materials" or abrasive coatings [22].

A characterization of tool wear in an Aluminum material reinforced by SiC was completed by G.J. Fernandez and L.E. Murr of the University of Texas at El Paso. Fernandez and Murr performed butt welds of MMCs using a threaded probe of diameter 0.25" and measuring 0.147" in length (the probe length is smaller than usual to correspond to the reduced plate thickness of 0.157"). Rotation speeds considered in the study were 500, 750, and 1000 RPM; travel speeds were fixed at 25.8 and 14.2 IPM. Tool wear of the probe was measured using an optical technique in which the post-weld probe shapes in magnified photographs were cut out and compared with the original

probe shape [25]. Tool wear could then be expressed quantitatively in terms of volume consumption. Figure 19 shows the plot of probe wear as a function of travel distance for rotation speeds of 500, 750, and 1000. It is clear that wear is most dramatic at 1000 RPM, a result which corroborates the results of an earlier study by Prado et al. on Al 6061/Al_2O_3/20p [26].

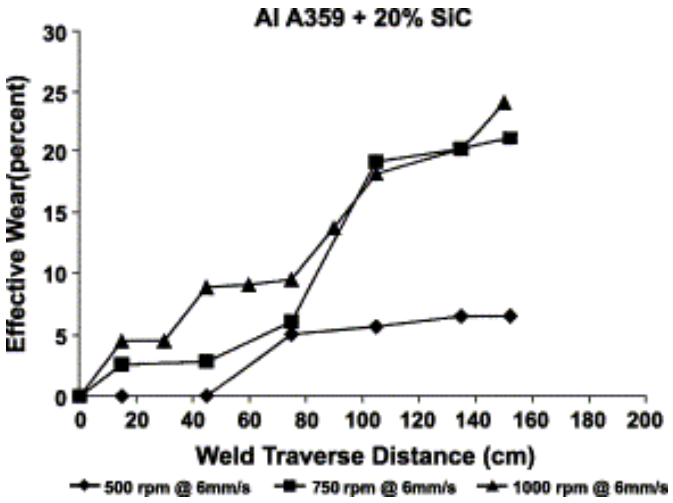

Figure 19 Wear versus traverse distance for 500, 750, and 1000 RPM. Travel speed was held constant at 14.2 IPM [25].

The evolution of the tool shape for the three rotation speeds is shown in Figure 20. While the remnants of threads are still visible after welding at 500 and 750 RPM, the 1000 RPM parameter results in complete erosion of the threads, ultimately creating a smooth cylinder.

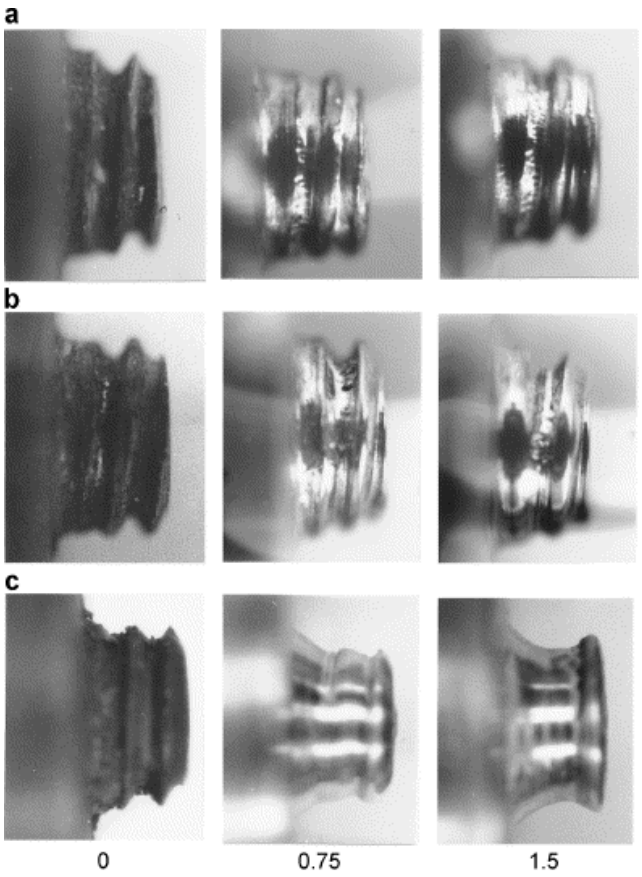

Figure 20 Sequence of probe wear for a) 500 RPM, b) 750 RPM, and c) 1000 RPM as a function of travel distance in meters [25].

The complete plot of probe wear for the range of parameters considered is shown in Figure 21. From the graph, Feng discerns that the parameters which minimize wear are a rotation speed of 500 rpm and a travel speed of 24 in/min. At these conditions, wear is less than 10% (as compared to 30% for the worst case of 1000 RPM and 2.4 IPM).

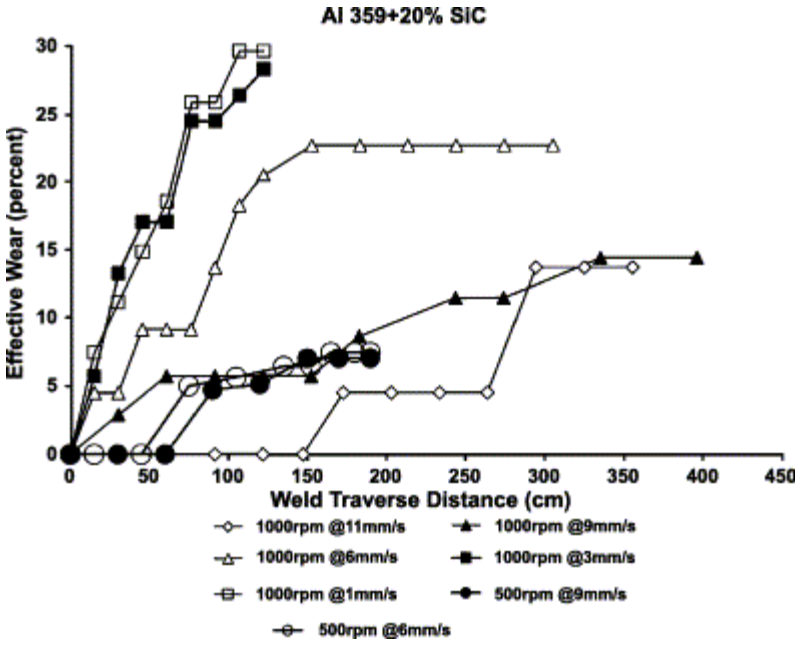

Figure 21 Wear for Al 359/SiC/20p for a range of parameters [25]

Feng does not present tensile test data for the parameters displayed in Figure 21. Although welds with higher travel speeds result in less wear, there may be too little plastic deformation at these parameters to create a strong weld. Herein lies the compromise that must be negotiated in joining MMCs: welding speeds must be slow enough to generate sufficient plastic deformation, yet fast enough to mitigate severe tool wear.

Feng notes that the wear trendlines for the parameters considered tend to plateau after a certain traverse distance. There is thus a threshold point beyond which no more wear occurs, which Feng refers to as the self-optimized shape. Based on their observation that "even partial thread removal decreases tool wear," Feng et al. argue that featureless tools are most efficient for FSW of MMCs. The analysis of the post-weld SiC distribution supports this hypothesis: once the threads have been eroded, there is reduced

contact of the tool with the reinforcement particles, resulting in a reduction of wear. This can be seen clearly in the frequency plots of Figure 22, which demonstrate that the mean particle diameter δ is reduced 25 percent by the threaded probe (from 4.1 μm to 3.1 μm), but only 7 percent by the smooth, worn probe. The implication is that "there is considerable particle attrition for the initial high-wear condition [threaded probe].....while at the end of welding, where the pin tool is becoming shape-optimized, there is only a slight reduction in mean particle size from the base material" [25].

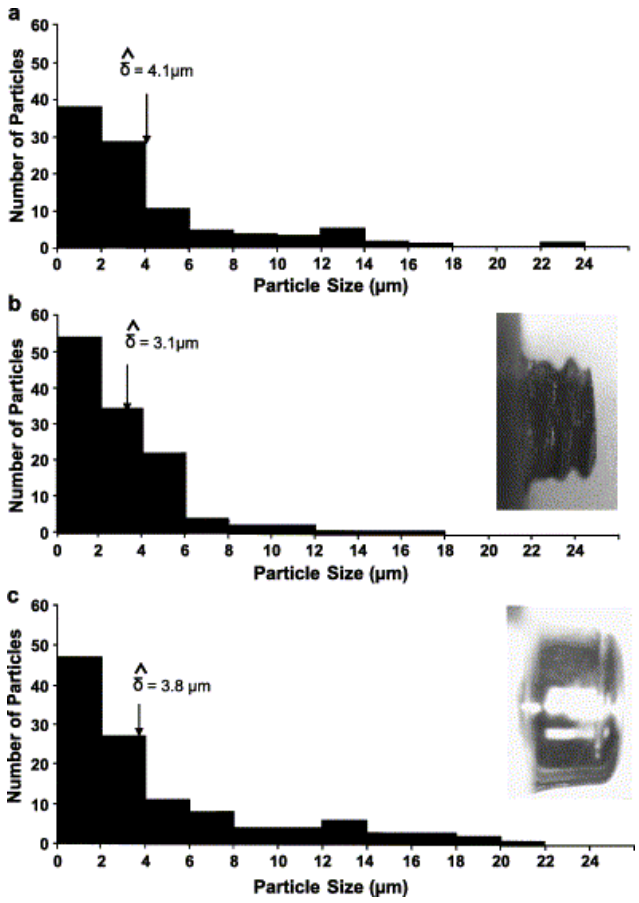

Figure 22 Histograms showing particle size distribution in a) parent material, b) welds with threaded probe, and c) welds with worn, self-optimized probe [25].

Although modeling of material flow is not the focus of Feng's work, he remarks that the flow is fundamentally altered by the wear of the tool. The left half of Figure 23 illustrates the vortical flow which contributes to wear; the flow around the self-optimized probe appears on the right side. The flow pictured in b is consistent with that described by Nunes in several of his papers on flow visualization.

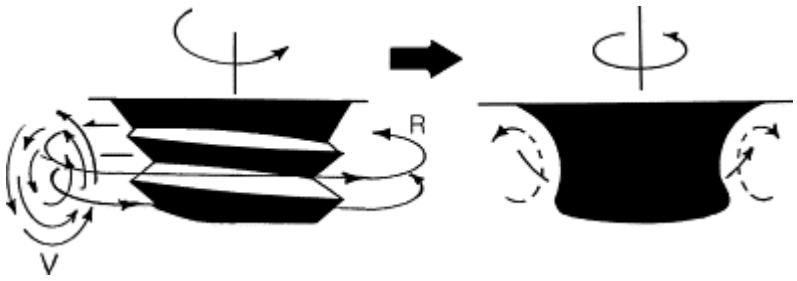

Figure 23 Comparison of flow regimes for threaded probe at onset of weld (left) and self-optimized probe shape (right) [25].

CHAPTER III

EXPERIMENTAL PROCEDURE

We will now detail the experimental conditions under which the research presented in subsequent chapters was conducted. The overall goal of the experimentation was to establish an optimized working envelope for the welding of Al 6061 and Al 6061/SiC/17.5p using coated and uncoated tools. The force and torque data was also analyzed to determine the effect of the coating on the loads experienced by the tool during the weld cycle. This chapter outlines the experimental configuration of the Vanderbilt University Welding Automation Laboratory apparatus for Friction Stir Welding, post-weld mechanical testing and microscopy procedures, the use of optical comparators to assess tool wear, and the processing of data.

3.1 Overview of the FSW Apparatus

The Vanderbilt University Welding Automation Laboratory uses a Milwaukee #2K Universal Milling Machine modified for Friction Stir Welding. A photo of the entire apparatus with the components labeled appears in Figure 24. The Heavy Duty Kearney and Trecker Vertical Head Attachment functions as a fastening mechanism which prevents movement along the vertical axis of the mill. Additionally, a Baldor Industrial VM 2514, 20 Horsepower, 3Phase 230 VAC motor rated for rotation speeds of 3450 RPM is affixed to the vertical head, driving the spindle by means of a belt and pulley system. The larger driven pulley (Emerson/Browning/Morse 16J60P) measures 6

inches in diameter, while the smaller driver (16J45P) pulley is 4.5 inches. This results in a ratio of 7:12, which roughly corresponds to a maximum spindle speed of 2100 RPM.

Lubrication is delivered to the spindle head during the weld cycle via a solenoid which is opened by the control computer at the start of the weld. Tanks of medical-grade compressed Nitrogen gas supply pressure which forces Ethyl lubricator DTE Light Bearing and Circulating Oil #ISO VG 32 through the tubing and into the bearings housed in the spindle head. The lubricator delivery system is also indicated in Figure 24.

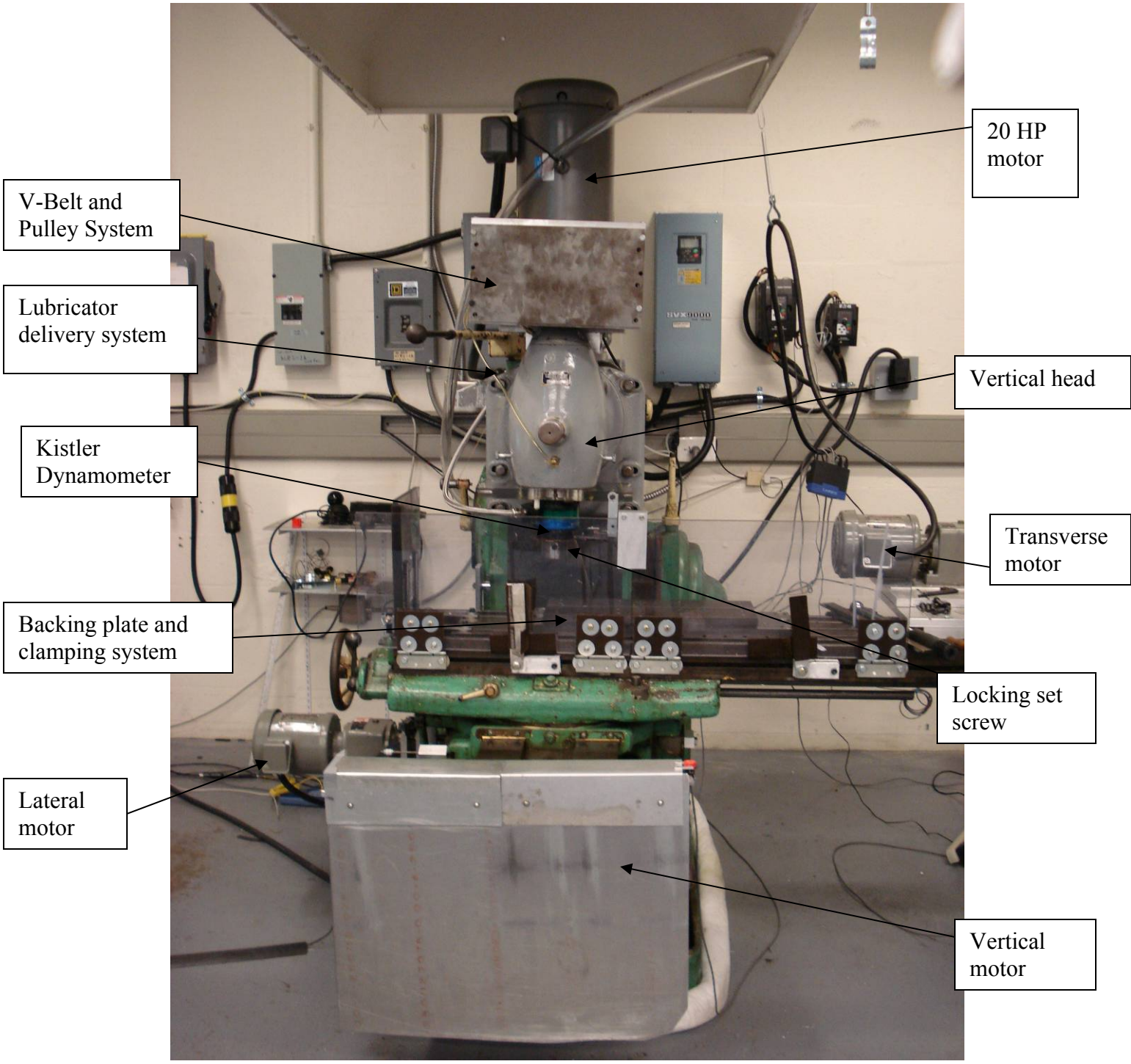

Figure 24 Overview of FSW apparatus

The blue-green instrument which is visible directly below the vertical head is the Kistler Rotating Cutting Force Dynamometer, which is responsible for in-process recordings of forces in the x, y, and z directions as well as torque. The base of the dynamometer is outfitted with two optical encoders. The lower interrupter functions to decouple the forces in the longitudinal and transverse directions, while the uppermost interrupter is responsible for counting the number of revolutions. The spacing between the teeth of the axis interrupter is 36 degrees. A close-up of the dynamometer and optical encoders appears in Figure 25. The laser transmitter works in tandem with the optical interrupters and transmits a signal through the NI-DAQ each time the light transitions from blocked to un-blocked.

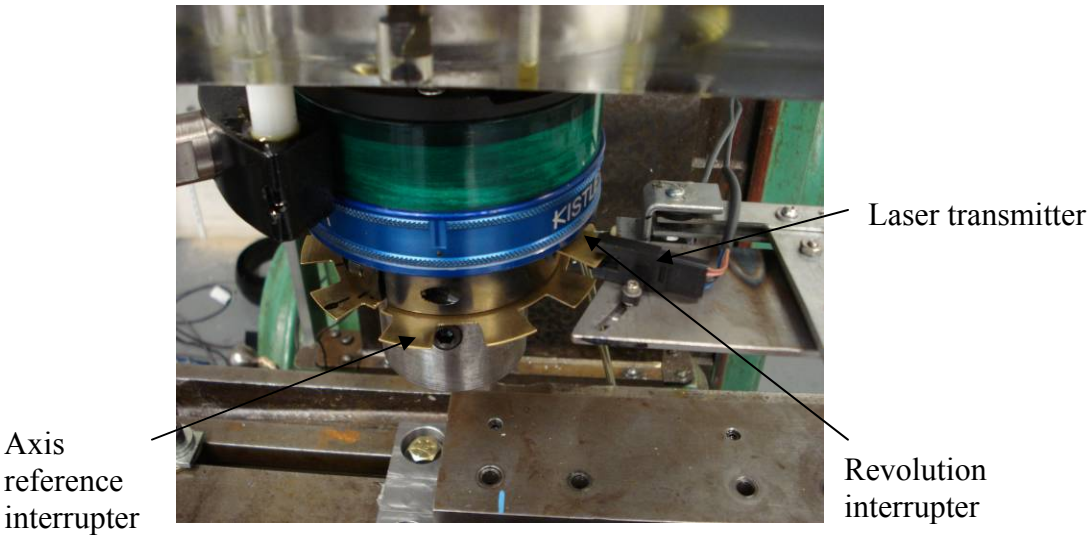

Figure 25 Dynamometer and optical encoders

The locking set screw by which the FSW tool is inserted into the machine is located directly beneath the dynamometer. The tool is positioned with the probe to be used in

welding facing downward toward the backing plate. A square indentation (½ x ½" x 1/10") which has been milled into the upper portion of the tool is aligned with the double set screw. Once proper alignment is achieved, both set screws are securely tightened using an Allen wrench, thus ensuring that the tool will not deflect or oscillate vertically during the course of the weld.

The weld sample rests on top of a backing plate composed of cold-rolled steel with dimensions of 24" x 7" x 1." The sample is clamped into place using a clamping scheme which consists of twenty bolt holes (ten on each side of the sample) which are tightened to 50 N-m using a torque wrench. The purpose of the clamping is to prevent the movement of the sample during the weld process; insufficient clamping can result in bowing or gapping of the material. Though the samples used in this research are only 9"x 3", the clamping and backing plate are large enough to accommodate samples which measure 30" x 5". In the case of bead on plate welds, the sample dimensions for this research are 9"x 3"x ¼". For butt welds, the sample consists of two pieces, each measuring 9" x 1 ½ " x ¼" thick which are aligned so that the FSW tool can traverse a straight line between them to produce a joint.

3.2 Lateral, Traverse, Vertical Motors and Position Control

The positioning and travel of the tool is controlled by the three external motor drives which are used to move the table in the x, y, and z directions. The lateral and traverse motors are both U.S. Electronic 1 Horsepower motors of type TF GDY TE. The lateral motor, which moves the stage in or out in a direction perpendicular to the weld path, has a gear ratio of 6.02 and a minimum speed of 1.7 inches per minute. The lateral

motor is equipped with an optical encoder which records relative position and a string potentiometer which indicates absolute position as a function of voltage. The optical encoder is used primarily for joint tracking experiments where increased resolution and relative measurement of lateral distance is required. The string potentiometer was a sufficient sensor for this research and was used to manually align the tool along the center line of the joint for butt welds.

The vertical motor is located in the metal enclosure at the front of the machine. This motor is a Parker Compumotor (model number 730 MTR) which uses a pulley/gear assembly to move the stage up or down. The maximum speed of the vertical motor is 5 inches per minute. The vertical position is determined by means of a sensor which moves along a magnetic strip. The motion of this sensor is coupled to the vertical motor and the absolute location (zero point) is set when the sensor passes a plastic square located halfway along the magnetic path. The vertical position is specified relative to this absolute location. The vertical motor is used to drive the tool to the weld height (height at which weld is performed) or change height (some height above the table at which the sample and/or tool can be safely changed without incurring harm to other structures on the machine).

The traverse motor has the same specifications as its lateral counterpart, but it is used to move the stage forward (left) or backward (right) relative to the tool. The maximum traverse speed is 14 inches per minute. A string potentiometer identical to that of the lateral motor is used to sense the transverse position of the tool as the table underneath is driven from left to right. Close-ups of the lateral, vertical, and traverse motors are shown in Figures 26a, 26b, and 26c, respectively. It should be noted that the

maximum speeds of the traverse, vertical, and spindle motors can be reconfigured as needed by simply changing the gear ratios.

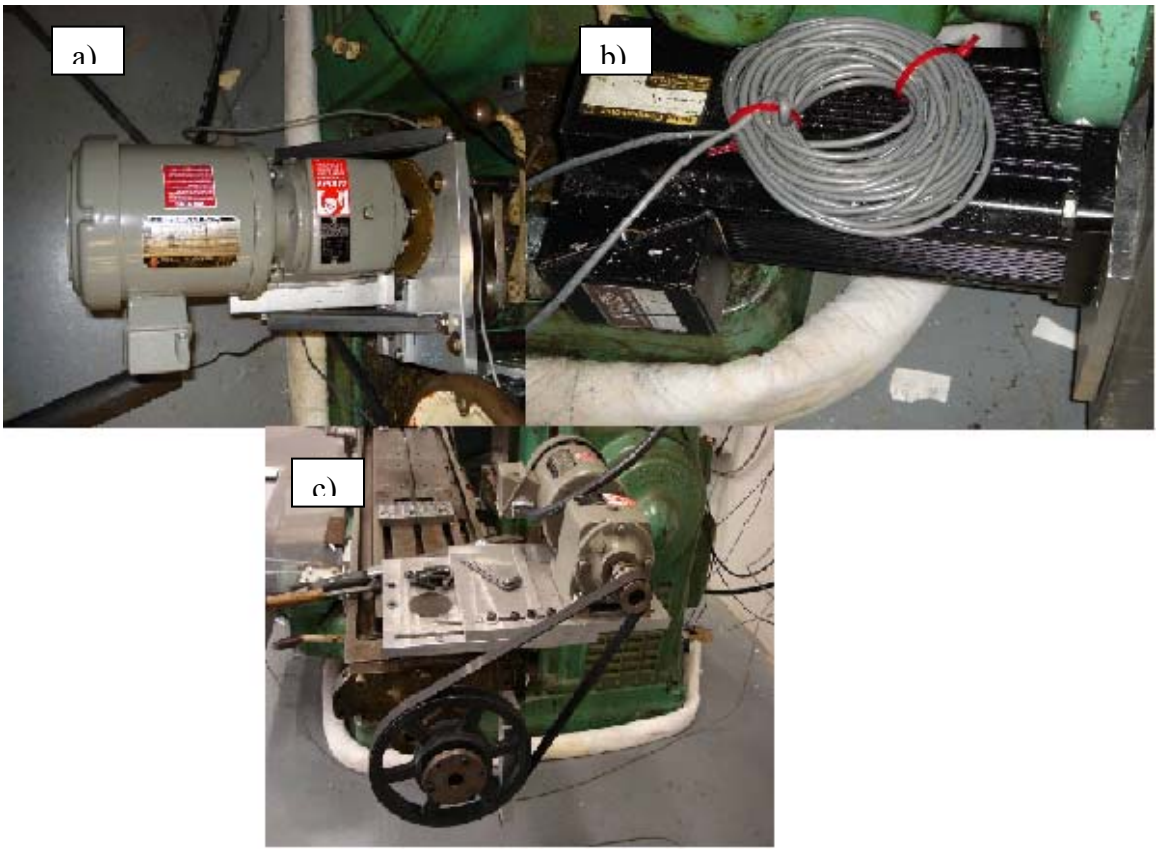

Figure 26 a) lateral motor – U.S. Electronic 1 HP TF GDY TE with optical rotary encoder, b) vertical motor –Parker Compumotor 730 MTR, and c) traverse Motor -- U.S. Electronic 1 HP TF GDY

The motors are controlled through the motor drives which are mounted along the wall behind the FSW apparatus. These drives interface with a sensor box which transmits signals to the control computer (the sensor box is additionally responsible for sending signals from the control computer back to the motor drives). The position data recorded by the aforementioned transducers is also transferred to the control computer via the sensor box. The tool position and spindle speed can thus be controlled through a General

User Interface known as “Weld Controller” on the control computer. “Weld Controller,” written in Dynamic C by graduate student Paul Fleming, effectively automates the entire weld cycle. A screenshot of the control program in use appears in Figure 27.

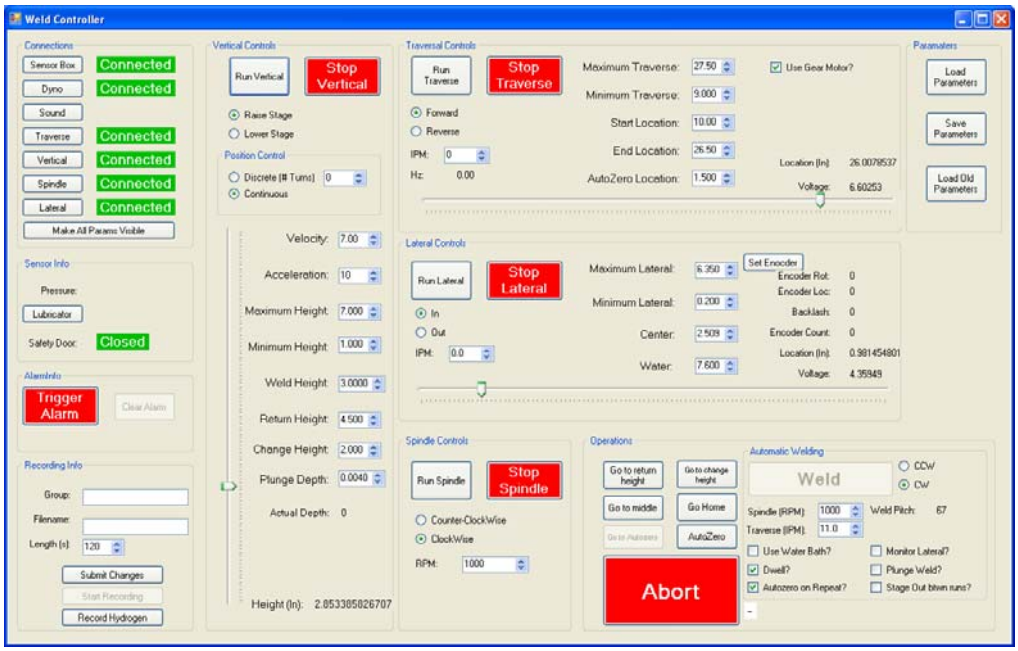

Figure 27 Screenshot of “Weld Controller”

The procedure for performing a typical weld operation using “Weld Controller” is outlined below:

1. Once the tool and sample to be welded are in place, the sensor box, motor drives, and dynamometer are turned on and connected to through the GUI.
2. The vertical motor is zeroed by raising or lowering the stage until the magnetic strip encoder has passed the reference mark.

3. Weld parameters are entered by the user. These include the start and end locations for the weld, plunge depth, spindle speed, traverse rate, return height, change height and the Autozero location.
4. The Autozero location should roughly coincide with the "end" of the sample. The Autozero function in "Weld Controller" will lower the tool until the shoulder contacts the material. Manual adjustments are made as necessary to ensure that the shoulder (rather than the probe) contacts the edge of the sample.
5. The pressure is turned on and the lubricator is activated by clicking the appropriate button in the control program. When lubricant can be seen flowing freely through the tubes which deliver lubricant to the spindle, the lubricator is turned off and the weld can commence. It is only necessary to run the lubricator in this manner for the first weld in a series; once the user clicks "Weld", the lubricator is started automatically.
6. Click "Weld" to initiate the weld. Note that the tool must already be in the start position; this can be easily achieved by clicking "go home." The spindle will start and the tool will gradually "creep" into the material: the creep period ensures that there is sufficient plastic deformation for welding, thus helping to prevent tool fracture. After a few seconds of creep, the machine will weld the sample at the parameters specified by the user. When the tool reaches the end location, the spindle will stop and the tool will return to the change height. The welded sample can then be exchanged with new material and the weld process can be repeated.

During the course of a weld, force and torque recordings are made by the Kistler dynamometer. These files are stored on a second computer separate from that which controls the weld. After the weld is complete, its corresponding data file can be accessed and exported to Microsoft Excel for post-processing and analysis.

3.3 Post-weld analysis: Metallography

In order to assess the quality of a weld using microscopy techniques, the material must first be prepared through a sequence of cutting, polishing and etching to reveal the microstructure of the finished joint. Initially a 1"x 3"x ¼ " piece of the sample is cut away using a band saw. This piece is usually taken from the middle of the sample to ensure that the cross-section will be representative of the steady state process (i.e. free of the anomalous microstructure which may accompany the entrance or exit of the tool from the material). A second cut is then made along the longitudinal axis of this smaller piece of weld using a diamond saw. After cutting is complete, the weld cross-section should measure no more than ¼" x ½" x ¼". The cross-section is then mounted using a thermosetting epoxy molding compound. The mold compound encapsulates the cross-section and, when placed in an environment of sufficient heat and pressure, cures around it. The ultimate result is a black cylinder approximately 1" in diameter and ¾" in height with the weld cross-section exposed on one of the circular faces. The edges of the cylinder are chamfered to augment the polishing process. The cross-section is then polished on a polishing wheel using successively finer grades of Silicon Carbide paper. The grades range from the coarsest at 300 grit to the finest at 3600 grit, with intermediates of 600, 800, 1200, 1600, and 2400. At the end of the polishing stage, the

sample should have a mirror-like finish and be free from scratches or abrasions. Microstructural features such as the weld nugget may already be visible; their appearance will be subsequently enhanced through etching. In etching, the specimen is immersed in an alloy-specific solution which functions to further expose the weld's microstructure for microscopic evaluation. For the Aluminum alloys considered in this study, the specimens were first etched using a solution of 10% Hydroflouric acid (HF) and 90% water. A second etching used Keller's reagent, an etchant composed of 5% Nitric acid, 5% Hydrochloric acid, and 5% Hydroflouric acid. After etching is complete, an optical microscope can be used in conjunction with computer imaging software to characterize the grain structure of the weld as well as capture macrograph images which reveal the weld nugget and/or macroscopic defects such as wormholes, cracking, or hooking.

3.4 Post-weld analysis: Tensile testing

Metallographic analysis techniques are well-suited for any FSW weld configuration (i.e. bead on plate, butt joints, lap welds, T-joints, etc.). Tensile testing, however, is only applicable to welds in which there is an actual "joint line" – hence bead on plate welds are excluded from the tensile testing procedure which follows (consequently, the strength data which traditionally supplements the results of microscopy will not be presented for bead on plate welds). In preparation for tensile testing, a 1"x 3"x ¼" thick section of the weld is milled into the shape of the tensile coupon pictured in Figure 28.

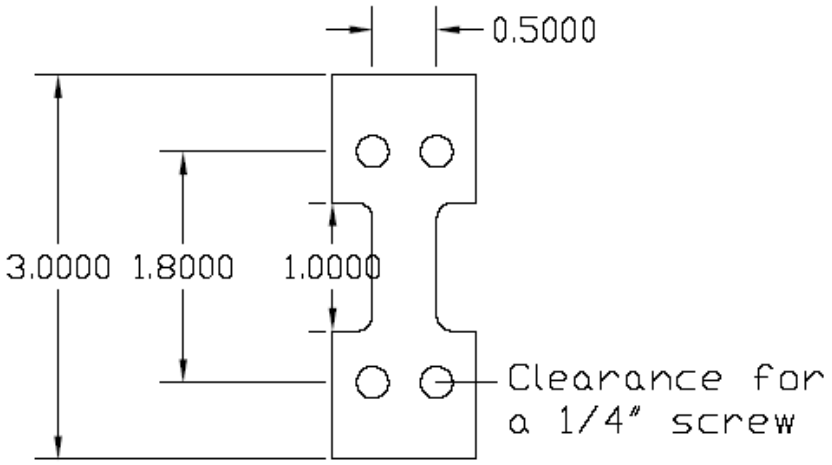

Figure 28 Sketch of coupon used in tensile testing.

These tensile coupons, which are designed in accordance with ASTM standards for mechanical testing, are assessed using an MTS machine equipped with a hydraulic press for tensile and compression testing. The thickness and width of the specimen are measured by the user and input into the computer prior to testing. As the coupon is pulled apart, the computer records the stress, strain, ultimate tensile strength (UTS), yield strength (YS), and percent elongation. This data file can then be used to generate plots of stress versus strain and/or load versus extension. Results of tensile tests are usually specified in terms of joint efficiency, defined as the ratio of the UTS of the weld specimen to the UTS of the parent material expressed as a percentage. Ideally, a tensile specimen will have a joint efficiency of greater than 70% and break outside the weld line. A "good" weld is characterized by both high joint efficiency and a defect-free macrosection, criteria which will be discussed further in the chapters on experimental results.

3.5 Shadowgraph

A shadowgraph technique was used as an optical comparator to measure tool wear in welds of Metal Matrix Composites (MMCs). The shadowgraph machine works largely in the same manner as an overhead projector, using a Fresnel lens to focus the light from a lamp aimed at the specimen. Each wear study begins with an unused FSW tool which serves as a baseline. The shadowgraph of the unworn tool is then compared with successive shadowgraphs of the tool post-weld. In this manner, the shadowgraph is used to provide a visual representation of tool wear which supplements the quantitative data. Specifics of the shadowgraph technique and how they were applied to this research will be further discussed in Chapter V.

CHAPTER IV

EXPERIMENTAL RESULTS FOR SMOOTH PROBE FSW TOOLS ON AL 6061

Experimental results for welds performed on Aluminum 6061 using an uncoated steel tool and a Molybdenum tool of identical geometry coated with diamond by Chemical Vapor Deposition will be compared in this chapter. The primary basis for comparison is the measurement of longitudinal force, transverse force, axial force, and torque recorded during welding by the dynamometer. The principal limitation in robotic applications of Friction Stir Welding is axial force. Thus, any reduction in axial force which is attained through the use of a coated tool is advantageous from a robotics standpoint. To ascertain that this decrease in axial force is not accompanied by a decline in weld quality, macrosections of welds performed at identical parameters using the uncoated and coated tool were also evaluated.

4.1 Tool Design

The tool geometry considered in this stage of the research was a smooth cylindrical probe. Although the tool was devoid of the features (threads, flats, flutes, etc.) which enhance vertical stirring and often result in a better quality weld, the smooth probe was chosen for its simple geometry and ease of machining. Additionally, the welds performed on Al 6061 were all "bead on plate" welds; the emphasis was on comparative analysis of force data rather than optimization of weld quality. The tool dimensions were based on the previous research of graduate student Reginald Crawford [27]. All tools in

this study had a probe diameter of 0.2 inches, a probe length of 0.15 inches, a flat shoulder with diameter 0.5 inches, and a shank of 0.75 inch diameter. A three-dimensional image of the tool rendered using PATRAN, a finite element pre-processor, appears in Figure 29.

Figure 29 3-D rendering of smooth probe FSW tool

The monolithic h13 steel FSW tool was made by the Vanderbilt University Physics Machine Shop and underwent a heat treatment process prior to use in welding. As previously stated, the substrate for the coated tool is Molybdenum, a material chosen because of its ability to withstand the extreme temperature incurred in the coating process. Due to the size of the coating chamber at the Vanderbilt University Diamond Fabrication Lab, the coated tool was machined in two parts. The Molybdenum piece (consisting of the tool probe and shoulder) was made by Midwest Tungsten of Chicago, IL. Once the coating was complete, this Molybdenum part was press fit into a 0.75" diameter shank of h13 steel. SEM (Scanning Electron Microscope) images of the coating

on the probe of the completed tool appear in Figure 30. The layer of diamond deposited on the probe and shoulder is only a few micrometers thick. However, the nature of the coating is such that it should not deteriorate unless the working temperature of the tool exceeds the melting point of diamond (4000 ^{o}C), a remote possibility in a lower-temperature solid-state process such as FSW.

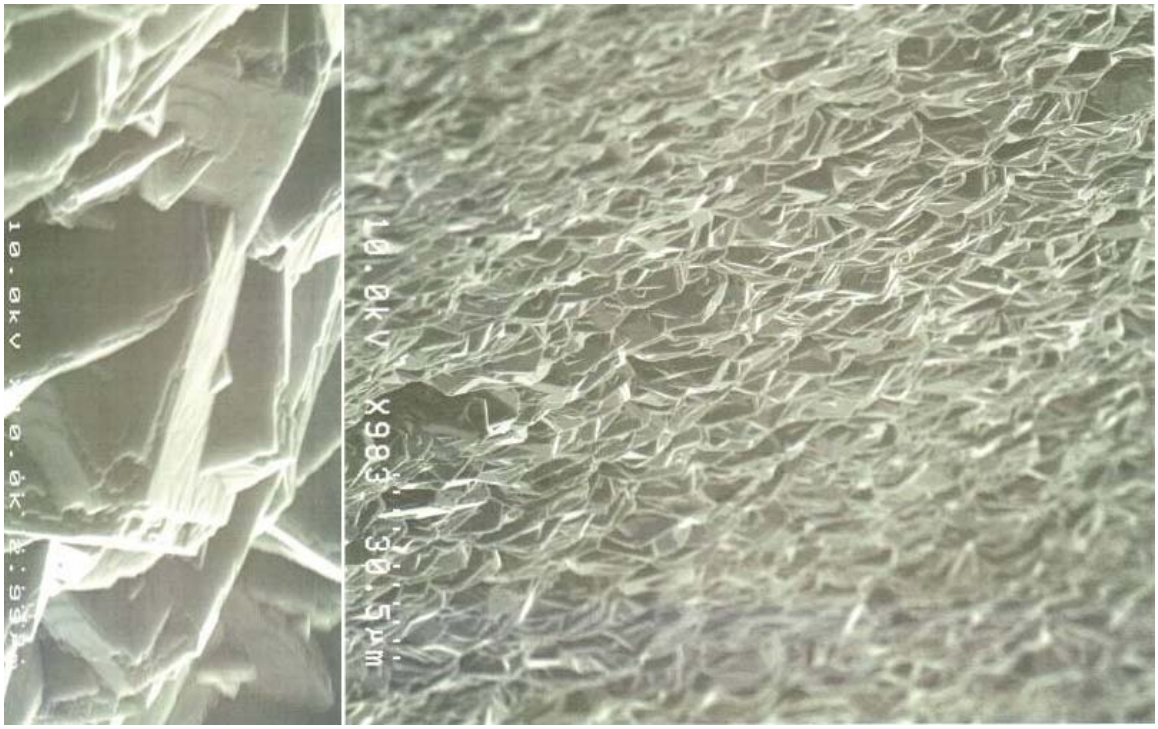

Figure 30 SEM images of coating on FSW probe (taken by Mick Howell).

4.2 Parameter selection

At the time the research presented in this chapter was performed, the Vanderbilt University Welding Automation Laboratory Friction Stir Welding apparatus was configured for high speed processes. The maximum operating speeds of the various

motors (some of which are different than those presented in the previous chapter on experimental setup) are listed in Table 10.

Table 10 Maximum operating speeds for various motors on FSW apparatus at time smooth probe research was conducted [27].

Motor	Maximum operating speed
Spindle	6000 rpm
Traverse	63.3 ipm
Lateral	2 ipm
Vertical	5 ipm

The upper limits listed for the lateral and vertical motors are not true operational limits, per se, but rather indicate the maximum speed at which these motors can be operated safely. The higher speed configuration is reflected in the selection of weld parameters for the smooth probe experiments. The smooth probe weld matrix is shown in Table 11.

Table 11 Weld matrix for smooth probe experiments. "x" indicates parameters for which welds were performed.

Spindle Speed (rpm) \ Travel speed (ipm)	10	15	16	20	25	30
1500	/	X	X	/	/	/
1600	X	/	/	/	/	/
1900	X	/	/	/	/	/
2000	/	X	X	X	/	/
2100	X	/	/	/	/	/
2500	/	X	X	/	X	/
3000	/	X	X	/	/	X

The parameters in Table 11 were chosen based on a number of factors. It was important to have parameter sets in which travel speed was varied while the rotation speed was held constant (and vice versa) so that plots could be generated which clearly characterize force or torque as a function of travel or rotation speed. Additionally, it was desirable to use the higher-speed capabilities of the apparatus as a way to evaluate the behavior of the tool at faster speeds. The dimensionless constant of Debroy et al. suggests that the coated tool may produce better results at higher rotation speeds (the research of Debroy et al. will be discussed more thoroughly later in this chapter) [28].

The number of welds that could be completed using the coated tool was also limited by the tendency of the Molybdenum to fracture. While Molybdenum is advantageous as a substrate because of its ability to withstand high temperatures, it is also

very brittle and prone to fracture when it undergoes stress. Of the three original coated tools set aside for this portion of the research, two of the three failed. Specifically, the probe sheared off upon entrance into the workpiece material. This shearing phenomenon is even more pronounced in uncoated Molybdenum (the coated Molybdenum tool may be less brittle because it has been subjected to the high temperature environment of the coating chamber, a process analogous to heat treatment). It may be possible to reduce the incidence of probe failure by pre-drilling a hole with a diameter slightly larger than that of the probe into the workpiece material. This would enable the shoulder of the tool to fully contact the material before the probe, creating a preheat zone which would plasticize the material and reduce stresses on the probe as it enters the material. The effect of pre-drilling will be assessed more fully in a subsequent chapter.

For all welds, the tool tilt angle was fixed at 2^0 and the plunge depth was set at 0.004 inches. The latter specification indicates that the tool plunges an additional 0.004 inches below the zero point before welding begins (this is done to ensure sufficient shoulder contact with the workpiece material). A 0.15 inch probe length, 0.25 inch thick material, and a plunge depth of 0.004 inches result in a weld ligament (distance from the probe tip to the backing plate) of 0.096 inches. This is a rather large ligament (for butt welds the optimal value can be as small as 0.01 inches), but it is acceptable for the research presented in this chapter. Since we are performing bead on plate welds and are primarily concerned with the recording of force data rather than the ultimate strength of the weld (these welds were not subjected to tensile tests), a partial penetration weld is sufficient.

4.3 Results: General trends in force data for the uncoated steel smooth probe FSW tool

Several welds were performed for each parameter set in the weld matrix of Figure 11. In most cases, at least two welds with the same tool were performed at a given parameter. If there were any anomalies in the force data for a tool/parameter combination (typically a variation of more than ten percent), a third weld was completed.

Values for force and torque (Fx, Fy, Fz, and Mz) are extracted from an Excel spreadsheet which compiles the data recorded by the dynamometer. The dynamometer records ten samples per revolution – hence a typical weld file can contain anywhere from 25,000 to upwards of 60,000 data points, depending on the length of the weld. A significant segment of this data is recorded either in the period before the actual weld commences or after the tool has exited the material. Hence the best way to obtain a steady state value for force is to graph the dynamometer data versus time in Excel and then visually estimate the cells which contain steady state data. This method is not as imprecise as it may initially seem. Figure 31 shows a typical force vs. time graph for a steel tool welding Aluminum 6061 at 2000 rpm and 20 ipm. The flat lines on the left and right sides of the graph correspond to the period before and after the tool engages with the material, respectively. The high plateau in the center of the graph corresponds to the steady-state weld condition, while the lower plateau coincides with the "creep" (the phase in which the tool dwells in the material to generate sufficient heat for welding).

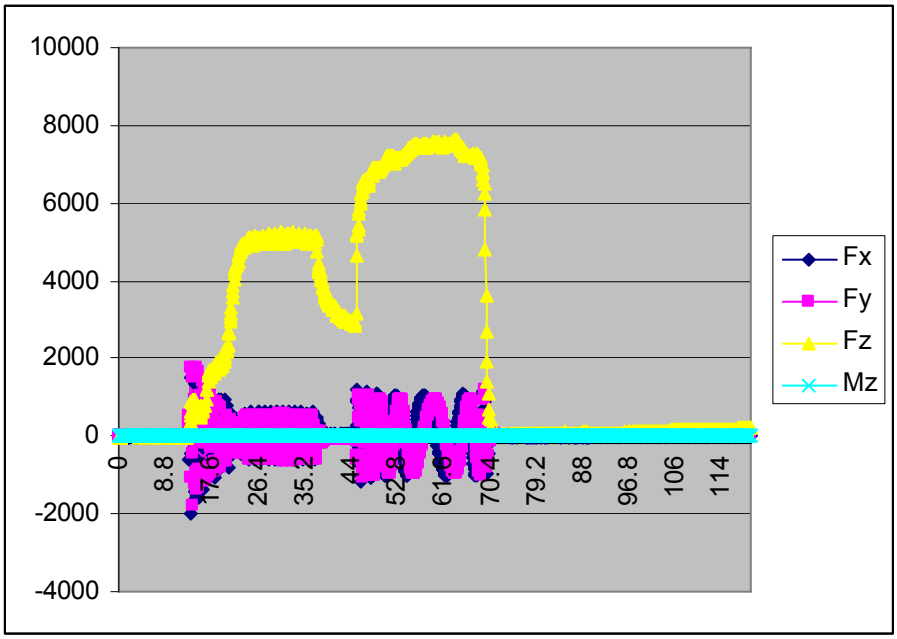

Figure 31 Example of force vs. time graph

In the case of the axial force and torque, it is easiest to average a sample of around one thousand points from the steady state data. Since the smooth probe welds were performed before the x and y forces were decoupled, the best way to obtain an accurate representation of these forces is by averaging the peak values of the steady-state data. It is apparent from Figure 31 that Fx and Fy are sinusoidal; thus, the peak value is simply half of the amplitude.

Some preliminary welds were performed using the smooth probe steel tool in order to assess the effect of rotation speed on force and torque. The graph in Figure 32 displays the magnitude of forces in the x, y, and z direction for the smooth probe steel tool as a function of rotation speed. The trends observed corroborate the work of Crawford, et al. [27]. For a constant travel speed, transverse and longitudinal forces increase with increasing rotation speed. Although the trendline for axial force in Figure

32 is less uniform, it is apparent that overall the z-force experienced by the tool decreases with an increase in spindle speed. The force plots for these welds, as well as all welds in this chapter, can be found in Appendices A (for the uncoated tool) and B (for the coated tool).

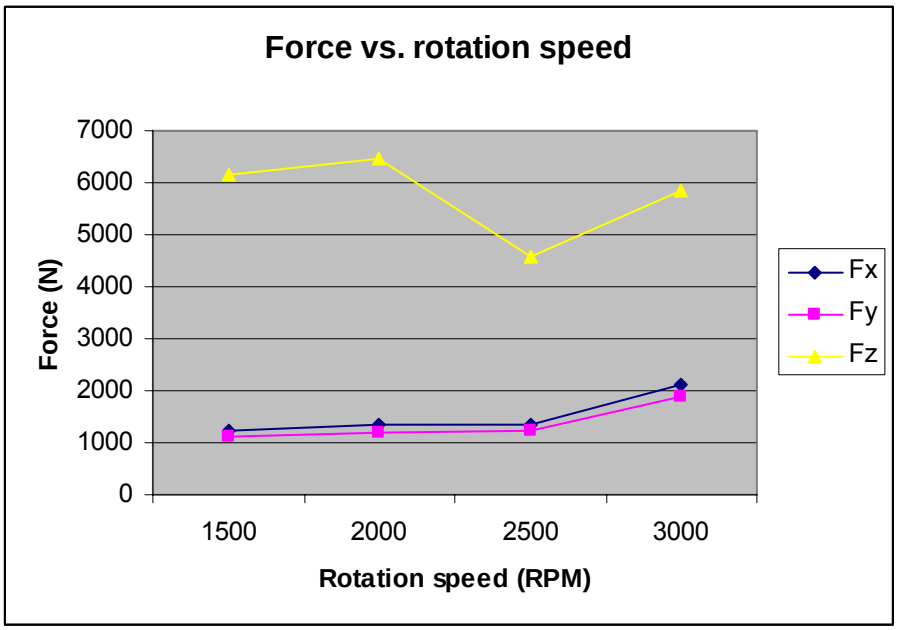

Figure 32 Force as a function of rotation speed for steel tool with a smooth probe geometry. Travel speed was held constant at 16 ipm. Each data point represents the average of two experiments.

The torque data for the smooth probe steel tool was also plotted against rotation speed; the results of this analysis are shown in Figure 34. A cursory evaluation of the graph indicates that torque is inversely proportional to rotation speed, an observation which is also consistent with the research of Crawford [27].

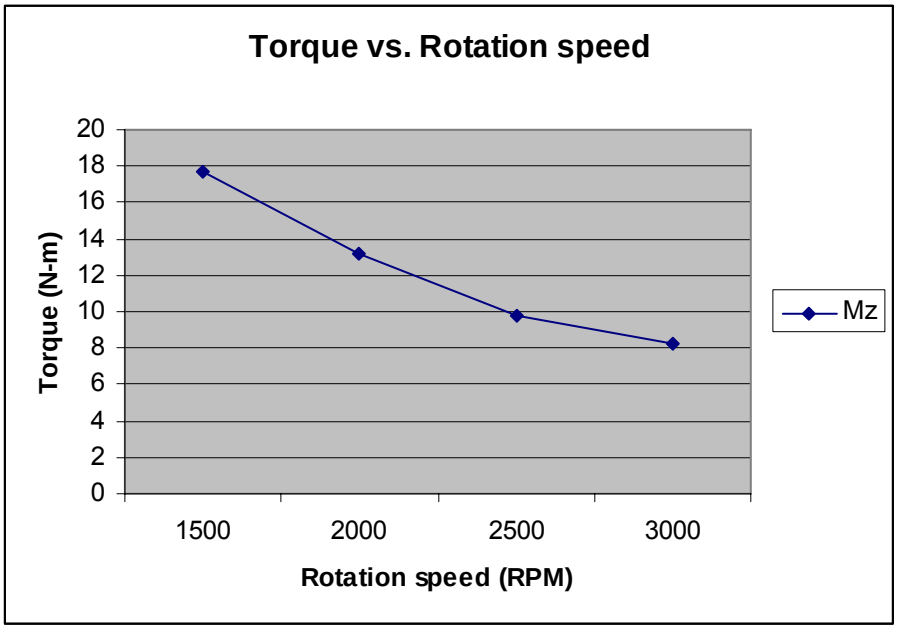

Figure 33 Plot of torque vs. rotation speed for steel tool with smooth probe geometry. Travel rate is constant at 16 ipm.

The formulation for power in FSW is 2π x torque x RPM/60. The units of power in this case are N-m/s, or Watts (W). Power is plotted against rotation speed in Figure 34. Since power is a function of torque, the results of this graph mirror those of Figure 33 (torque vs. rotation speed). As rotation speed increases, torque (and thus power) decreases.

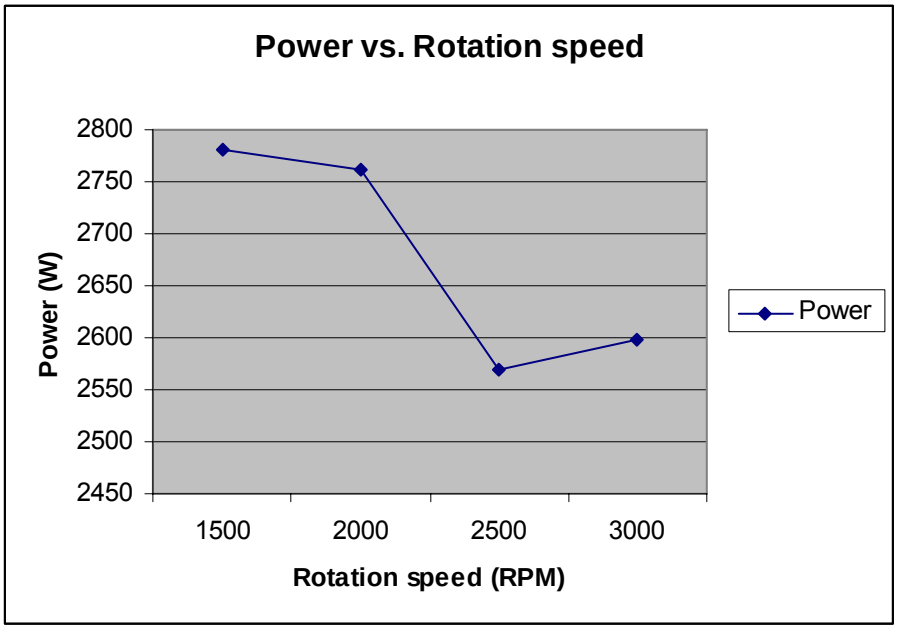

Figure 34 Plot of power vs. rotation speed for steel tool with smooth probe geometry. Travel speed is constant at 16 ipm.

4.4 Results: Force data for diamond coated smooth probe FSW tool

Once the general trends in force and torque data for the uncoated tool with smooth probe geometry were established, a similar analysis was performed for the coated tool. The diamond tool was assessed by evaluating the force data obtained for each of the parameters listed in Table 11. The force in the x-direction as a function of rotation speed is shown in the scatterplot of Figure 35.

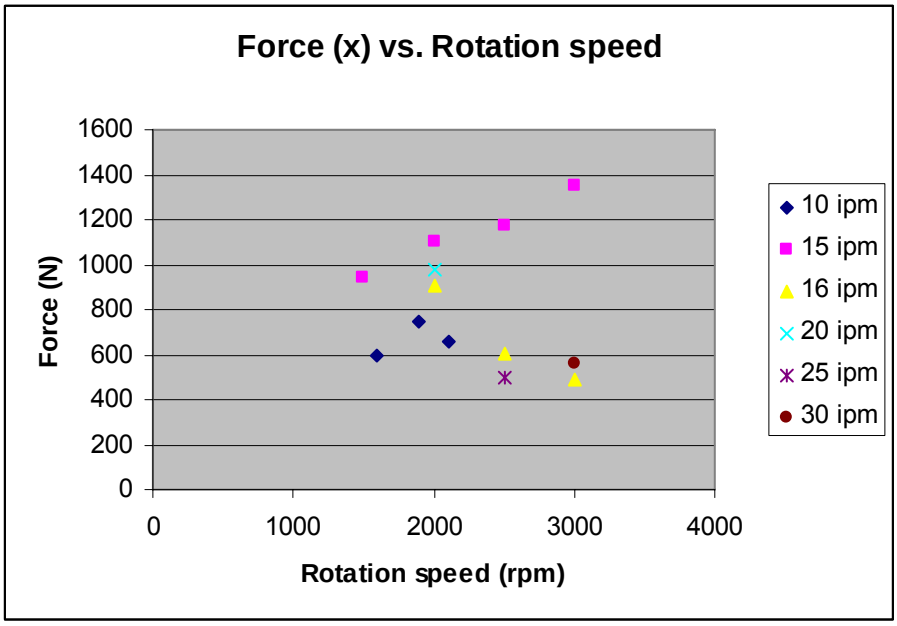

Figure 35 Scatterplot of Fx vs. Rotation speed for coated tool with smooth probe geometry.

From this plot we see that the peak x-forces encountered by the tool are in the range of approximately 500 N (for 16 IPM and 3000 RPM) to 1400 N. This is substantially lower than the forces experienced by the uncoated tool, which vary from approximately 1000 N (at 16 IPM and 1500 RPM) to 2000 N (at 16 IPM and 3000 RPM). It should also be noted that at least a portion of the data for the coated tool does not follow the trends we observed in section 4.3. For the 15 IPM series, Fx increases with increasing rotation speed, a trend which is in agreement with the work of Crawford and the results of section 4.3. However, the opposite is observed for the 16 IPM series, in which case Fx drops precipitously with increasing rotation speed. A possible explanation for these and other anomalies in the data, along with a more rigorous quantification of the force reduction for various parameters, will be presented in the next section.

The force in the y-direction plotted against rotation speed is shown in Figure 36. Overall, the y-direction forces are lower in comparison with those recorded for the uncoated tool (Figure 32). Once again, the trend established in section 4.3 (that of direct proportionality between y force and rotation speed) is absent in the data for both the 10 IPM and 16 IPM series of welds.

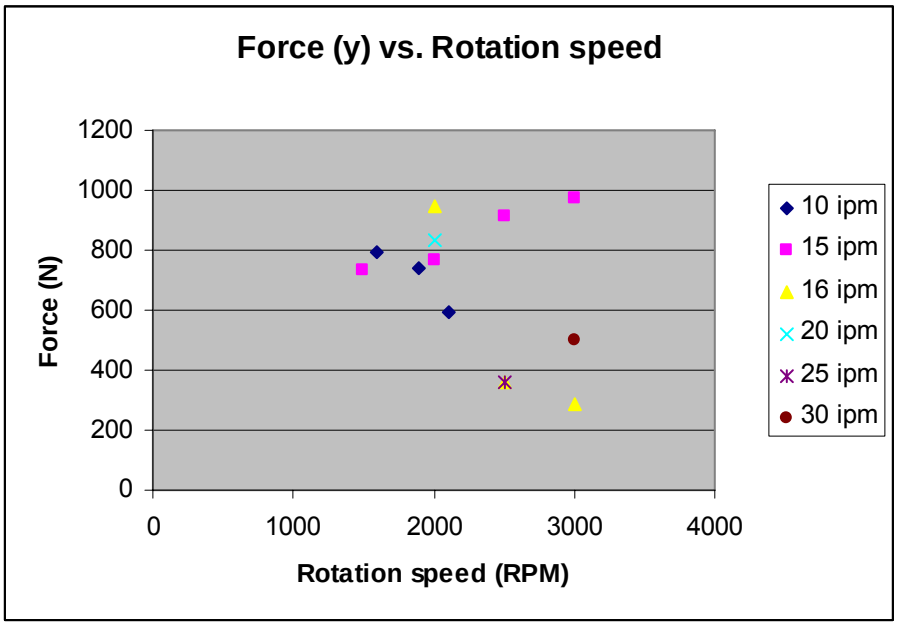

Figure 36 Fy vs. rotation speed for coated tool with smooth probe geometry.

Perhaps the most dramatic benefit of using a coated tool on Aluminum is readily apparent in the plot of Figure 37. A perfunctory comparison of the data points in Figure 37 with those for the uncoated tool (Figure 32) reveal a substantial reduction in axial force. The decrease in the average axial force values for the coated tool becomes more pronounced with increasing rotation speed, an observation which is consistent with the trends documented by Crawford [27].

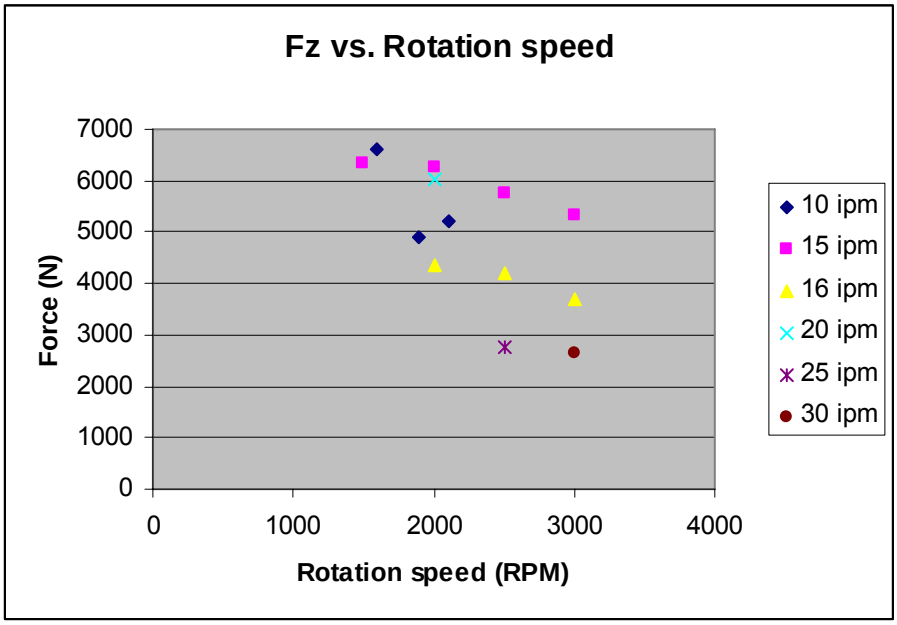

Figure 37 Fz vs. rotation speed for coated tool with smooth probe geometry.

The variation of torque with rotation speed is plotted in Figure 38. As in the case for the uncoated tool, torque is inversely proportional to rotation speed. The range of torques recorded for the coated tool is significantly lower than those recorded for the uncoated tool (Figure 33).

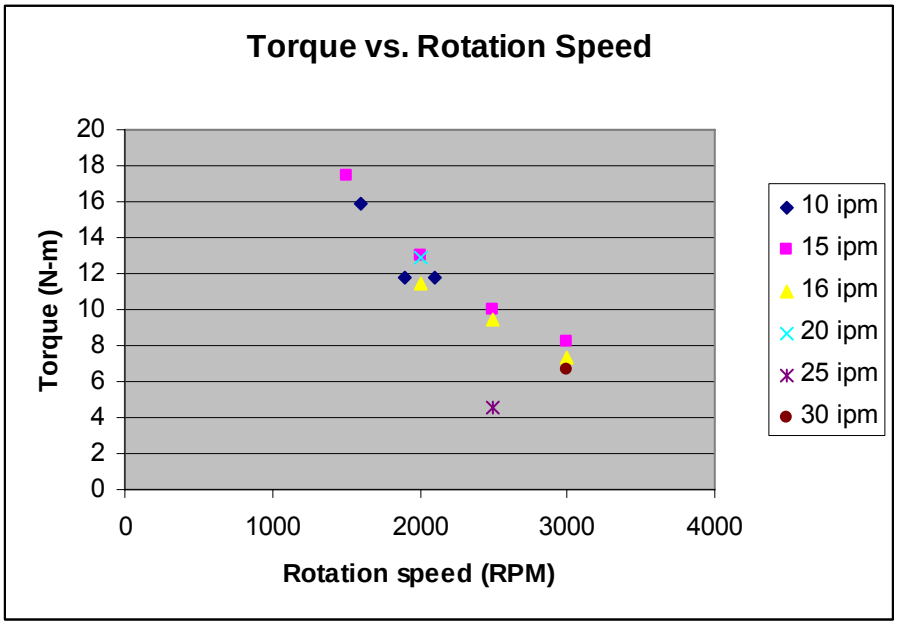

Figure 38 Torque vs. rotation speed for coated tool with smooth probe geometry.

There is also a correlation between axial force and torque: the parameters in Figure 37 which correspond to the lowest values of axial force also experience the smallest torque (similarly, a larger value for axial force corresponds to greater torque). This may seem like an obvious result, but it can serve as an internal check on the quality of the data we have presented thus far. A scatterplot of torque and axial force is shown in Figure 39. The relationship between the variables is roughly linear; a regression analysis yields an R^2 value (correlation coefficient) of 0.74. The correlation is also positive – that is, axial force and torque are approximately directly proportional.

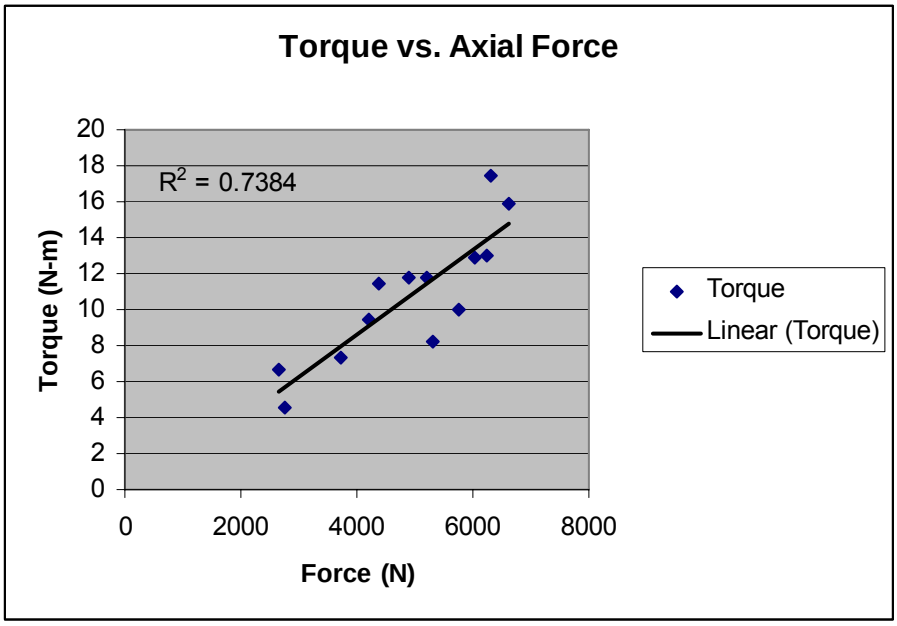

Figure 39 Scatterplot of Torque vs. Axial Force (Fz). The linear trendline has a correlation coefficient of 0.7384.

The formulation used to calculate power for the coated tool is identical to that introduced in section 2.3. Figure 40 displays the plot of power as a function of rotation speed for the coated tool. A clear trend emerges from this data: with the exception of the 25 IPM/2500 RPM case (a point which may be considered an outlier even though it is the average of two welds and thus exhibits internal consistency), power decreases slightly with increasing rotation speed. Comparing the power values for this tool to those of its uncoated counterpart (Figure 34), we see that the values for power obtained using the coated tool are comparable to those reported for the uncoated tool in section 4.3. A more thorough comparative analysis of the force data for the coated and uncoated tools appears in the next section.

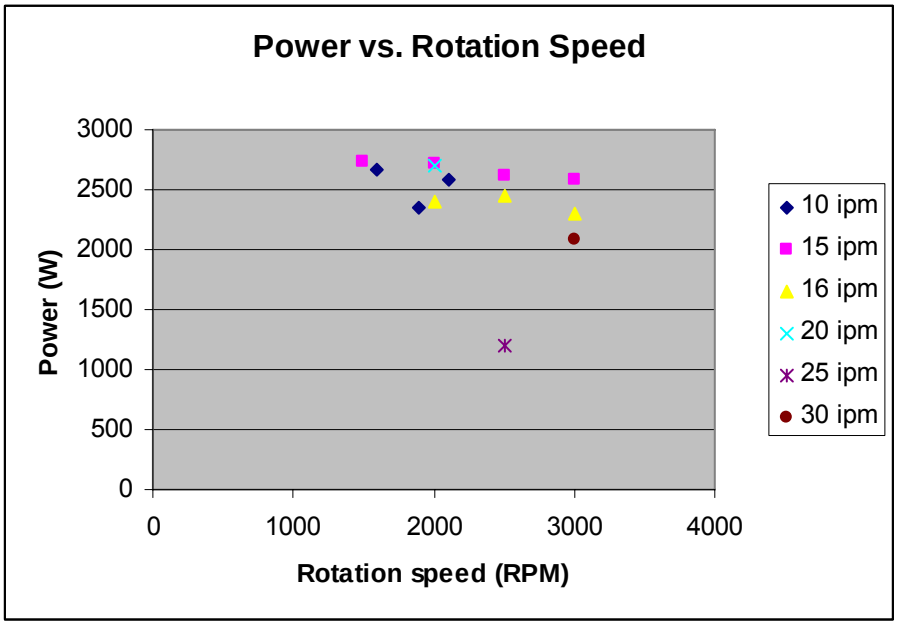

Figure 40 Power vs. rotation speed for coated tool with smooth probe geometry.

4.5 Results: Comparison of Data for Coated and Uncoated Smooth Probe FSW Tools

The reduction in loads and torques which are achieved through the use of the coated tool will now be quantified more precisely. The Dynamometer data recorded during a weld with the uncoated tool can be directly compared with the data for the coated tool at the same parameters (since the tools under consideration are of identical geometry, the only variable becomes the tool material). The bar graphs in Figure 41, 42, and 43 provide a side by side comparison of the x, y, and z forces, respectively, for the coated and uncoated tools at the parameters which showed the greatest reduction in forces.

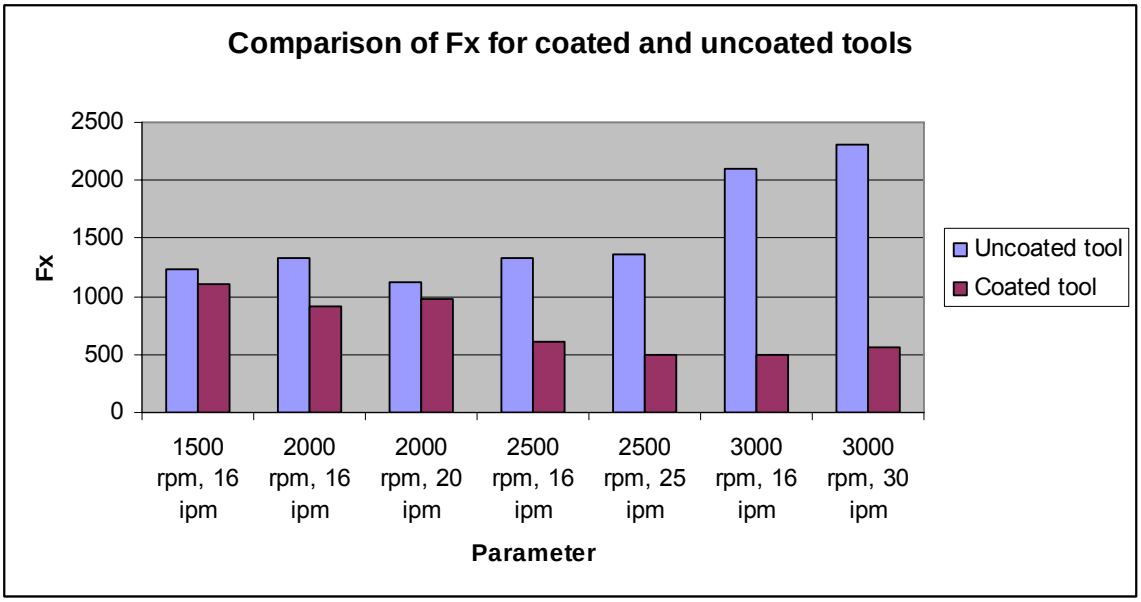

Figure 41 Comparison of force in x-direction for coated and uncoated tool at various parameters.

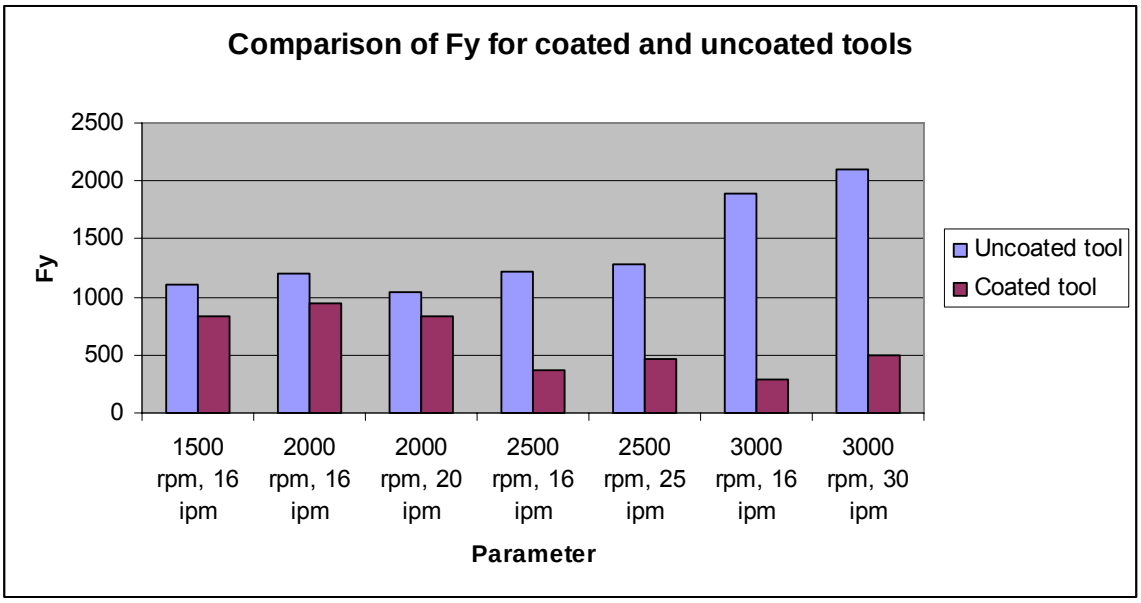

Figure 42 Comparison of force in y-direction for coated and uncoated tool at various parameters.

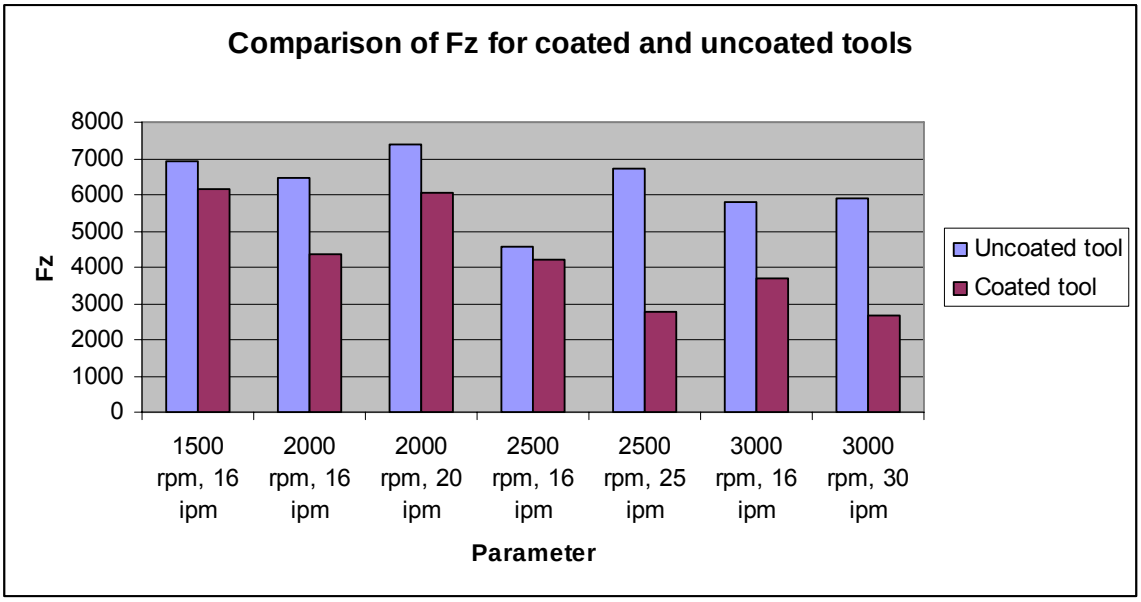

Figure 43 Comparison of force in z-direction for coated and uncoated tool at various parameters.

The percent reduction in forces achieved by using the coated tool at a given parameter is summarized in Table 12. The third column, weld pitch, is defined as the ratio of rotation speed (rotations per minute) to travel speed (inches per minute). The units for weld pitch are thus revolutions per inch. The weld pitch can be decreased by: 1) holding the rotation speed constant and increasing the travel rate or 2) holding the travel rate constant and decreasing the rotation speed. Conversely, maintaining a constant travel rate while increasing the rotation speed or controlling the rotation speed while decreasing the travel rate increases the weld pitch.

Table 12 Percent reduction in x, y, and z forces for coated tool (as compared with values for uncoated tool at the same parameters)

Rotation speed (rpm)	Travel speed (ipm)	Weld Pitch	% Reduction in Fx	% Reduction in Fy	% Reduction in Fz
1500	16	93.75	10.65907242	25.78616352	11.56395703
2000	16	125	32.28699552	21.24481328	32.34164743
2000	20	100	13.06286224	20.1345507	18.21739306
2500	16	156.25	55.00747384	70.15663644	8.296777625
2500	25	100	63.71616679	63.18057188	58.89386725
3000	16	187.5	76.65555026	84.86772487	36.22117403
3000	30	100	75.65217391	76.19047619	55.15889831

From the summary of preliminary results presented in the table above, it becomes evident that the percent reduction in x, y, and z forces for the coated tool is more pronounced at higher rotation speeds. The maximum reduction in the transverse and longitudinal forces occurs at 3000 rpm and 16 ipm. The optimal reduction in axial force, however, is observed for the 2500 rpm, 25 ipm case. Thus a significant reduction in transverse and longitudinal forces does not necessarily translate into a comparable reduction in axial force. The 2500 rpm, 16 ipm parameter set, for instance, experiences a 55 and 70 percent reduction in x and y forces, respectively, but only an 8 percent reduction in z force. Hence, there is not an obvious predictive relationship between rotation speed, travel speed, and/or weld pitch. It can, however, be generally stated that increasing rotation speed is accompanied by an overall decrease in axial force. A graph displaying the torque data for the chosen parameters is shown in Figure 44.

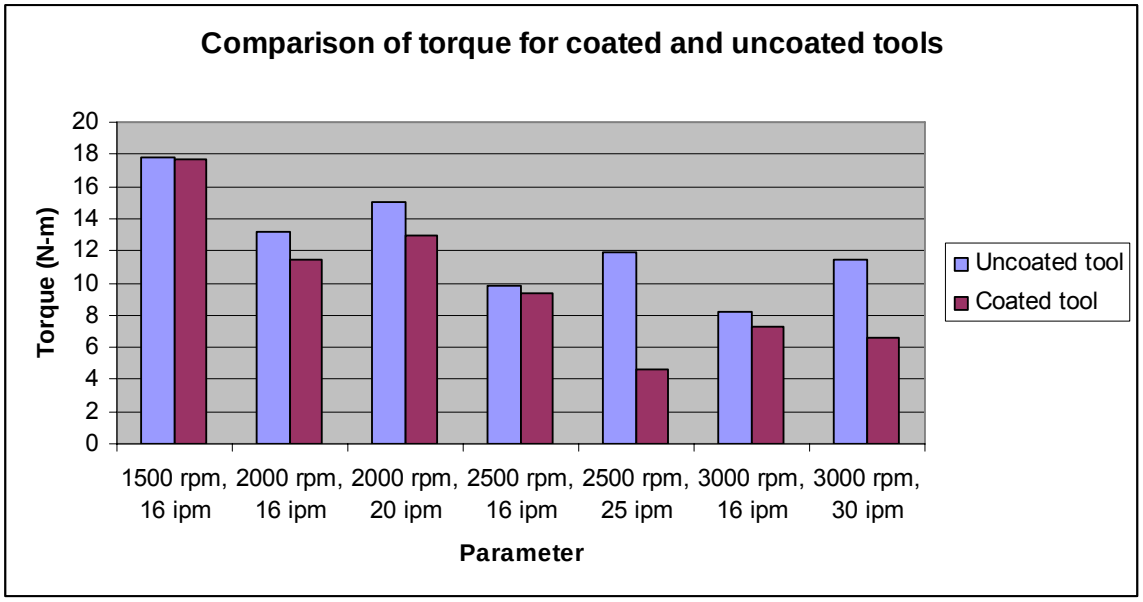

Figure 44 Comparison of torque for coated and uncoated tool at various parameters.

Figure 45 presents the accompanying power values for the parameters in the previous graphs.

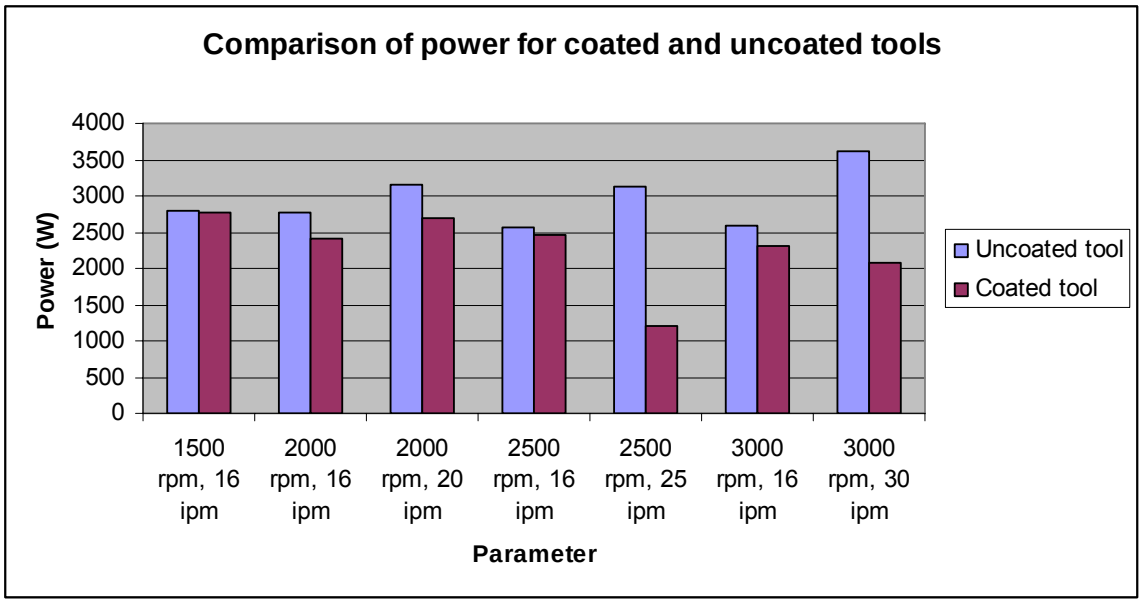

Figure 45 Comparison of power for coated and uncoated tool at various parameters.

The percent reduction in torque and power attained with the use of the coated tool is summarized in Table 13.

Table 13 Percent reduction in torque and power for coated tool (as compared with values for uncoated tool at the same parameters).

Rotation speed (rpm)	Travel speed (ipm)	Weld Pitch	%Reduction in Torque	% Reduction in Power
1500	16	93.75	0.884739422	0.884739422
2000	16	125	13.00808077	13.00808077
2000	20	100	14.26270137	14.26270137
2500	16	156.25	4.34287792	4.34287792
2500	25	100	61.6537084	61.6537084
3000	16	187.5	11.31263299	11.31263299
3000	30	100	42.25156522	42.25156522

The results summarized in the table above parallel those presented in Table 12. The outcomes of these tables are consistent with the proportionality between axial force and torque previously established. The parameter at which the greatest reduction in axial force was observed (2500 rpm, 25 ipm) also experiences the largest reduction in torque/power. Since power is directly proportional to torque, the percent reductions in torque and power are identical for a given parameter.

Although the reductions in longitudinal force, transverse force, torque, and power are a noteworthy corollary to use of the coated tool, the central interest lies in axial force reduction (since axial force is the primary limiting factor in robotic applications of FSW).

A substantial reduction in any force, but particularly axial, is advantageous from a robotics standpoint; specifically, less axial force required to produce a suitable weld could translate into the design of smaller automated systems for FSW processes. The caveat to this rests with the quality of the weld – if the coated tool is to be a viable option for industry usage, the reduction in axial force cannot be accompanied by a significant decline in weld integrity. The macrosections of welds performed at identical parameters using the uncoated and coated tools were compared to assess what effect, if any, the coating had on the weld's structural characteristics. The microscope images of these welds, prepared using the metallographic method outlined in chapter III, are compared in Figure 46.

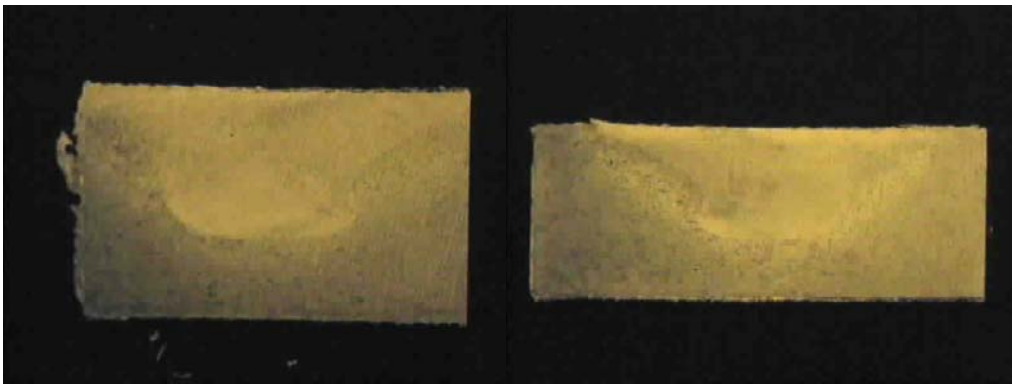

a) 1500 rpm, 16 ipm

Figure 46 (continued)

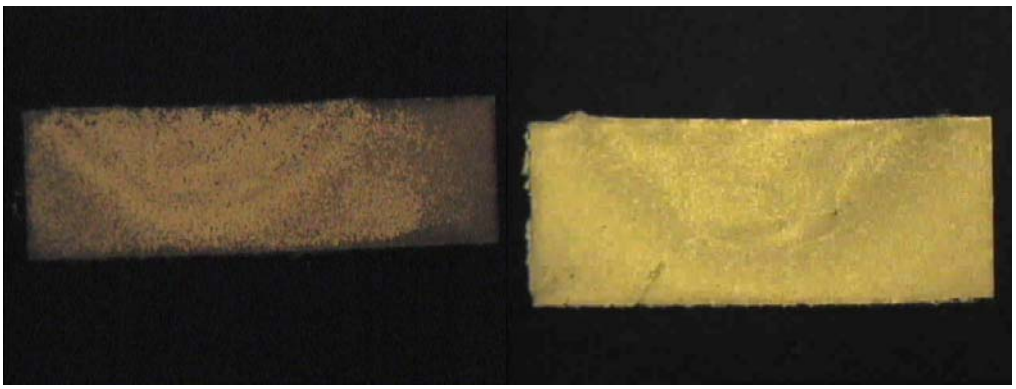

b) 2000 rpm, 16 ipm

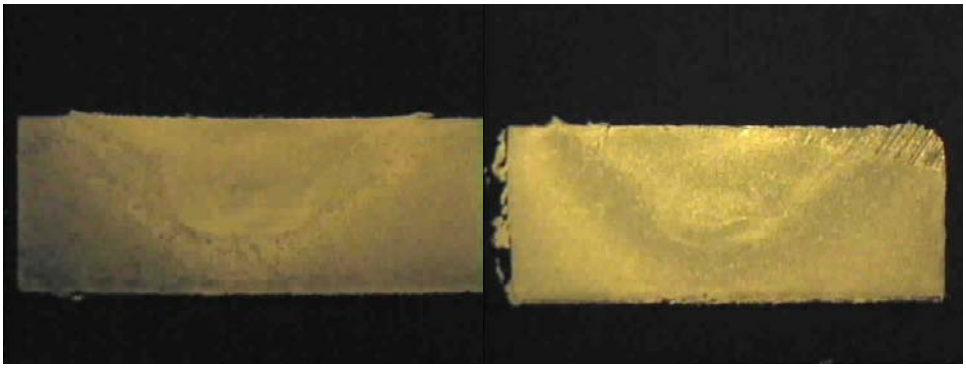

c) 2000 rpm, 20 ipm

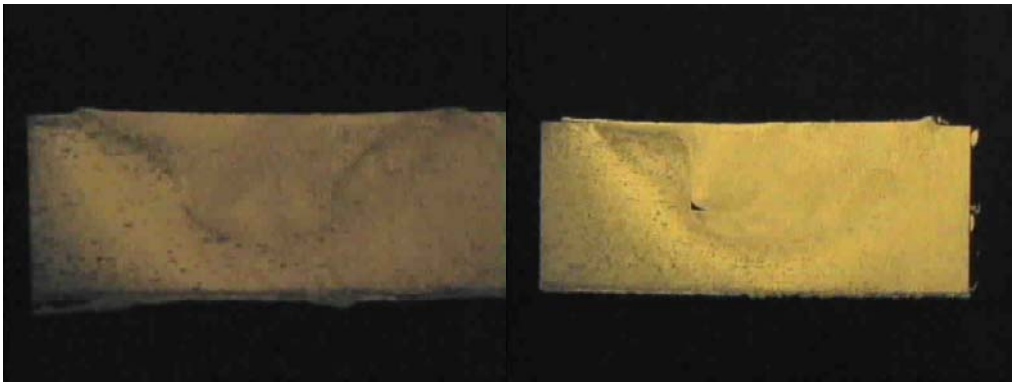

d) 2500 rpm, 16 ipm

Figure 46 (continued)

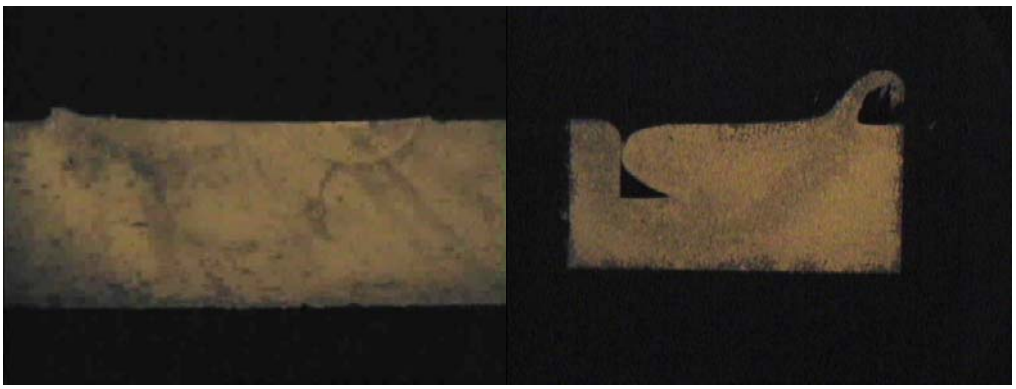

e) 3000 rpm, 16 ipm

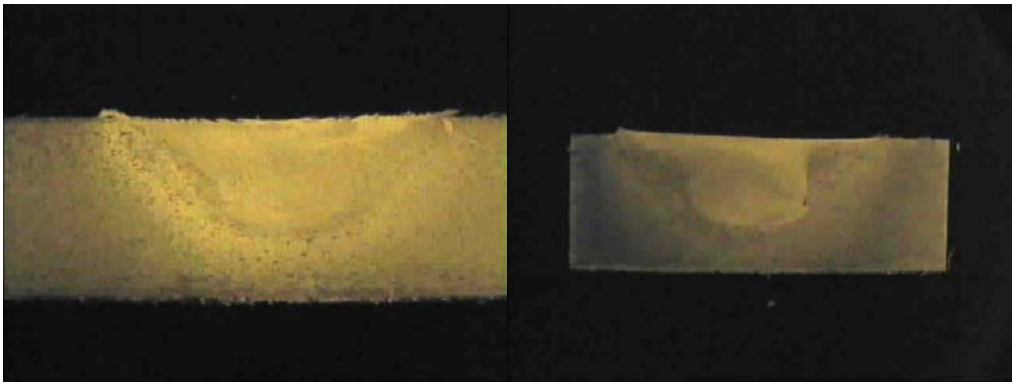

f) 3000 rpm, 30 ipm

Figure 46 Comparison of macrographs for coated (left) and uncoated (right) tools at various parameters.

The macrographs in Figure 46 are for bead on plate, partial penetration welds performed with the coated and uncoated tool at the parameter specified below the paired images. Though a direct comparison does not reveal any major defects in the welds for either condition (with the exception of the uncoated tool at the 3000 rpm, 16 ipm parameter), some subtle differences are apparent. Small wormholes are visible at the root of the nugget in the right image in 47d and f (corresponding to the uncoated tool condition), a defect which indicates deficient plasticization of the material and can be attributed to

excessive travel speed for a particular rotation speed. The heat affected zone (HAZ) also differs slightly in size for the coated tools. The enlargement of the HAZ observed for the macrographs on the left hand side of Figure 46 is related to the difference in thermal conductivities between the tool and the workpiece, a disparity which will be evaluated more thoroughly in the discussion which appears in the final section of this chapter.

The material properties of Molybdenum (the base material upon which the diamond coating is deposited) and the effect they may exert on the welding process must also be considered. Though ideal as a CVD coating substrate, Molybdenum tools have a tendency to flake during machining. Initial welds with the coated tool resulted in a surface with hard Aluminum shavings dispersed along the weld path. This surface structure was distinct from the flash which sometimes accumulates at the perimeter of the weld path (indicating overheating), thus pointing toward a problem with material interface between the tool and workpiece rather than parameter selection. However, once the rotation speed was increased to 1500 rpm or greater, this flakiness disappeared and was replaced by a smooth, mirror-like finish which ran the length of the weld. Figure 47 shows a comparison of the surface texture for selected welds using the coated and uncoated tools. In cases a) and b), the welds produced using the coated and uncoated tool are comparable in surface quality. However, the macrographs previously presented in Figure 46 reveal a wormhole in the weld at parameter b using the uncoated tool; the weld with the coated tool is free of defects at this parameter. For cases c), d), and e), the surface structure of the welds made using the coated tool are superior to those made using the uncoated tool. In c) and d), both of the welds being compared have flash, but the surface of the weld performed using the coated tool has a significantly smoother texture.

In e), the parameter for which the forces experienced by the coated and uncoated tool were most disparate, the coated tool results in a greater amount of flash.

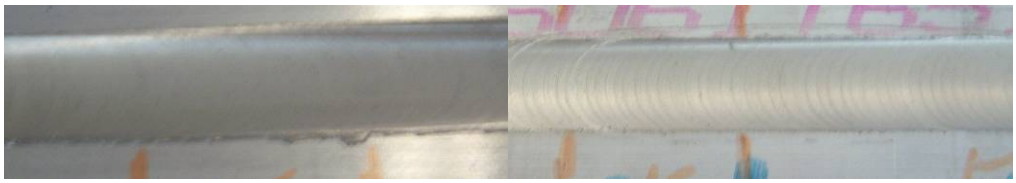

a)1500 rpm, 16 ipm

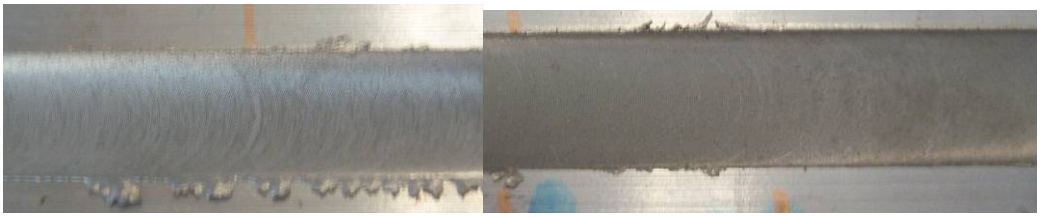

b) 2000 rpm, 16 ipm

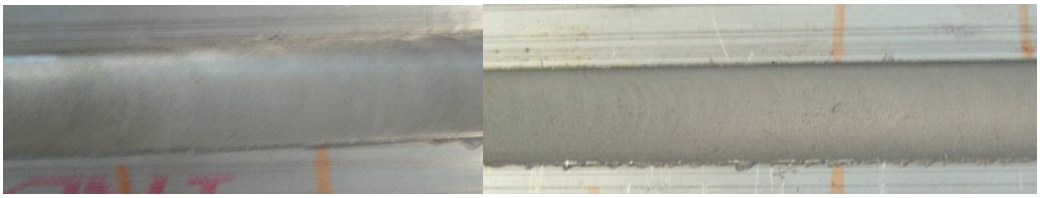

c) 2000 rpm, 20 ipm

d) 2500 rpm, 16 ipm

Figure 47 (continued)

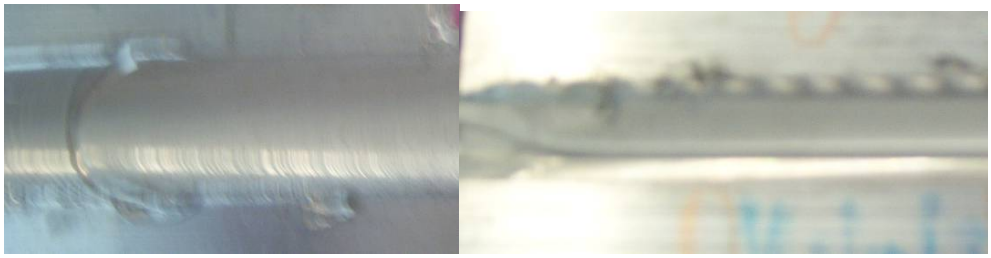

e) 3000 rpm, 16 ipm

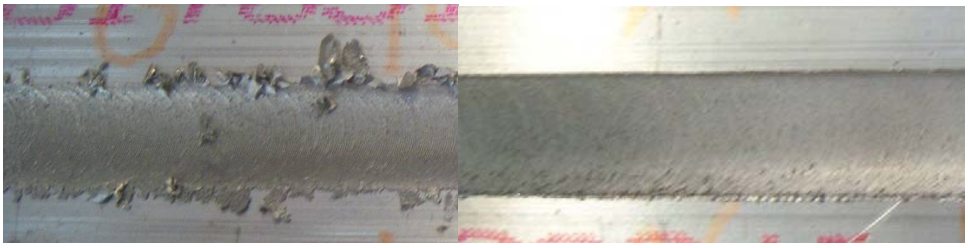

f) 3000 rpm, 30 ipm

Figure 47 Comparison of surface texture for coated (left) and uncoated (right) tools at various parameters.

The results of this section establish that a coated tool can be used in FSW to reduce axial force. The subsequent comparison of the surface structure and macrographs for the coated and uncoated tools at identical parameters demonstrate that the coated tool does not detrimentally alter the composition of the weld. Though partial penetration bead on plate welds can provide a preliminary assessment of force reduction and macrostructural changes attained with coated FSW tools, any future research on this topic should include butt welds, T-joints, lap welds or any other configuration which would allow for the comparative assessment of tensile strength for the coated and uncoated tools. Microscopy is a valid means to qualitatively gauge the "goodness" of a particular weld (and its

importance should not be discounted), but strength testing is the easiest method by which to generate quantitative data. A move to a weld configuration with a true joint line, however, necessitates redesign of the tool. A smooth cylindrical probe does not produce enough downward vertical flow to make a strong weld; hence alternate geometries which incorporate more complex features such as threads, flutes, or flares to enhance vertical flow must be considered. Features such as those mentioned, however, introduce a stress concentration to a Molybdenum substrate which is already susceptible to shear stresses. As expected based on the material properties of Molybdenum, all attempts at the use of a threaded diamond coated probe resulted in failure at the entrance to the material. Thus for probes with features, a less brittle Molybdenum alloy (or another substrate altogether) should be considered as the tool base material.

4.6 Analysis and Conclusions

The CVD diamond coating has a number of properties which suggest it would aid in the joining of materials through Friction Stir Welding (FSW). The hardness of the diamond coating makes it a good candidate for the welding of superabrasive materials such as MMCs. Diamond is the hardest known material (100 on the Rockwell Hardness Scale); consequently, it is expected that a diamond-coated tool would be resistant to the tool wear which plagues conventional tools in MMC welding [29]. This hardness may also contribute to the reduction in axial force, which has the potential to enhance robotic FSW applications. Additionally, diamond has the highest longitudinal sound velocity [29]. Since one potential method of wear detection is the analysis of acoustic emissions by Fourier transforms, this property could be exploited to compare the rate of tool wear

for the diamond-coated Molybdenum tool with that of its steel counterpart. The high thermal conductivity of the diamond coating (20W/cm/^{o}C) may enable it to function as a heat sink, a characteristic which could prove an asset in high-speed welding processes where the high-temperatures attained impose limitations on traditional steel tools [29]. Although diamond is largely inert, it does interact with carbon-based materials; this places restrictions on the materials which can be joined using the proposed tool. The carbon content of iron materials, such as steel, could result in the dissolution of the diamond coating [13]. This tendency to dissolve diamond, coupled with the inability of steel to withstand the CVD chamber, makes steel a poor choice for a base tool material in this investigation. Titanium and its alloys are also unweldable with the diamond-coated Molybdenum tool because Titanium interacts with diamond to form carbides [13]. To prevent this interaction, a shielding mechanism must be devised; the apparatus in the Vanderbilt Welding Laboratory is not currently set up to accommodate such a procedure. Aluminum and Aluminum MMCs appear to be the best choices for joining materials when using the CVD Molybdenum tool.

Returning to the concept of heat transfer, Roy, Nandan, and Debroy propose the factor f, a dimensionless ratio that characterizes how the heat generated by the tool is transmitted between the tool and the workpiece (analogous to the process efficiency factor in arc welding) [28]. The factor f is expressed as:

$$f = [(k\rho C_p)_W]^{1/2} / [(k\rho C_p)_T]^{1/2} \qquad (1)$$

where

k = thermal conductivity

ρ = density of the material

C_p = specific heat at constant pressure [28]

The subscripts W and T refer to the workpiece and tool, respectively.

For the coated case, we will assume the tool has the properties of CVD diamond, since the coating (assuming it does not wear off during the process) is what actually contacts the workpiece material (not the Molybdenum substrate). For diamond at room temperature, k =2000 W/m-K, ρ =3500 kg/m^3 , and C_p = 0.4715 J/g-K. The material properties of CVD diamond are nearly identical to those of diamond (the variation is less than 0.1%), so substituting the values for diamond into equation (1) is justified in this instance [30]. For Aluminum Alloy 6061 in the T6 condition at room temperature, k = 195 W/m-K, ρ = 2705 kg/m^3, and C_p = 0.87 J/g-K [4]. Substituting these values into the Roy equation, we obtain 0.3729. This analysis, though simplistic since k and Cp vary nonlinearly with temperature, predicts that only 37 percent of the heat generated at the tool/workpiece interface will be transported between the tool and the workpiece. This suggests that since a large portion of the heat will be going into the tool, it must be compensated for by rotating the tool at higher spindle speeds. This lends support to the idea that the Molybdenum-coated diamond tool is better-suited for high-speed welding than welding at slower rotation speeds.

The f factor of Roy et al. can be used to evaluate the distribution of heat between the tool and the workpiece for a range of welding temperatures. The thermophysical properties of Aluminum 6061 as a function of temperature are listed in Table 14 (adapted from reference 31). The temperatures considered are consistent with those incurred in a solid-state process, ranging from 25 ^{o}C (room temperature) to 600 ^{o}C (near the melting point).

Table 14 Variation of thermophysical properties of Aluminum alloy 6061-T6 with temperature [31].

Temperature (Celsius)	Density (kg/m^3)	Specific heat (J/K-g)	Thermal Conductivity (W/m-K)
25	2705	0.87	195
100	2695	0.95	195
200	2675	0.98	203
300	2655	1.02	211
400	2635	1.06	212
500	2610	1.15	225
600	2590	1.16	200

The variation of the material properties of diamond with temperature was similarly characterized using information compiled from references 4 and 33. The diamond coating used in this research is actually comprised of two materials: graphite (sp2) and diamond (sp3). Graphite and diamond are allotropes, meaning they have the same elemental composition but differ in molecular arrangement. However, the sp2 content of the coating is deemed too small to appreciably impact material properties [30]. The density of diamond is virtually unaffected by temperature, ranging from 3500 kg/m^3 to 3530 kg/m^3 (a difference of less than one percent over the range of 25 to 600 ^oC). The thermal conductivity of diamond decreases with increasing temperature, a trend depicted in the plot of Figure 48. Note that the variation of the conductivity is asymptotic and converges on a value of approximately 10 W/cm-K for temperatures exceeding 300 ^oC. The largest deviations in thermal conductivity for diamond occur at temperatures below

0 ^{o}C. The red line represents copper, another highly conductive material, and is included merely as a basis for comparison [32].

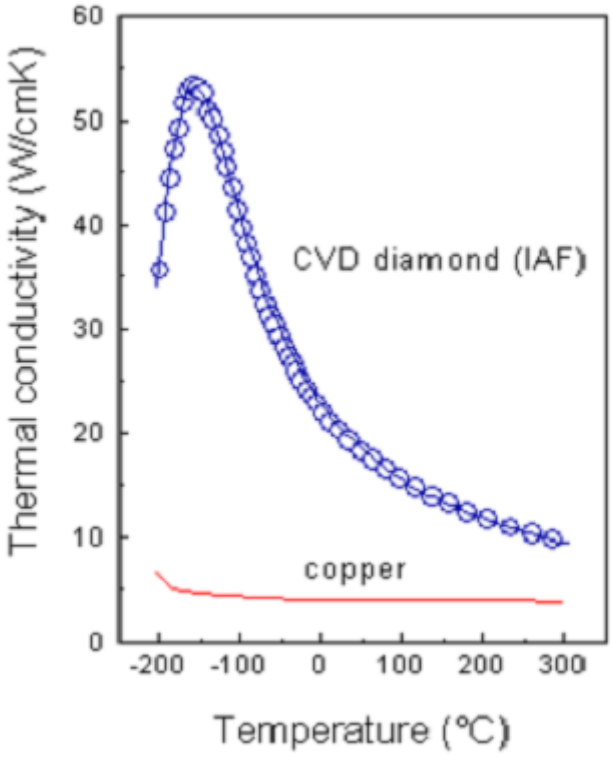

Figure 48 Variation of thermal conductivity with temperature for diamond [32]

The specific heat for diamond is given as 0.5091 J/g-K. We can expect that the specific heat will increase as temperature increases and the molecules become excited, but the exact amount of this escalation is not known. The chemical formula for diamond is C. Based on our knowledge of kinetic theory, this classifies diamond as monatomic, meaning it has only three degrees of freedom (x, y, and z). Linear variation of specific heat is observed when the rotational degrees of freedom are accessed, which usually occurs at room temperature; nonlinearity is associated with the vibrational modes for

higher temperatures (greater than 600 K). Since diamond only has three translational degrees of freedom, it is reasonable to assume that the specific heat of diamond at constant pressure, Cp, is constant with temperature.

Returning to equation (1), it is apparent that the denominator of the dimensionless constant f will change only marginally with temperature. Increasing the rotational speed of the FSW tool so that the temperature of the Aluminum edges closer to the melting point of the workpiece could increase the f value to as much as 0.49. This reduces the heat transfer disparity between the tool and the workpiece, perhaps resulting in an improved joint.

CHAPTER V

PARAMETERIZATION OF FRICTION STIR WELDING OF AL 6061 AND AL 6061/SIC/17.5P FOR TRIVEX TOOL

As outlined in the introduction, one of the goals of this research is to reduce the axial force necessary to produce a structurally sound friction stir weld. In chapter IV, this force reduction was accomplished by means of layering a diamond coating on the smooth probe of an FSW tool. Though the results of the previous chapter established the efficacy of this method, it has two major disadvantages from an industry/cost standpoint. Diamond is an expensive coating material whose use is usually reserved for situations in which the potential benefits justify the extra cost (it remains to be seen if FSW of Al 6061 fits this criterion). Additionally, the susceptibility of the Molybdenum substrate to shear stress precludes the exploration of more complex probe geometries and joint configurations. A less expensive and timely alternative to coatings as a means of force reduction is the use of the Trivex tool, a design patented by The Welding Institute (TWI) in February 2003 [33]. This chapter will focus on the application of the Trivex tool in butt welding of Al 6061 and Al 6061/SiC/17.5p (an Aluminum Metal Matrix Composite). Force data, microscopy, results of tensile tests, and (in the case of the Al-MMCs) periodic measurements of tool wear will be presented. Based on these collective outcomes, an operating window for the use of the Trivex tool in butt welding of these two materials was established.

5.1 Tool Design

The probe of the Trivex tool is approximately triangular in shape. The tool design arose from the FLUENT CFD modeling of Colegrove and Shercliff, who found that it was effective in reducing traverse forces by 18 to 25 percent and axial forces by as much as 12 percent [33]. The surfaces of the probe are convex and the three vertices, when connected, form an equilateral triangle. Each vertex is the center of a circle which contains the other two vertices. The outline of the Trivex shape is clearly illustrated in the two-dimensional top view of the probe which appears in Figure 49.

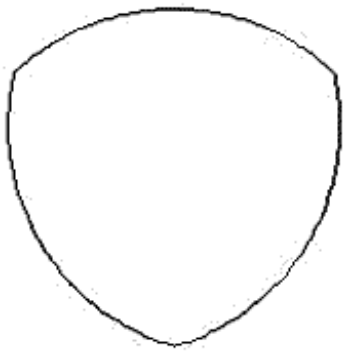

Figure 49 Top view of Trivex probe.

This probe geometry, while still considered a "smooth" probe since it does not have threads or flats, offers several advantages over the cylindrical probe design considered in chapter IV. As in the case of the smooth cylinder, the absence of features in the Trivex tool design eradicates stress concentrations which may result in probe fracture (particularly in abrasive materials such as MMCs). However, unlike the smooth cylindrical probe, the Trivex has a large dynamic volume; that is, the area (and thus volume) of material swept out by the probe is greater than the area of the probe itself.

For a smooth cylinder, the ratio of swept area to probe area is 1; for the Trivex, this ratio increases to 1.25-1.33, depending on the specific dimensions of the probe. This enhanced stirring facilitates increased vertical flow, reducing or eliminating the formation of wormholes (for the proper parameters), the most common defect in welds made using a smooth cylindrical probe. For a more complete comparison of the Trivex probe with other geometries (including the smooth cylindrical), the reader should consult the two papers entitled "Development of Trivex Friction Stir Welding Tool" by Colegrove and Shercliff, the TWI researchers who also hold the patent on this innovation [33].

The steel Trivex tool used in this research had a swept diameter of 0.25" and a probe length of 0.235". The shoulder diameter is 0.75." For this shoulder dimension at a one degree angle of tilt, one hundred percent shoulder contact is attained when the plunge depth is set to 0.009." The weld ligament at these conditions measures slightly less than 0.01", close enough to the backing plate to ensure a full penetration weld yet distant enough to prevent welding the workpiece to the anvil. A three-dimensional CAD drawing of the entire tool is pictured in Figure 50. The tool has a probe at both ends and measures 3.5" in length. The shank of the tool has a diameter of 1", which tapers to the 0.75" shoulder diameter by means of a frustum. The square indentations, measuring 0.5" x 0.5" x 0.1", are used to lock the tool into the set screw configuration summarized in chapter III.

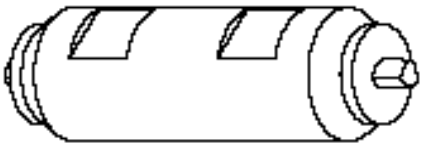

Figure 50 A side view CAD-rendered image of the Trivex tool used in this research.

5.2 Parameter selection for butt welding of Al 6061

The parameters for butt welding of Al 6061 (the unreinforced alloy) were again chosen based on the operational constraints of the laboratory apparatus during the period the research was conducted. The maximum operating speeds of the various motors are summarized in Table 15.

Table 15 Maximum operating speeds for FSW apparatus motors at time of Trivex tool research.

Motor	Maximum operating speed
Spindle	2500 rpm
Traverse	14 ipm
Lateral	2 ipm
Vertical	5 ipm

The corresponding weld matrix for the Trivex tool on Aluminum 6061 appears in Table 16. An "x" indicates parameters for which welds were performed. A "/" identifies parameter sets which were unsuitable due to a mismatch in travel/spindle speed. For

instance, a weld at 13 ipm and 1000 rpm results in a severely deformed surface and excessive flash. Similarly, welds at fast rotation speeds (greater than 2000 rpm) and slower travel speeds (less than 5 ipm) generate an excessive amount of heat, leading to the formation of hard flash along the perimeter of the weld path.

Table 16 Weld matrix for Trivex tool on Al 6061.

		Travel speed (ipm)					
		3	5	7	9	11	13
Spindle Speed (rpm)	1000	X	X	X	X	X	/
	1500	/	X	X	X	X	X
	2000	/	/	X	X	X	X
	2100	/	/	/	X	X	X

5.3 Results: Trends in force data for butt welds of Al 6061 using Trivex tool

The axial force and torque data for butt welds of Aluminum alloy 6061 were compiled using the same method outlined in chapter IV. At this stage of the research, the x and y forces had been decoupled with the assistance of the optical encoder system described in chapter III. Since the x and y forces are no longer sinusoidal, the technique for averaging the peaks summarized in chapter IV becomes unnecessary. Thus the transverse and longitudinal forces for a particular weld parameter can now be determined by simply averaging approximately one thousand points of the steady-state raw data recorded by the dynamometer.

Force plots similar to those in chapter IV were constructed based on the data extracted from the weld matrix in Table 16. Figure 51 is the plot of the force in the x-direction as a function of rotation speed. Each trend line represents a particular travel speed, identified in the legend at the right of the plot. The directionality of the force (indicated by whether the force is positive or negative) is imposed by the decoupling. It is evident that for a constant travel speed, the x force increases with increasing rotation speed. Based on this data, the x force is minimized at parameters with travel and rotation speeds which lie toward the upper right of the weld matrix. The maximum x force is observed for the more extreme parameters in the weld matrix; that is, when both travel and rotation speeds are at the high (lower right) end of the array.

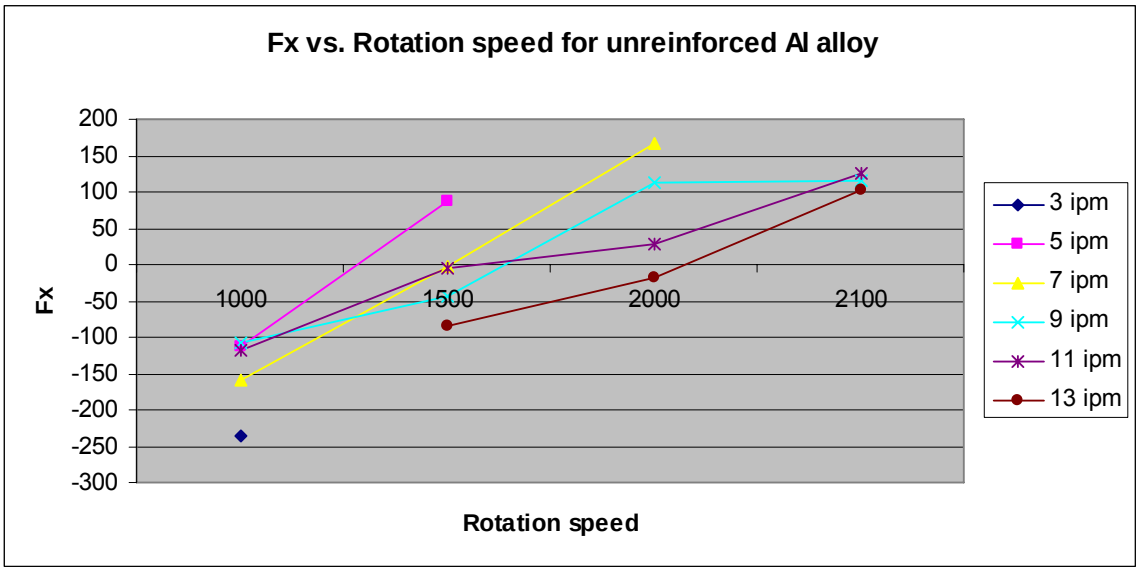

Figure 51 Plot of force in x-direction vs. rotation speed for butt welds of Al 6061 using steel Trivex tool.

The plot of the force in the y direction as a function of rotation speed appears in Figure 52. As in the previous plot, the legend identifies which trendline corresponds to a specific travel speed. It should be noted that the y-forces now take on negative values; this is a consequence of the implementation of the decoupling mechanism previously mentioned. The trends in the y-force data prove more difficult to characterize. For most cases, the magnitude of the y-force is inversely proportional to rotation speed. The trendline for the 11 ipm parameter, however, exhibits a less uniform upward drift. We can conclude that overall, the y-force becomes less negative with increasing rotation speed. This does not necessarily imply that the y-force will approach zero for some sufficiently high rotation speed. As Figure 53 indicates, the slope of the trendlines becomes less steep as rotation speed increases. Though we are hesistant to extrapolate beyond the limits of the weld matrix, it may be the case that some force values (longitudinal, transverse, or axial) converge to a threshold value beyond which there is insubstantial variation with increasing rotation speed. Further study is required to fully characterize this hypothesized variation for the Trivex tool; the data is presented here in the interest of completeness.

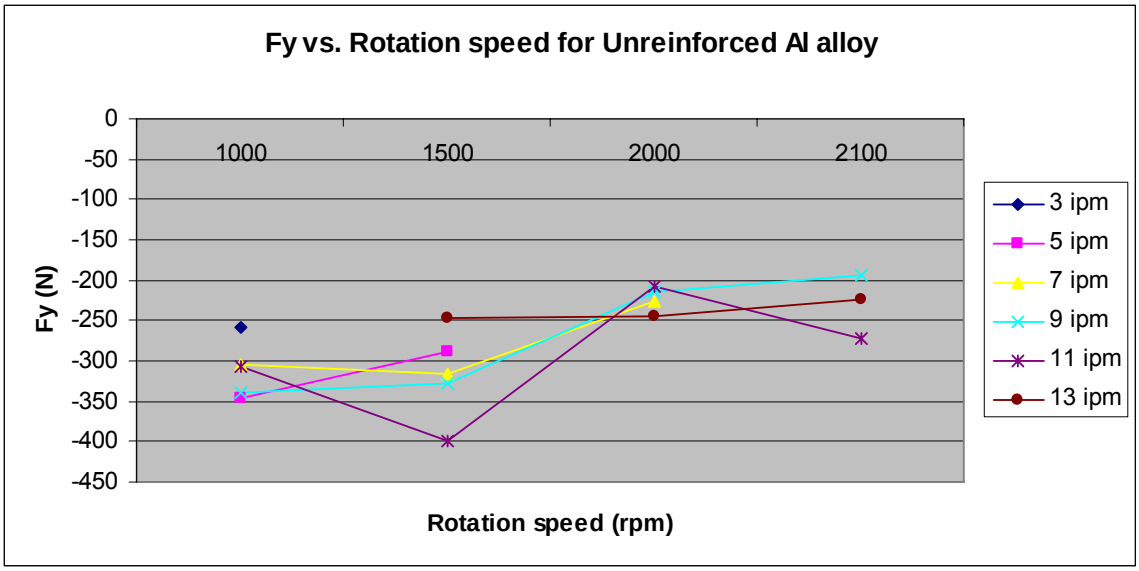

Figure 52 Plot of force in y-direction vs. rotation speed for butt welds of Al 6061 using steel Trivex tool.

Though the longitudinal and traverse force values for the Trivex tool seem significantly lower than those reported for the smooth probe (even in the case of the diamond coating), it is difficult to draw a direct comparison between the data in Figures 51-52 and that presented in chapter IV for a number of reasons. Firstly, the decoupling of the x and y forces posits a significant improvement in the quality of the data (i.e. the force values reported in this chapter are conceivably more accurate and robust than those which appear in the smooth probe plots). Additionally, the gear ratios of the motors have been changed to accommodate lower speeds. As a result, there is virtually no overlap between the weld matrix for the Trivex tool and the smooth probe. Other parameters (aside from rotation and travel speed) have also been altered. The tilt angle has been reduced to one degree and the plunge depth has been increased to 0.009." The weld configuration is also different. As discussed in section 5.1, the Trivex tools are better suited for butt welds owing to their increased dynamic volume. The smooth probe welds

were bead on plate welds at partial penetration (0.004" plunge depth). It is not the intention of this research to quantify the transverse, longitudinal, and axial force reductions which can be attained with the Trivex geometry. The effect of tool geometry on force has been extensively studied by Colgrove and Shercliff in their work on CFD modeling of FSW [33]. The goal of our study is to determine optimal parameters for the use of the Trivex tool in butt welding of Aluminum alloy 6061 (and thereafter measure wear of this tool in the joining of the Al 6061/SiC/17.5 MMC).

Figure 53 displays axial force as a function of rotation speed. As we observed for the data in chapter IV, axial force is inversely proportional to rotation speed. It appears that for the Trivex tool this decrease becomes more pronounced at higher speeds. A more complete discussion of the impact of rotation speed on axial force appears in reference 27 (though we should note the probe geometry considered in that study is threaded rather than Trivex).

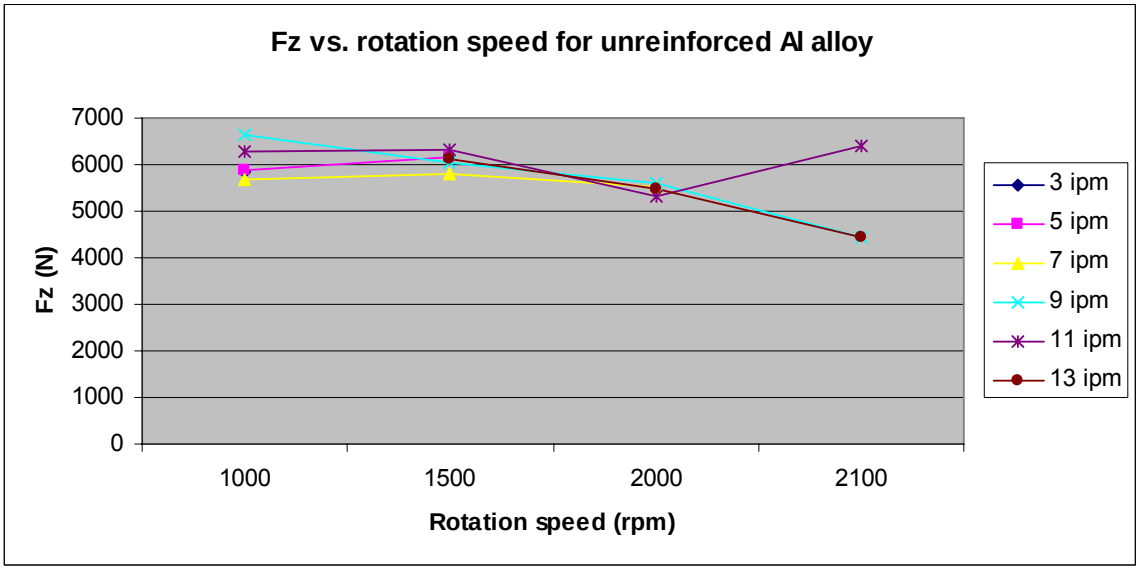

Figure 53 Force in z-direction vs. rotation speed for butt welds of Al 6061 using steel Trivex tool.

The accompanying torque and power data appear in Figures 54 and 55, respectively. Shercliff and Colegrove have demonstrated through CFD that in addition to the more substantial reduction in forces, the Trivex tool also marginally reduces torque, a reduction they attribute to the tool's convex shape [33]. From the power graph in Figure 55, we see that this decrease in torque is more than compensated for by the increase in rotation speed, resulting in a direct proportionality between rotation speed and power for the Trivex tool. Decreased torque also corresponds to smaller (in magnitude) transverse forces, an observation which is unique to the Trivex shape [33].

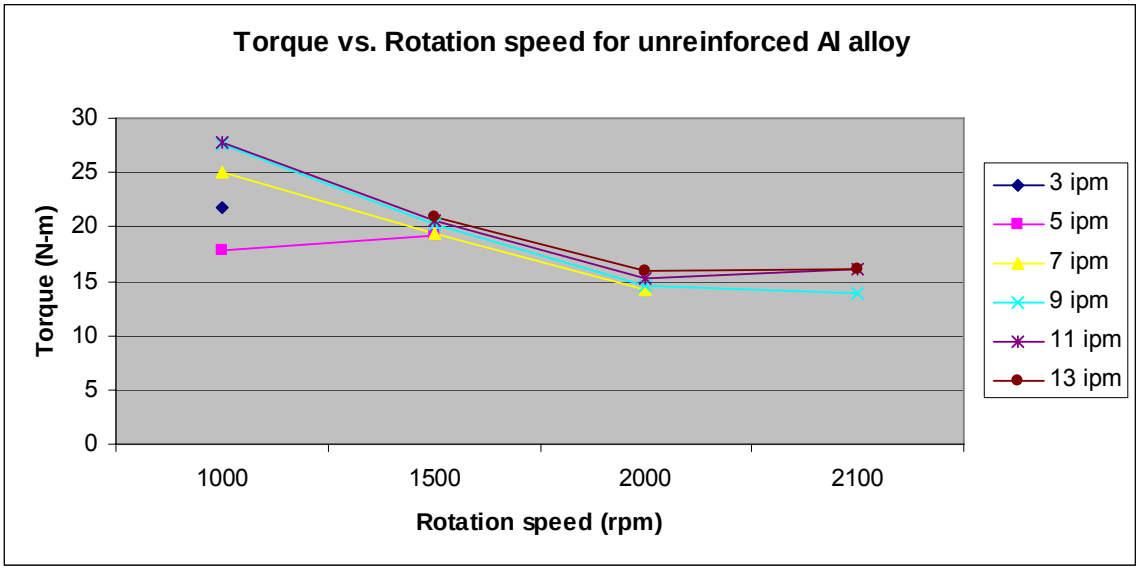

Figure 54 Torque vs. rotation speed for butt welds of Al 6061 using steel Trivex tool.

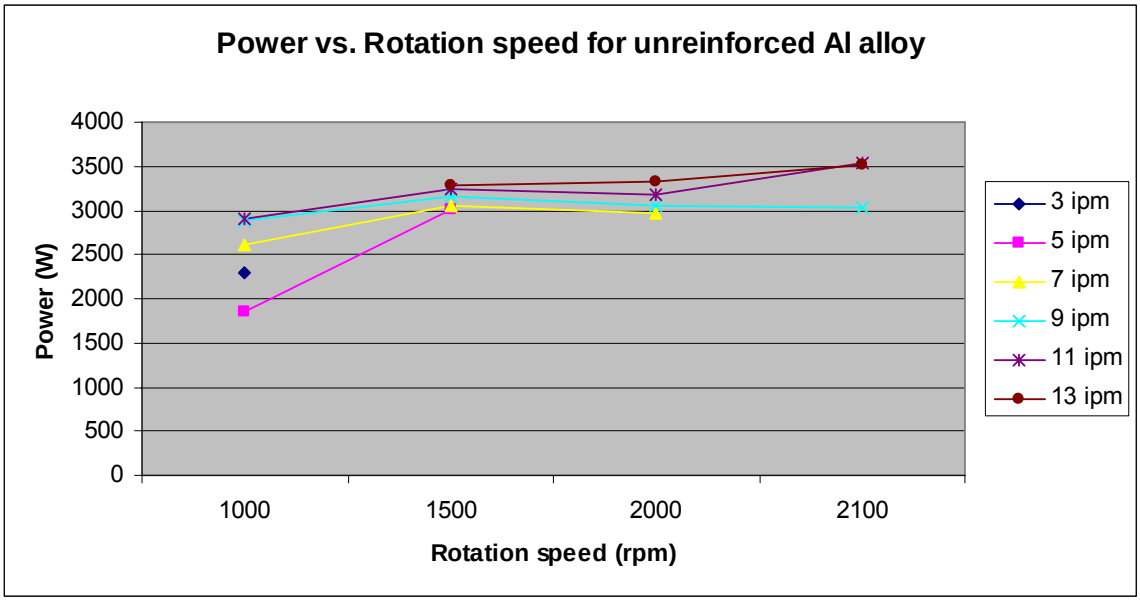

Figure 55 Power vs. rotation speed for butt welds of Al 6061 using steel Trivex tool.

5.4 Parameterization of Trivex tool in butt welding of Al 6061

Although force and torque data can serve as an indication of the flow behavior which governs the interaction between a tool and a workpiece (and is particularly useful from a modeling perspective), they offer little information about the quality of a weld. The parameterization of any tool/workpiece combination must include criteria which can be used to distinguish the parameters which produce superior welds. For this research, we establish three conditions which identify a quality weld:

1) Surface appearance. Ideally, the surface of the weld should have a smooth, mirror-like finish and be free of obvious structural deformities. The presence of flash, a feature which can point to overheating, is undesirable.
2) Joint strength based on the results of tensile tests. The joint efficiency (ratio of the UTS of the joint to the UTS of the parent material) should be greater than seventy percent. UTS denotes ultimate tensile strength and refers to the peak load

(normalized with respect to the cross sectional area of the tensile sample) the specimen is able to withstand during the course of testing. Though not requisite, it is additionally desirable that the specimen fracture in the parent material (rather than along the joint line).

3) Microscopy. When the weld cross sections are etched and analyzed under a microscope, they should be absent of defects (including, but not limited to, cracking, wormholes, voids, and/or hooking). In most cases, a poor tensile test result indicates the presence of a defect. A high joint efficiency, however, does not necessarily preclude the existence of these structural imperfections. We are cautious not to understate the importance of cross-sectioning all samples, even those with favorable tensile test results.

Based on the criteria outlined above, an operating window for the use of the Trivex tool in the butt welding of Al 6061 was established. This window is designated by the shaded region of the weld matrix in Table 17 (at least one weld at each of the shaded parameters was deemed a "good" weld).

Table 17 Operating window (indicated by blue shaded region which contains an "x") for Trivex tool in butt welding of Al 6061. The shaded box without an "x" indicates a weld that satisfied tensile strength criteria, but metallographic analysis revealed a defect.

Travel speed (ipm)

Spindle Speed (rpm)	3 ipm	5 ipm	7 ipm	9 ipm	11 ipm	13 ipm
1000 rpm						
1500 rpm		X	X			
2000 rpm			X	X	X	
2100 rpm					X	X

The operating window in Table 17 was arrived at through evaluation of the finished joints in terms of the three criteria established in this section. With respect to the surface structure, the Trivex tool results in deformed welds at 1000 rpm/7 ipm, 1000 rpm/9 ipm, 1000 rpm/11 ipm, and 1500 rpm/13 ipm. The remaining parameters at which welds were performed produced the desired surface structure. Figure 56 compares a smooth weld surface with that of a distorted weld (characterized by the

presence of flash). Surface images of all welds in the matrix of table 18 can be found in Appendix C.

Figure 56 Comparison of favorable (left) and unfavorable (right) weld surfaces. Left image corresponds to 1000 rpm/5 ipm; the right image is the 1000 rpm/7ipm case.

All joints were tensile tested and the results of this analysis are presented in Figures 57 and 58. Figure 57 shows how the peak load (in kgf) varies with increasing rotation speed. Figure 58 displays the corresponding peak stress for each parameter. Peak stress is simply the peak load divided by the cross sectional area of the specimen; stress is thus expressed in units of pressure (MPa). The graphs indicate that even a minute change in parameters can have a dramatic impact on the load the joint is able to withstand before fracturing. For instance, decreasing the travel speed from 11 ipm to 9 ipm at 2100 rpm translates into a fifty-eight percent reduction in peak stress.

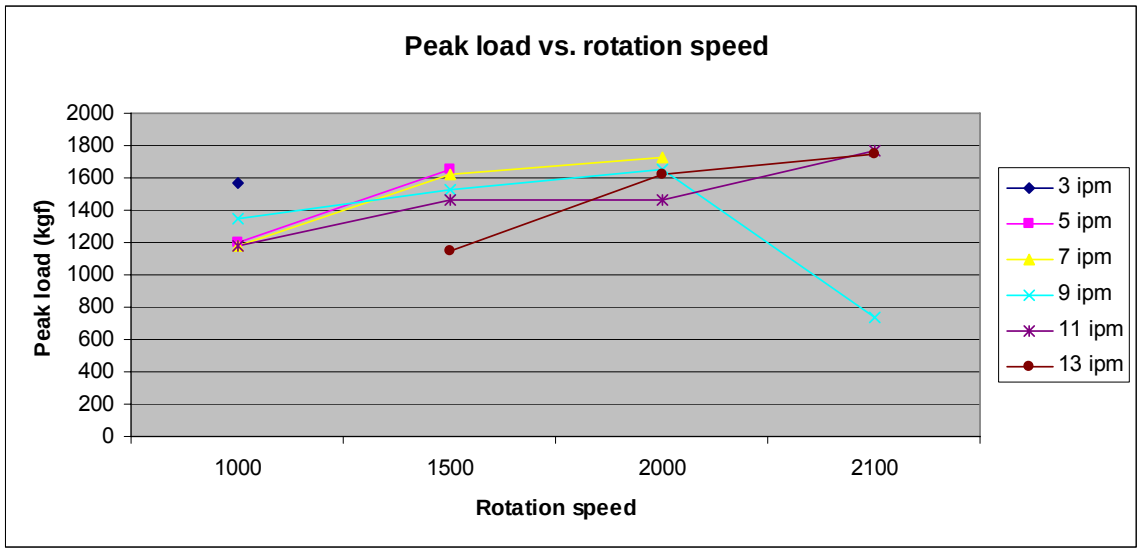

Figure 57 Peak load vs. rotation speed for butt welds of Al 6061 using Trivex tool.

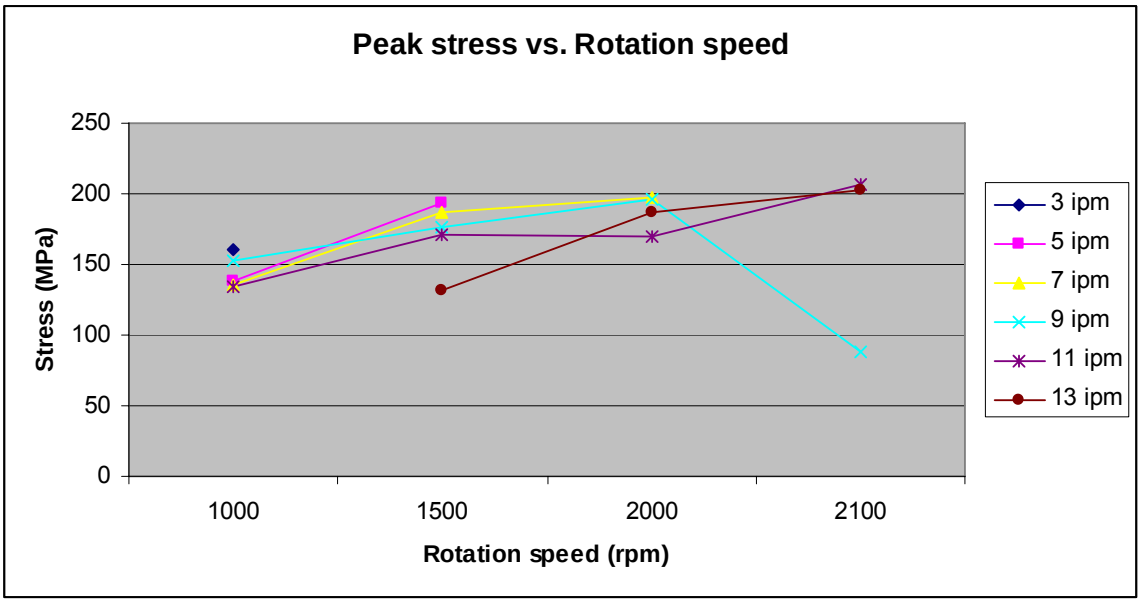

Figure 58 Peak stress vs. rotation speed for butt welds of Al 6061 using Trivex tool.

Based on the standards set forth earlier in this section, a joint efficiency of greater than 70 percent is considered satisfactory. The macrostructure of the welds that met

this condition were analyzed. Those with defects were subsequently eliminated; the remaining welds comprise the operating window charted in Table 18. Microscopic images of the macrographs for the acceptable welds are shown in Figure 59.

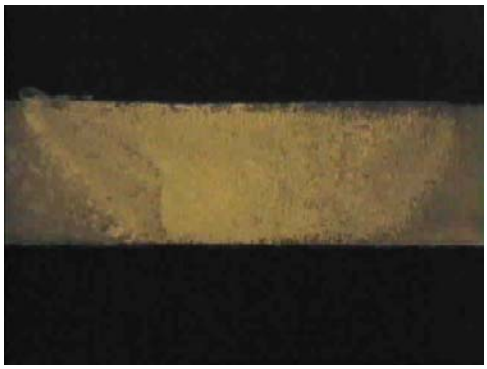

a) 1500 rpm, 5 ipm

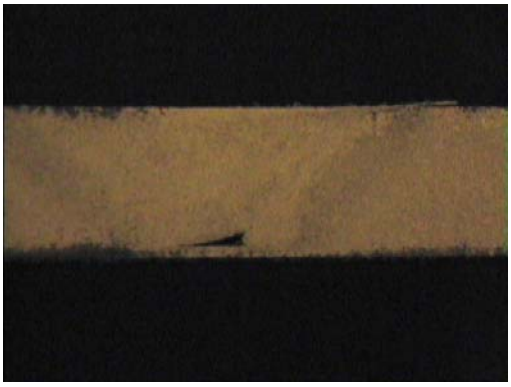

b) 1500 rpm, 7 ipm

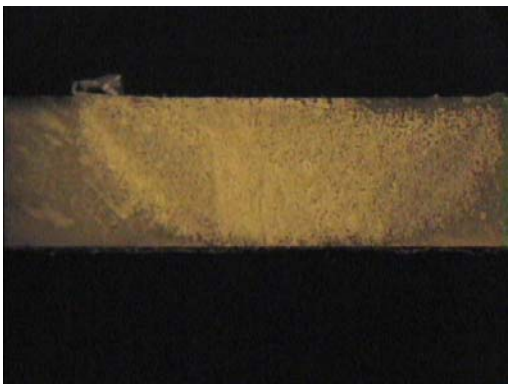

c) 2000 rpm, 7 ipm

d) 2000 rpm, 9 ipm

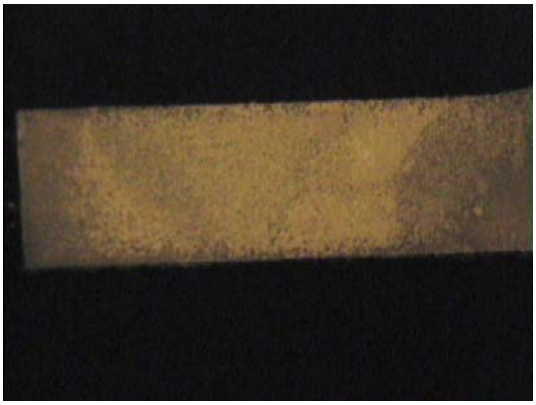

e) 2100 rpm, 11 ipm

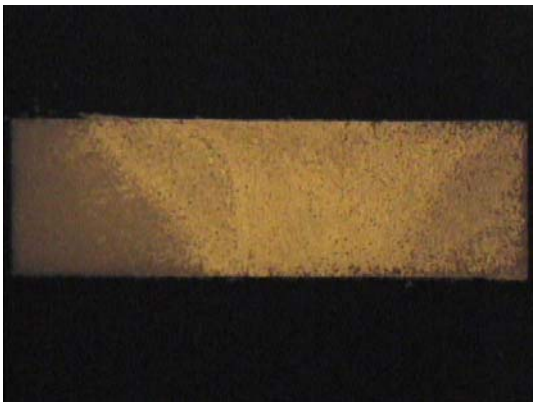

f) 2100 rpm, 13 ipm

Figure 59 Macrograph images of welds in operating window for Trivex tool on Al 6061.

5.4 Wear study of Trivex tool in butt welding of Al 6061/SiC/17.5p

As addressed in the literature review of chapter II, Metal Matrix Composites (MMCs) are superabrasive materials valued for their high strength to weight ratio. Due to their high cost and difficulty to machine, MMCs remain a largely application driven industry, typically reserved for use in structures where the added strength justifies the extra investment. As a result, MMCs most commonly find use in the fields of defense, aerospace, or high performance automobiles.

The problems inherent in the joining of MMCs were outlined extensively in chapter II. A fusion welded MMC joint is characterized by porosities in the heat affected zone, the dissolution of reinforcing particles, and the formation of a deleterious theta phase (Al_4C_3) caused by localized melting. Though Storjahnn, et. al. found that these effects could be mitigated somewhat by careful control of heat input, a solid-state joining process such as FSW is a more viable alternative [15]. The autogenous nature of FSW also enhances repeatability by eliminating the element of human control.

Though FSW is preferred to fusion welding for the reasons mentioned above, FSW poses its own set of unique problems in this particular application. The primary limiting factor in the FSW of MMCs is tool wear. A current area of research lies in the development of methods to combat tool wear (by means of coatings, variations in tool geometry, or the use of functionally gradient materials). As established by Diwan, the weldability of a particular MMC is inversely proportional to its percentage reinforcement. The 17.5 percent reinforcement of the composite in our study places the material on the lower end of the spectrum. This classification indicates that while a substantial amount

of wear is still to be expected, the wear will not be as severe as in the case of a material with a greater reinforcement percentage.

A preliminary wear study of the steel Trivex tool in the butt welding of Al 6061/SiC/17.5p was conducted using the VUWAL test bed. The parameters studied were 1000 rpm/4ipm, 1000 rpm/10 ipm, 1350 rpm/4ipm, and 1350 rpm/10ipm. These parameter sets were chosen to assess the influence of travel and rotation speeds on the tool's wear rate. A separate tool was used for each parameter set (although each of the four tools had identical geometry, were fabricated from the same material, and subjected to an equivalent heat treatment process). The plunge depth (.009") and tilt angle (one degree) remained constant for all welds. After each 9 inch butt weld, the tool was removed from the apparatus, any Aluminum accumulated on the probe was brushed off using a grinder, and measurements of probe diameter and length were recorded. A shadowgraph image was also taken. This procedure was repeated for a given parameter until no additional wear was observed, indicating that the tool had reached the "self-optimized shape" described in the work of Prado, et al [26].

The shadowgraph images detailing the wear of the Trivex tool for the four parameters considered appear in Figures 60 through 63. The measurement below each image corresponds to the length of weldment. The leftmost photo in each figure is the appearance of the probe prior to welding, while the rightmost shows the probe shape after 36 inches of weld (equivalent to four butt welds).

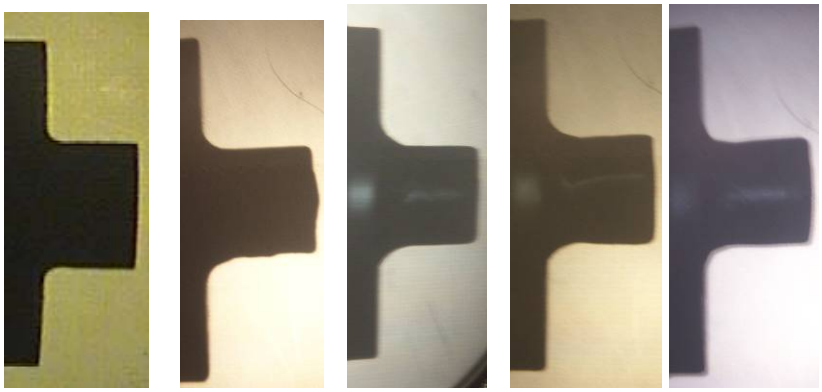

0 in 9 in 18 in. 27 in. 36 in.

Figure 60 Wear of Trivex tool for butt welding of Al 6061/SiC/17.5p at 1000 rpm and 4 ipm.

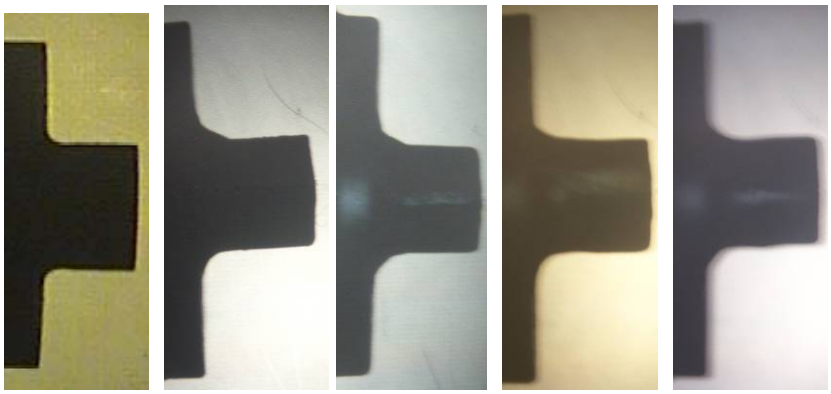

0 in 9 in 18 in. 27 in. 36 in.

Figure 61 Wear of Trivex tool for butt welding of Al 6061/SiC/17.5p at 1000 rpm and 10 ipm.

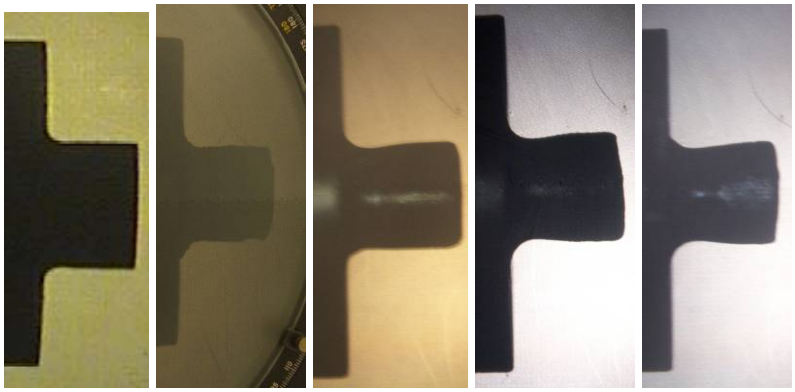

0 in 9 in 18 in 27 in 36 in

Figure 62 Wear of Trivex tool for butt welding of Al 6061/SiC/17.5p at 1350 rpm and 4 ipm.

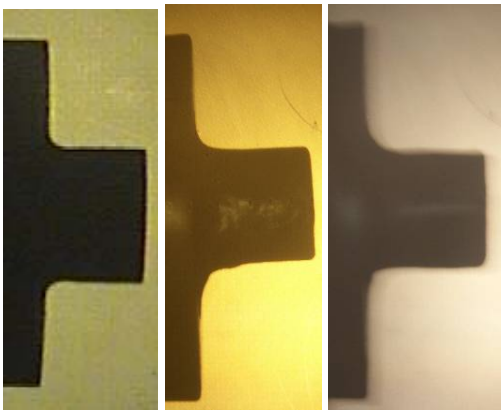

0 in 9 in 36 in

Figure 63 Wear of Trivex tool for butt welding of Al 6061/SiC/17.5p at 1350 rpm and 10 ipm.

The probe diameter and length were measured to within 0.001" following each weld. The percent reduction in probe diameter and length as a function of weld length for the parameters considered are plotted in Figures 64 and 65, respectively.

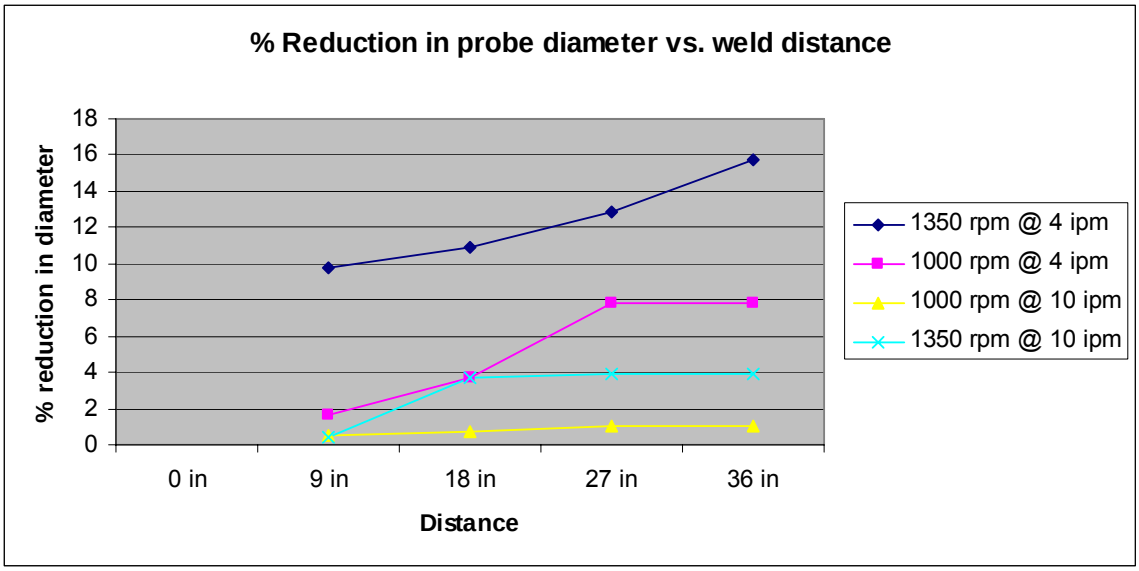

Figure 64 Percent reduction in probe diameter vs. weld distance for Trivex tool in butt welding of Al 6061/SiC/17.5p.

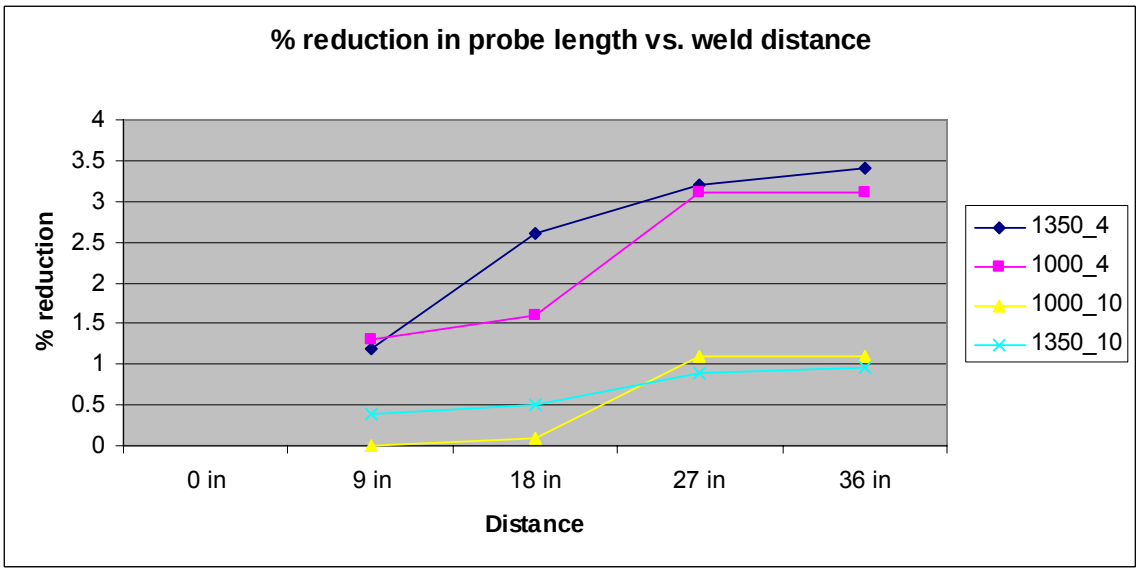

Figure 65 Percent reduction in probe length vs. weld distance for Trivex tool in butt welding of Al 6061/SiC/17.5p.

From the plots above, we can conclude that for the parameters studied, higher travel speeds result in less wear. This is a plausible result that is consistent with the previous wear studies of Prado et al [26]. The faster the travel speed, the less time the

tool is in contact with the material and the less opportunity the probe has to encounter the abrasive reinforcement particles which are responsible for wear. In comparing parameters which have the same travel rate (for example 1350 rpm/4 ipm and 1350 rpm/10 ipm), the parameter with the higher rotation rate will result in greater deterioration of probe dimensions. This can presumably be attributed to increased contact with the material, the mechanism previously proposed as an explanation for why an upsurge in wear is observed at decreased travel speeds. Based on these results, the condition for maximum tool wear seems to correspond to higher rotation speeds and lower travel speeds. Minimal tool wear is observed for the converse parameters (slower rotation speeds and faster travel speeds).

Visual confirmation of these conclusions can be seen in the shadowgraph images of Figures 60 through 63. Figure 62 shows the shadowgraphs for the parameter set 1350 rpm/4 ipm (which we established resulted in the most dramatic tool wear). If we compare the rightmost image of Figure 62 with that for the other parameters, it is apparent that the reduction in probe diameter at 1350 rpm/4 ipm is substantial enough to produce a noticeable "necking" effect, marked by the rounded edges at the interface where the probe contacts the shoulder. The reduction in probe diameter in Figures 61 and 63 (which match up with the 1000 rpm/10 ipm and 1350 rpm/10 ipm parameter sets, respectively) is much less appreciable.

The shape of the tool is said to be optimized when it has reached some threshold weld length beyond which no wear occurs. For our study, this length is typically in the range of 18 to 27 inches, a distance equivalent to two to three butt welds of Al 6061/SiC/17.5p. The exception to this is the tool at the 1350 rpm/4ipm parameter, which

experiences the most severe wear and also requires a longer weldment (relative to the tools at the other parameters) to arrive at the self-optimized shape. This shape, in which the probe begins to resemble an hourglass, is represented by the final shadowgraph images of Figures 60 through 63 as well as the plateaus of the trendlines in Figures 64 and 65. The term "self-optimized" shape, however, is somewhat of a misnomer. The phrase refers merely to the shape of the tool produced by wear, not necessarily the shape which will result in a strong weld. In fact, the self-optimized shape tends to produce large wormholes, defects which are clearly visible in the macrographs of Figure 66. These could be a consequence of poor parameter selection (the travel speeds considered here may be too rapid to ensure proper consolidation of material). The formation of wormholes may also be due to decreased vertical flow associated with the wear of the probe; consult reference 25 for a more complete discussion of how wear can fundamentally alter the flowfield surrounding the tool.

a b

Figure 66 Macrographs of welds with self-optimized tool shape. a) 1350 rpm/10 ipm, b) 1000 rpm/10 ipm.

There are some shortcomings to our research methodology that should be noted. In the case of the Trivex tool, methods which rely on optical comparators as a qualitative measurement of tool wear present some limitations. The shadowgraph generates only a two-dimensional image and hence is not able to accurately capture the Trivex geometry. This is evident in the "before" images of Figures 60 through 63, in which the Trivex probe appears in profile as a smooth cylinder. Another problem with the shadowgraph method is its inability to reflect the often asymmetric manner in which wear occurs. During the course of the study, an effort was made to take each shadowgraph image from the same angle and at the same magnification. Thus while the shadowgraph images are effective at conveying the wear on one face of the tool, they reveal nothing about the progression of wear at other locations.

The dimensions of the tool were measured periodically using a digital micrometer; this data serves as the basis for the plots in Figures 64 and 65. Because the tool wears asymmetrically, measurements are location dependent. That is, the probe length at one point on the tool may or may not be equal to the length measured at another point. The non-cylindrical Trivex geometry makes it difficult to obtain a representative value for the probe diameter. The values used in the calculation of diameter and probe reduction were typically an average of three measurements taken at various locations on the tool. Additionally, our measurements do not account for wear of the shoulder. If shoulder wear occurs, it would translate into a consistent underestimation of the reduction in probe length. Severe shoulder wear could even produce data that would indicate the probe is becoming longer with successive welds (a nonsensical result). For future

research into tool wear, a more robust method of measurement (such as the imaging technique employed by Prado, et al.) is recommended [26].

The central issue in joining any MMC is negotiating the compromise between tool wear and weld quality. Welding speeds must be slow enough to generate sufficient plastic deformation to produce a good weld, yet fast enough to mitigate severe tool wear. This concept will be explored more thoroughly in the section which follows.

5.5 Parameterization of Trivex tool in butt welding of Al 6061/SiC/17.5p

Once the tool had reached its self-optimized shape and no further wear was observed, the tool was used in a parameterization study of Al 6061/SiC/17.5p, the Aluminum Metal Matrix Composite material provided by DWA Composites, a materials supplier located in northern California. The weld matrix for this investigation appears in Table 18. Note that the rotation and travel speeds considered are significantly lower than those of the weld matrix for the unreinforced alloy, Al 6061. These reduced travel and spindle speeds were based on existing parameterization studies for Aluminum alloys with reinforcement; the results of several such studies are summarized in the literature review of chapter II.

Table 18 Weld matrix for Trivex tool (self-optimized shape) on Al 6061/SiC/17.5p.

Spindle Speed (rpm)	Travel speed (ipm)			
	3 ipm	5 ipm	7 ipm	9 ipm
500 rpm	*	*	*	*
750 rpm	*	*	*	*
1000 rpm	X	X	X	X
1250 rpm	X	X	X	X
1500 rpm	/	X	X	X

An "X" is used to indicate the parameters for which welds were performed. "*" represents an apparatus limit with respect to spindle speed. The VUWAL apparatus is not currently configured for the lower rotation speeds (less than 1000 rpm) commonly encountered in the literature on FSW of MMCs. At present, 750 rpm seems to be the lower limit of the VUWAL spindle setup. Attempts to perform welds at this rotation speed (or lower) produce a loud droning sound, presumably an indication that the motor is operating below its rated speed.

Though force and torque data were recorded for all welds in the Table 19 matrix, the data is largely unusable beyond determining maxima for Fx, Fy, Fz, and torque. When plotted against time for a given parameter, the longitudinal and transverse forces exhibit oscillatory behavior, sometimes on the order of thousands of Newtons. This could be due to the abrasive nature of the material, in which case a spike in Fx or Fy would correspond to the tool's contact with a concentration of SiC particles. The oscillations may also be attributable to misalignment in the butt joint. The composite

material is initially in 84" long x 12" wide x ¼" thick sheets which are cut into the 9" long x 3" wide x ¼" thick strips used for butt welds. The extreme stiffness of the material makes it incredibly difficult to machine; consequently the cuts are often uneven. When selecting two strips to join, it is not always possible to ensure either a perfect fit or a straight joint line. Thus, gapping and/or variation along the path of the joint line may be responsible for the inconsistencies in the x and y forces.

Additionally, it is difficult to determine average values for steady state axial force and torque at the slower travel speeds (three inches per minute) considered. In this instance, the "creep" (the reduced speed at which the tool enters the material to generate sufficient heat for plasticization) is only slightly less than the actual weld speed. The "ramp" on the force graph which indicates the transition between the "creep" phase and the weld is thus absent, making it difficult to distinguish which values comprise the steady state condition. With these caveats stated, the average force and torque values for butt welds of the Trivex (self-optimized shape) on Al 6061/SiC/17.5p do not display the consistent trends associated with butt welds of the tool on Al 6061 (section 5.4). The force data for the MMC welds will be presented more completely in chapter VI, where they will serve as the inputs for a finite element model to predict tool deformation and stress.

The surfaces of the butt welds of Al 6061/SiC/17.5p have a rougher texture than those of Al 6061 discussed in the previous section. The composite material is coarser in the pre-welded state than its unreinforced counterpart, which may account for the difference in as-welded surface consistency between the materials. The typical surface structure of a Al 6061/SiC/17.5p butt joint is pictured in Figure 67.

Figure 67 Welded surface of Al 6061/SiC/17.5p. Performed at 1250 rpm, 3 ipm using Trivex tool with self-optimized shape.

The abrasive nature of Al 6061/SiC/17.5p precludes tensile testing as a quantitative measure of joint efficiency. Characteristic sections of the welds were cut using a diamond saw, but were unable to be milled into the tensile test samples sketched in Figure 28 using conventional machining methods. Waterjet cutting or electron discharge machining (EDM) are possible options for any future research which may require an assessment of joint strength.

Since no tensile data was collected, it was necessary to cross-section all welds in the matrix of table 18 using the method outlined in chapter III. Since the shape of the self-optimized Trivex tool is effectively the same as that of a smooth probe, it is expected that a majority of the welds will exhibit wormhole defects. The operating window for the butt welding of Al 6061/SiC/17.5p is thus comprised of those welds that were deemed "defect-free." The weld envelope (a term synonymous with operating window) is designated by the blue shaded region of Table 19. The accompanying macrographs appear in Figure 68.

Table 19 Operating window (indicated by blue shaded region) for Trivex tool (self-optimized shape) in butt welding of Al 6061/SiC/17.5p.

	3 ipm	5 ipm	7 ipm	9 ipm
1000 rpm	X			
1250 rpm	X	X		
1500 rpm		X		

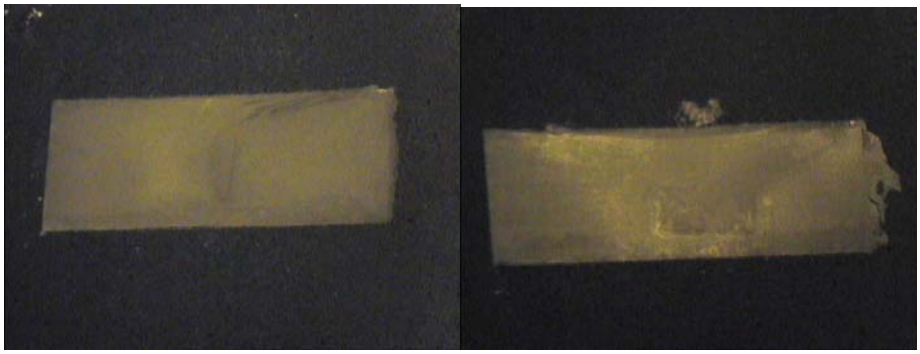

Figure 68 Sample macrographs for "good" welds at parameters in weld envelope. Corresponding parameters are 1250 rpm, 3 ipm (left) and 1000 rpm, 3 ipm (right).

Though a defect-free weld is a promising result, it is by no means a guarantee of joint strength. For this reason, it is essential that the welds be subjected to mechanical testing before any further conclusions about optimal parameters are drawn.

5.6 Future research

The ultimate purpose of the research presented in this chapter is to serve as a baseline for comparison with future results obtained using a diamond-coated Trivex tool. As briefly discussed in chapter IV, the major obstacle to such an investigation lies in the selection of a suitable substrate. Though Molybdenum is the best material from a coating perspective (i.e. it can withstand the heat of the coating chamber and diamond adheres to

it readily), its brittleness makes it inappropriate for use in machining processes. The fracture problem observed in use of the smooth probe diamond coated tool on Al 6061 is only exacerbated by attempts to weld its reinforced counterpart. In most instances, the probe shears off at the entrance to the material. It may be possible to lessen this shearing effect by milling a slot slightly larger than the probe diameter at the start of the joint line. This will ensure that the shoulder fully contacts the material before the probe, generating enough heat to plasticize the localized material and reduce the stress on the probe as it creeps into the joint. For the same reason, it may also be beneficial to decrease the "creep" speed in order to extend the time the probe dwells in the material before the weld commences.

Because of the problems which accompany the choice of Molybdenum as a base material, it may be worthwhile to consider an alternative substrate. Though steel was previously discarded as a substrate candidate because of its carbon constituency, it may be possible to coat steel if an intermediate layer, such as Chromium Nitride (CrN), is deposited first. It is likely that welding with tools fabricated from Tungsten (W) or Tungsten Carbide (WC) will present the same brittleness problems as Molybdenum. It is possible to obtain Molybdenum or Tungsten alloyed with another element, such as Rhenium (which improves resistance to shear stress), but these materials are expensive and nearly as difficult to machine as their unalloyed counterparts. When due consideration is given to both cost and material properties, it seems that tools of high-speed steel coated with CrN and subsequently diamond are the most viable option and consequently the direction in which any future research on this topic will proceed.

The potential outcomes for the use of a coated tool are promising. The results of chapter IV demonstrate that a coated tool can significantly reduce the values of force and torque in the welding of Al 6061. It may be that a similar force reduction will be observed when the coated tool is applied to Al 6061/SiC/17.5p. Additionally, it is hoped that the coated tool will exhibit decreased wear. Though tool wear is little more than a peripheral concern in the joining of Aluminum alloys, it is the limiting factor in the welding of Metal Matrix Composites. As such, any innovation which can be shown to reduce the wear rate of tools in these materials would be of considerable benefit to the industry.

CHAPTER VI

FINITE ELEMENT MODEL OF TOOL DEFORMATION AND STRESS BASED ON FORCE DATA

The focus of this chapter is to construct and implement a finite element model of tool deformation and stress during the Friction Stir Welding process. By emphasizing the modeling aspect of FSW research, we do not wish to discount the value of experimental work presented in chapters IV and V. Much can be learned about a process by physically varying the parameters and analyzing the effect these changes have on the data obtained. There is, however, error (be it human or otherwise) that is inherent in any experimental procedure. This is not to say that modeling eliminates error; is it relatively common for models to generate outcomes which do not fully agree with those obtained through experimentation. This divergence from experimental results can usually be attributed to assumptions made during the model's development stages. A simple FEA method to model deformation and/or stress is perhaps most advantageous from an industry cost standpoint in that it would enable researchers to predict the wear behavior for a given tool/workpiece material combination while minimizing experimentation that is both time consuming and, in the case of Metal Matrix Composites, destructive. The model presented here is a three-dimensional static model in which forces obtained from the dynamometer are applied to the probe and shoulder in order to produce a "snapshot" of tool deformation and stress for various welding parameters.

6.1 An Overview of the Finite Element Method

Finite element analysis (FEA) is a numerical method developed to analyze engineering problems for which a closed form solution does not exist. The method involves dividing a body into discrete elements connected by nodes. The behavior at each node can then be analyzed. In this manner, FEA can be used to characterize the behavior of the structure as a whole. The major advantages of FEA are the ability to model irregularly shaped bodies as well as those comprised of several different materials, handle any number and type of boundary conditions, and save time and money that would be required for large-scale experimentation on a structure [34].

There are essentially eight steps in any finite element analysis:

1) In discretization, the body is divided into elements linked by nodes. For a two-dimensional analysis, common elements include multi-noded line elements (used to represent bars or beams), triangular, and quadrilateral elements. Three-dimensional elements include tetrahedrals, hexahedrals, wedges, etc. and may be regular or irregularly shaped depending upon the geometry of the structure being modeled. The choice and number of elements depends on the nature of the structure under consideration as well as the level of accuracy desired. It is common engineering practice to use more elements with smaller dimensions in areas where stresses, displacements, or temperatures are expected to be changing or at a maximum (locations where a high level of accuracy is desired). Fewer elements with larger dimensions are appropriate for regions where results are expected to be largely unchanging.

Together, the elements and nodes of a structure comprise what is referred to as the mesh. The usability of a finite element analysis hinges largely on the choice of elements and the level of mesh refinement. To assess mesh refinement, a sequence of analyses is conducted in which the number of elements is successively increased (or decreased). When the results of the analyses converge, the mesh is said to be sufficiently refined. It should be noted that refinement is not an indicator of the accuracy of the model, but a check performed as a way to minimize computational time. For instance, we may be able to reduce the number of tetrahedral elements in a structure from 2500 to 1500 without appreciably altering the results. This issue is of particular importance when using a finite element computer package.

2) A nodal function is selected which expresses displacement in terms of the nodal variables (x, y, and z for the three-dimensional case). Depending on the type of element, a linear, quadratic, cubic, quartic, or even trigonometric function may be chosen [35]. The same displacement function is applied to each element, thus utilizing discrete methods to characterize a quantity which is ultimately continuous.
3) A relationship relating strain to displacement and stress to strain is now defined. In the simplest case, strain in the x-direction as a function of displacement is written as $\varepsilon_x = du/dx$. Stress and strain are then related by Hooke's law, $\sigma_x = E\,\varepsilon_x$, where E denotes Young's modulus of elasticity.
4) The stiffness matrix, k, is derived using the direct equilibrium method, work/energy methods, or Galerkin's method (weighted residuals). For one-

dimensional elements, the direct equilibrium method is easily applied. Existing relationships between local forces and deformations are exploited to express nodal forces as a product of nodal displacements and k. Work/energy methods that can be used to derive the stiffness matrix include minimum potential energy, the principle of virtual work, and Castigliano's method. Galerkin's method relies primarily on the use of weighting functions. For further details on deriving an element stiffness matrix using the methods briefly outlined above, the reader should consult reference [34].

5) The equations generated in the above step are assembled into a global stiffness matrix, K, which relates global forces to global displacements. Because K is always a singular matrix, we must impose appropriate boundary conditions on the structure before it is possible to solve the system.
6) The system of equations given by $\{F\} = [K] \{d\}$ is solved using a method from linear algebra. Note that a quantity in square brackets represents an n x n square matrix, while a quantity surrounded by curved brackets denotes an n x m column matrix.
7) The values for displacements can then be used to calculate strain and subsequently stress using the relationships defined in step 3.
8) The results of the finite element analysis are interpreted.

The steps outlined above are best suited for general loading conditions which are static in nature. When dynamic effects are considered, a consistent mass matrix for each element must be developed to account for time dependence. This matrix, [M], is specific to the

type of element and is derived using the principle of virtual work. For a complete discussion of the consistent mass matrix, consult chapter 16 of reference [34]. The governing equation in step (6) thus becomes $\{F(t)\} = [K]\{d\} + [M]\{d\}$. Hence, a finite element solution for a dynamic system must include a procedure to calculate nodal displacements, $\{d\}$, at incremental values of time (referred to in the FEA lexicon as time steps). There are three primary methods of direct integration using time steps: the central difference method, the Newmark-Beta method, and the Wilson-Theta method. The latter two are sophisticated algorithims which are used in many commercial FEA codes.

6.2 NASTRAN as Finite Element Solver

The finite element software package NASTRAN was used to carry out a finite element analysis of the FSW tool. NASTRAN is the finite element solver which evaluates the stiffness matrix and solves for displacements and stresses. Pre-processing (constructing and meshing the geometry) and post-processing of results is done in PATRAN. The steps of a typical finite element analysis using NASTRAN is outlined below:

1) The geometry is either built in PATRAN or imported from a CAD program.
2) The geometry is meshed. The element verification feature in PATRAN can be used to provide a preliminary assessment of the quality of the mesh.
3) The material properties of the geometry are specified. These can be selected from an existing library or input directly by the user.
4) The boundary conditions for the geometry are indicated. The magnitude and location of forces and/or pressures applied to the body are specified.

5) The completed mesh is exported to NASTRAN for analysis.
6) The results of the NASTRAN analysis are exported back to PATRAN for post-processing. PATRAN can be used to generate appropriate plots of the results. The .f06 file (which contains displacements, stresses, etc. for all elements and nodes in the model) can also be examined.

These steps are roughly equivalent to those delineated in the previous section. The major distinction is that the analysis steps (numbered 2 through 7) of section 6.1 are performed within the framework of NASTRAN and thus appear here as a single step (number 5).

6.3 Description of the Finite Element Model

The geometries for the smooth probe and Trivex tools were constructed directly in PATRAN. It is anticipated that the maximum deformation and/or stress will occur along the edges of the probe, since this is the area of the tool which has the most prolonged contact with the workpiece. The shank is thus considered a low-stress area, a classification which allows us to significantly reduce its height in the FEA model. The shank height for the smooth probe tools was reduced to 0.25 inches (from an initial height of 4 inches). A wireframe view of the smooth probe tool used for the FEA model is shown in Figure 69.

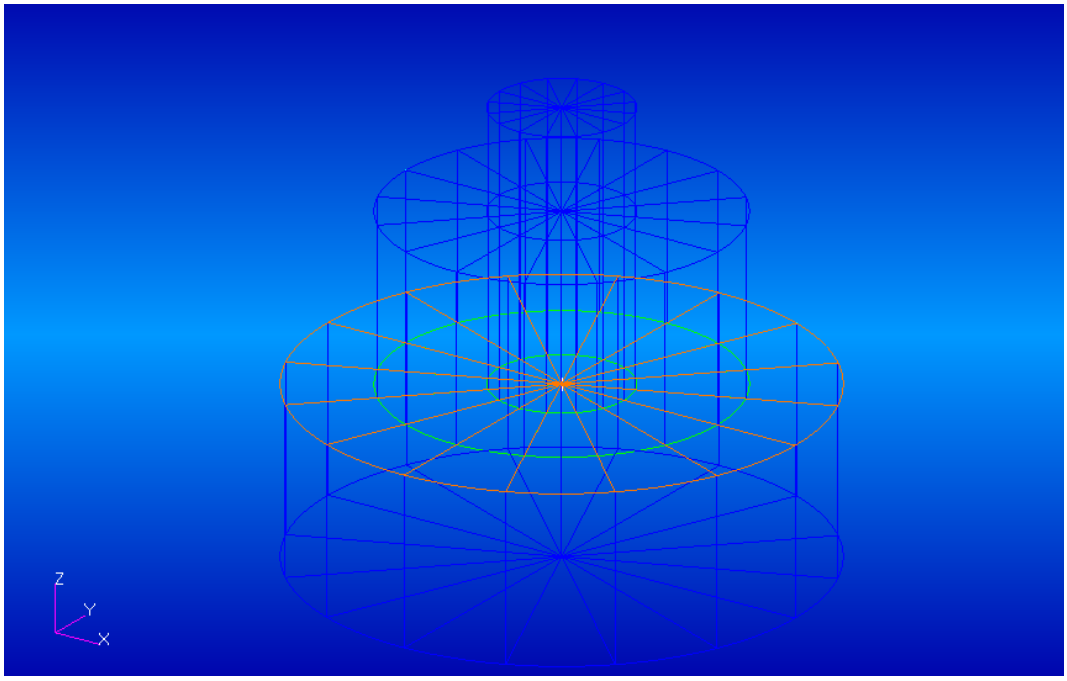

Figure 69 Wireframe view of smooth probe tool used in FEA model.

Mesh seeding was used to ensure that the mesh is more refined in the areas where stress concentration is expected to be highest (the area surrounding the probe and shoulder). Mesh seeds with five elements and one-way bias were constructed along the radial lines of the tool geometry. The paver function of PATRAN was then used to mesh the three circular surfaces (probe, shoulder, and shank) of the tool. This two-dimensional mesh of 3-noded tria elements was then extruded to form three-dimensional tria elements, identified in the .bdf file as CPENTA. Since the three dimensional mesh and the geometry of the tool were constructed independently in this case, the "Associate" feature of PATRAN was used to associate each geometric solid with its corresponding elements. Note that such an adjustment is not necessary for the simulation to run; it is merely a convenience which allows forces and boundary conditions to be applied directly to the geometry (the alternative is the often tedious selection of individual elements and nodes).

The mesh for the smooth probe model, which consists of 2144 Tria elements and 1715 nodes, appears in Figure 70. The window showing element verification can be found in Figure 71. Since no elements exceeded the threshold aspect ratio, skew, or tangential offset, remeshing is not required. If skewed elements are located in a "critical" region (i.e. an area which coincides with significant stress or deformation) it is necessary to restructure the mesh and correct for verification failures prior to running the analysis.

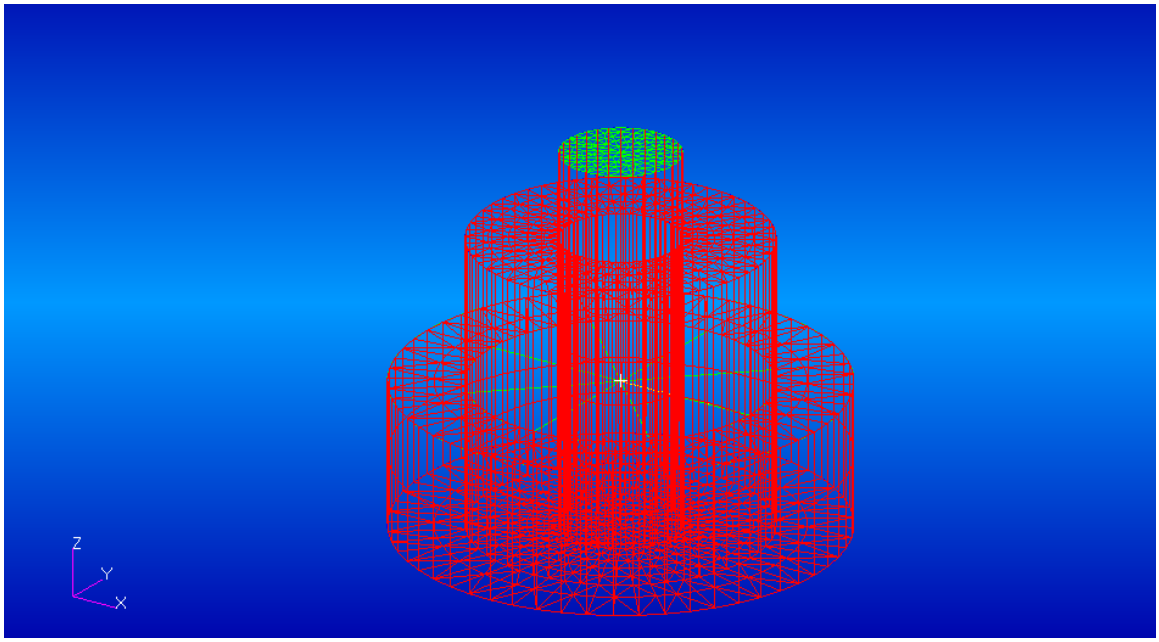

Figure 70 Mesh of smooth probe tool (2144 CPENTA elements and 1715 nodes).

The mesh for the Trivex tool was generated using the same method outlined above. A screen capture of the Trivex mesh, which is comprised of three-dimensional CPENTA elements and nodes, is shown in Figure 70. Information regarding element verification for this mesh is also included in the appendix.

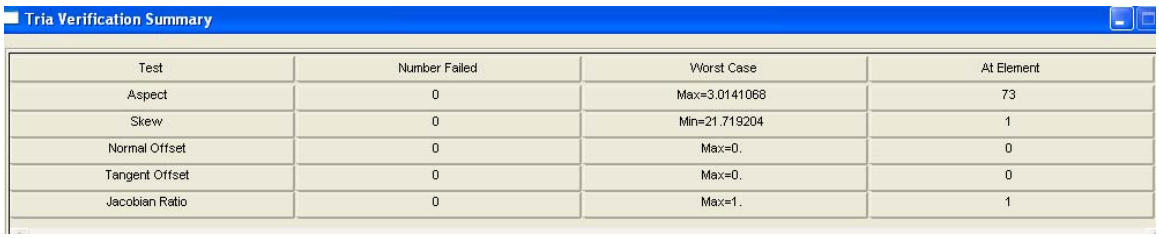

Figure 71 Element verification for mesh.

Material properties for the geometry are input directly by the user. Though additional properties may need to be specified depending on the type of analysis (i.e. thermal conductivity for thermal analyses or viscosity for situations involving fluids), structural analyses generally only require values for modulus of elasticity and Poisson's ratio. The values for the tool materials considered in this study are displayed in Table 20. Note that elastic moduli are expressed in units of pounds per square inch (psi) to ensure consistency with tool dimensions (specified in inches). The values used for CVD diamond were based on the experimental work of Klein and Cardinale [35].

Table 20 Values for material properties used in FEA simulation.

	Elastic modulus (psi)	Poisson's ratio
H13 tool steel [4]	28E+06	0.3
Molybdenum [4]	4.60E+07	0.321
CVD Diamond [35]	1.66E+08	0.0691

The smooth probe used for the "control" welds (those in which the tool was uncoated) the tools were fabricated entirely from h13 tool steel. For these tools, the entire geometry

could be assigned the properties of the base material. The prototype smooth probe tool, however, consisted of a Molybdenum substrate coated with CVD diamond. The properties associated with the diamond coating were specified for the surfaces of the probe and shoulder (the regions on which the coating was deposited). The coating was simulated using shell elements with thicknesses on the order of micrometers. The location of these shell elements corresponded to the coated region. The remainder of the geometry, including the ¼" long segment of the tool which represents the shank, was given the properties of Molybdenum.

The variability of material properties with temperature should also be considered. During the course of welding, we estimate that the tool's temperature will increase from room temperature (25 degrees Celsius) to the range of 400 to 600 C (depending on the weld parameters). In the case of steel, this increase in temperature coincides with a decrease in the modulus of elasticity (based on data from reference 4, this decrease may be upwards of fifteen percent for the temperatures previously indicated). Understandably, the variation of the modulus of CVD diamond with temperature is less well-characterized. Since the objective of this study is to merely provide "ballpark" estimates for tool deformation and stress based on force data, the effects of temperature were largely ignored in the initial analysis.

The major obstacle barring the inclusion of temperature dependency in out model is the nonuniformity of the temperature throughout the tool. The influence of geometry and weld parameters on the temperature distribution is a subject of current modeling research. Most investigations of this type use FLUENT, a computational fluid dynamics program that is better suited for thermal analysis (because NASTRAN is a structural

analysis program, temperatures usually serve as inputs). Ideally, we could use FLUENT to generate the temperature fields for a particular tool/workpiece/parameter combination and then apply the results of this analysis to the structural model in NASTRAN. In this way, the tool in the PATRAN pre-processor could be divided into geometric regions and the material properties that correspond to the temperature in each region (based on the results of the FLUENT simulation) could be specified. The caveat is that the results of such FLUENT simulations must be experimentally verified, presumably using a thermal camera or data acquired from thermocouples embedded in the workpiece. Though using the output of FLUENT simulations as an input to NASTRAN could be a more accurate way to model tool wear, it adds a level of complexity to our model that we are not yet ready to manage.

To simulate the fastening of the tool into the collet, the underside of the tool is constrained from translation and rotation in the x, y, and z directions. The tool geometry with the appropriate boundary conditions applied is shown in Figure 72 for the smooth probe. For a detailed description of which nodes the constraints were applied to, consult the .bdf file in the Appendix D.

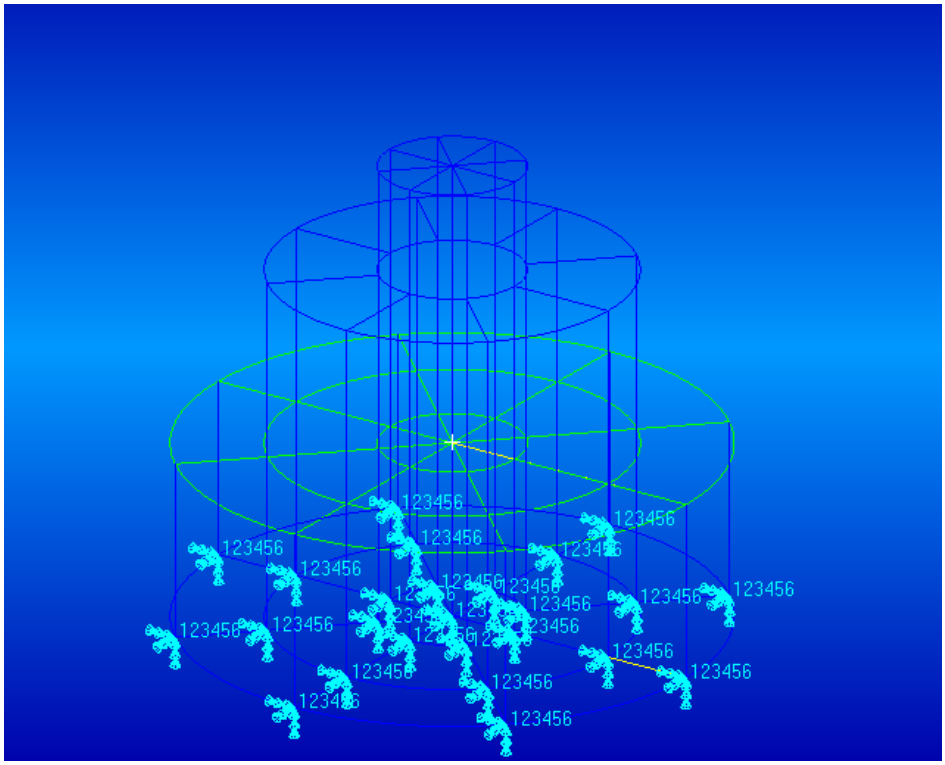

Figure 72 Boundary conditions for smooth-probe tool.

The forces on the tool during the welding process must now be accounted for. These forces are dependent upon several variables: tool geometry, workpiece material, spindle speed, traverse speed, and plunge depth, among others. Since a proven analytic method of calculating forces based on these variables does not exist in the literature, we rely upon experimental results. During a weld, forces in the x, y, and z directions are recorded by the dynamometer and plotted on a graph using Microsoft Excel software. Relative to the forces (typically on the order of hundreds or thousands of Newtons), the moment is approximately zero and thus should have little impact on the final results of the analysis. The Fx, Fy, and Fz forces vary with time: force remains static as the pin is allowed to dwell in the material to generate sufficient heat, quickly spikes up as the weld begins, and remains relatively constant for the duration of the weld. As discussed in

chapter IV, the average of the data recorded by the dynamometer during the steady-state portion of the weld was used to obtain values for the Fx, Fy, and Fz values applied to the tool.

In PATRAN, we can apply Fx, Fy, and Fz as pressures or forces to the tool surface. The advantage of a pressure application is that it results in continuous stress contours. When the forces are applied as is, the result is a stress concentration only at the points of force application; the remainder of the mesh is white (the color used by the PATRAN post processor to denote little or no stress). The application of forces instead of pressure should have no negative impact on the model's accuracy. The choice to apply pressures is largely an aesthetic one; the continuous stress contours which result from pressure application are more intuitive than the concentrated stresses produced by force application.

To apply the forces as pressures, simply divide the force data by the surface area (excluding portions of the tool which do not contact the material). The surface area calculation can thus be broken down into the surface area of the probe summed with the remaining radial area of the shoulder face. For the smooth probe tool, the surface area is equal to approximately .35 in^2. Note that forces must be converted from Newtons to pounds to remain consistent with the dimensions of the tool, which were specified in inches. Table 21 displays forces and pressures for the parameters considered for the smooth probe steel tool. Table 22 reports the same data for the smooth probe tool with diamond coating. Significantly more simulations were run for the coated tool on Al 6061 than for the uncoated tool. In the former case, it is anticipated that more simulations will

be necessary to characterize the dependence of deformation and stresses on force due to the experimental nature of the tool.

Table 21 Pressures in x, y, and z directions in pounds per square inch (psi) for uncoated tool with smooth probe at various welding parameters. The workpiece material is Al 6061.

Spindle	Travel	Px	Py	Pz
1500	16	15814.19	14321.56	78960.12
2000	16	17215.75	15505.37	83018.39
2000	20	13781.12	12317.17	95039.03
2500	16	17216.75	15608.31	58936.16
2500	25	19622.98	18966.74	89124.79
2500	25	15556.84	13884.06	83251.02
3000	16	27008.94	24319.63	74850.11

Table 22 Pressures in x, y, and z directions in pounds per square inch (psi) for coated tool with smooth probe at various welding parameters. The workpiece material is Al 6061.

Spindle	Travel	Px	Py	Pz
1500	15	14128.55	10651.19	89295
1500	15	11683.72	8497.743	75444.71
1500	15	10667.18	9348.807	79240.93
1600	10	7663.862	10198.34	85206.58
1900	10	9577.894	9537.317	62829.61
2000	15	14128.55	9851.709	80321.86
2000	16	11657.98	12237.27	56168.87
2000	20	12893.26	10689.88	85241.87
2000	20	13292.16	11566.73	77866.4
2000	20	11452.1	9890.393	70067.91
2100	10	8486.212	7654.953	67197.5
2500	15	15067.88	11785.94	73892.7
2500	16	7746.252	4667.956	54046.36
2500	25	6382.294	6060.606	35428.51
3000	15	17396.9	12585.43	68358.37
3000	16	6305.089	3687.943	47738.52
3000	30	6884.128	5854.288	33996.92
3000	30	5970.53	5802.708	35149.64
3000	30	8762.787	7672.469	32981.41

Transverse and longitudinal forces are applied to the leading edge, the portion of the tool which contacts the material first. The locations for force application are based on the research of Crawford [27], who used NASTRAN to model stresses in high speed FSW.

Figure 73 displays the model of the smooth-probe FSW tool with pressures applied in the x and y directions (values are for steel tool on Aluminum at 1500 rpm/16ipm). Figure 74 shows axial force for this parameter applied as pressures.

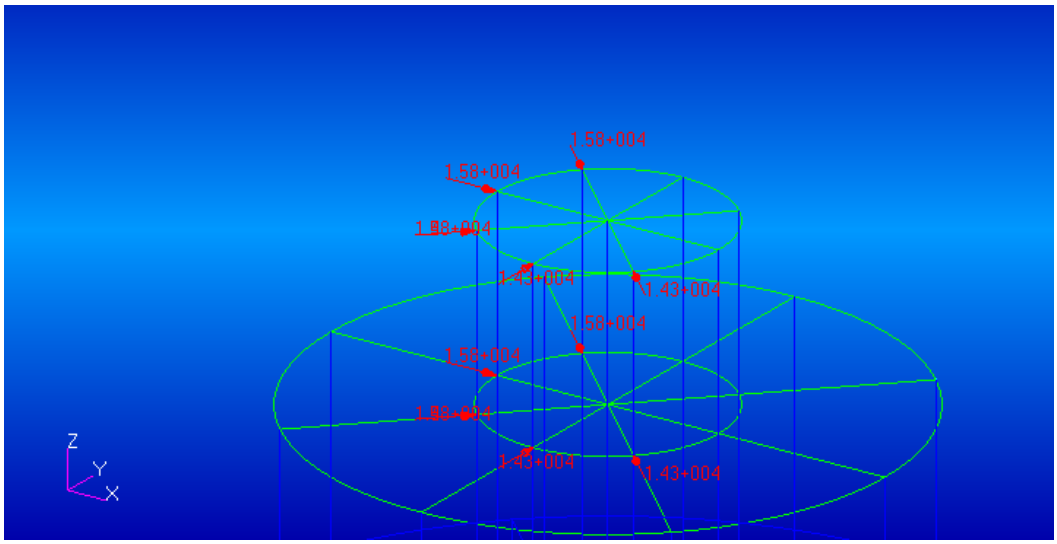

Figure 73 Smooth probe tool with pressures applied in the transverse and longitudinal directions.

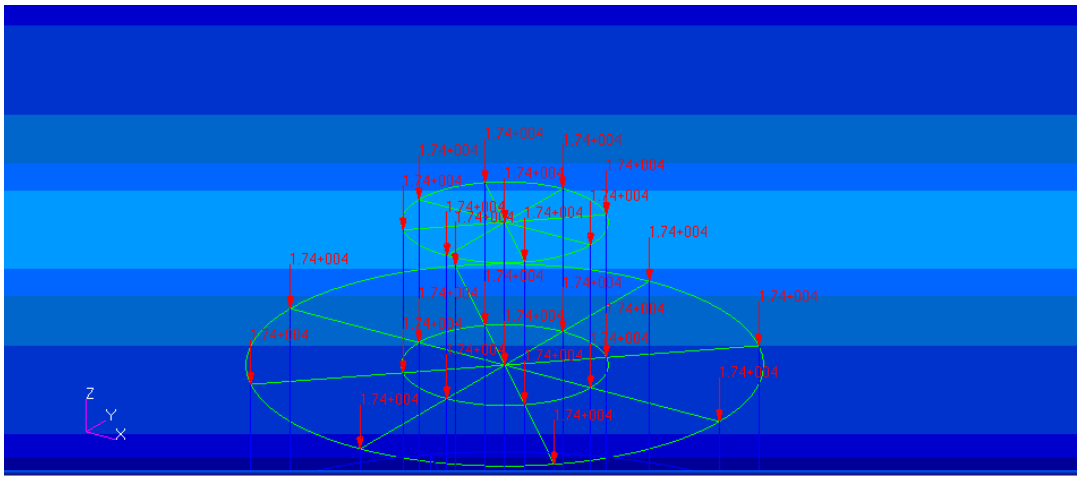

Figure 74 Smooth probe tool with axial pressures applied.

For further details on force and/or pressure placement, consult the .bdf file in the appendix D.

6.4 Results of Finite Element Analysis

Analyses were run using the pressure data in Tables 23 and 24 as inputs. For the data in Table 24, the material properties were adjusted to reflect the change in the base material to Molybdenum as well as the presence of the coating. The post-processor in PATRAN was used to generate contour plots showing tool deformation and Von Mises stress for each tool/workpiece/parameter combination considered. The deformed mesh for the uncoated steel tool with a smooth probe at 1500 rpm/16 ipm is shown in Figure 75. Figure 76 shows the Von Mises stress contour for this scenario. For the stress contour, the stresses which correspond to each color are identified by the legend on the right hand side of the plot. As we would expect, the areas of highest stress and deformation are concentrated at the probe (the black color indicates the region of maximum stress), while the lowest stress area (denoted by white) occupies most of the tool shank. Deformed meshes and stress contours for the other cases can be found in Appendix E. Note that the images in the appendix display the deformed mesh and the von Mises stress contours on the same plot. Information summarizing maximum deformation and von Mises stress appears in the left corner of the plot. The deformation and stress values for all nodes and elements can be found in the .f06 file associated with each case. These files are not included in the appendix due to length considerations; the average length of an .f06 file for this analysis is twenty pages.

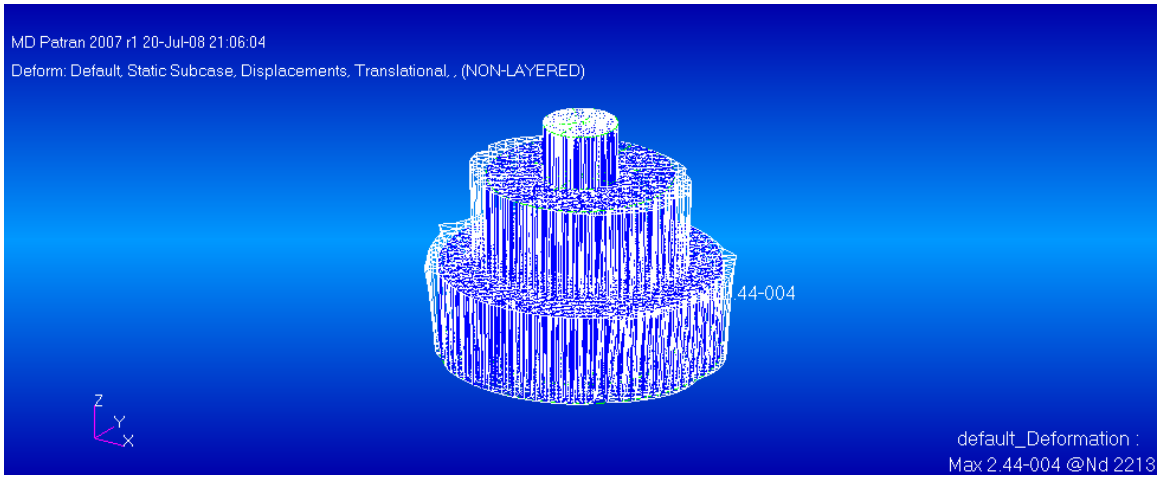

Figure 75 Tool deformation for uncoated steel tool at 1500 rpm/16ipm on Al 6061.

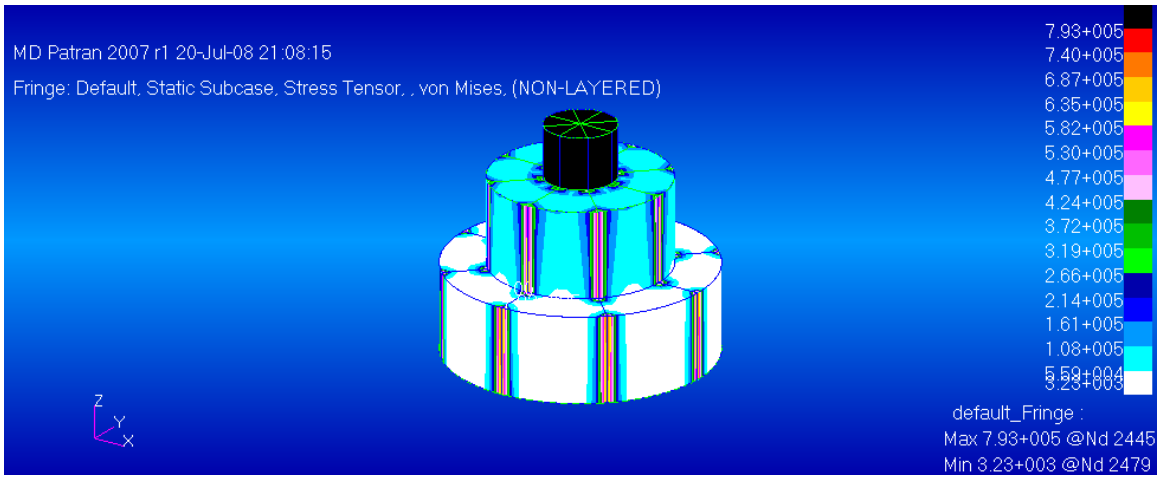

Figure 76 Von Mises stress contour for uncoated steel tool at 1500 rpm/16 ipm on Al 6061.

The values for maximum stress and deformation output by the NASTRAN simulation for the uncoated steel smooth probe are summarized in Table 23.

Table 23 Maximum stress and deformation predicted by FEA model for uncoated smooth probe steel tool on Al 6061.

Spindle	Travel	Fx	Fy	Fz	Maximum stress	Maximum deformation
1500	16	1229	1113	6136.386	7.93E+05	2.44E-04
2000	16	1337.922	1205	6451.774	8.83E+05	2.56E-04
2000	20	1071	957.2289	7385.958	9.54E+05	2.93E-04
2500	16	1338	1213	4580.224	5.92E+05	1.82E-04
2500	25	1525	1474	6926.333	8.95E+05	2.75E-04
2500	25	1209	1079	6469.853	8.36E+05	2.57E-04
3000	16	2099	1890	5816.976	7.51E+05	2.31E-04

One goal for this model is to enable us to estimate the maximum stress or deformation for a particular tool geometry and material based on dynamometer data. Based on regression analyses, we can correlate forces in the x, y, and z directions (as well as the resultant force) with stress and/or deformation. Scatterplots of maximum deformation against Fx, Fy, and Fz appear in Figures 77, 78, and 79, respectively. There does not appear to be a constitutive relationship between longitudinal or transverse forces and deformation. The function which best fits the data in Figures 77 and 78 is a third degree polynomial; however, the R^2 value in both cases is approximately .5, indicating a weak correlation between the variables. The strongest correlation exists between axial force and deformation. As Figure 79 shows, the correlation coefficient (R^2) for these variables is 1. This result is not particularly surprising; as we emphasized in the introduction, axial force is the governing factor in FSW and its applications. As discussed in chapters IV and V, the axial force data for Al 6061 displays more internal

consistency than its transverse and longitudinal counterparts. Once the weld process has reached steady-state, the axial force is essentially invariant – the same cannot be said for Fx and Fy. Thus, we can most likely attribute the lack of correlation between average x and y forces and deformation to the oscillatory behavior of the Fx and Fy values recorded by the dynamometer.

The deformation values predicted by the NASTRAN simulation are on the order of 10^{-4} inches. This is a reasonable result; tool wear is not typically observed in FSW of unreinforced Aluminum alloys, particularly when the tools in use are fabricated from sufficiently hard materials. The shorter length of the tool also minimizes deflections.. Extrapolating the trendline of Figure 79, we discern that a deformation of .001" would correspond to a force of approximately 25000 N. We also notice that decreased deformation is coincident with lower axial force. As Chapter IV and V established (as well as the work of Crawford), axial force generally decreases with increasing rotation speed [27]. By the use of transitive logic, it would thus appear that increasing axial force would be one method to combat tool wear. We will return to this statement later in the chapter.

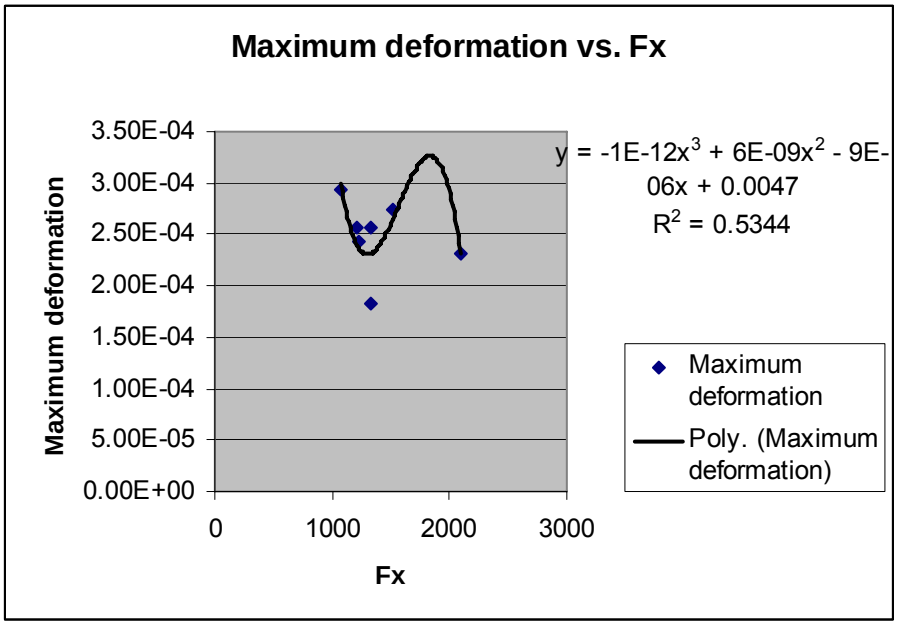

Figure 77 Maximum deformation (based on results of NASTRAN simulation) vs. Fx for uncoated steel tool with smooth probe on Al 6061.

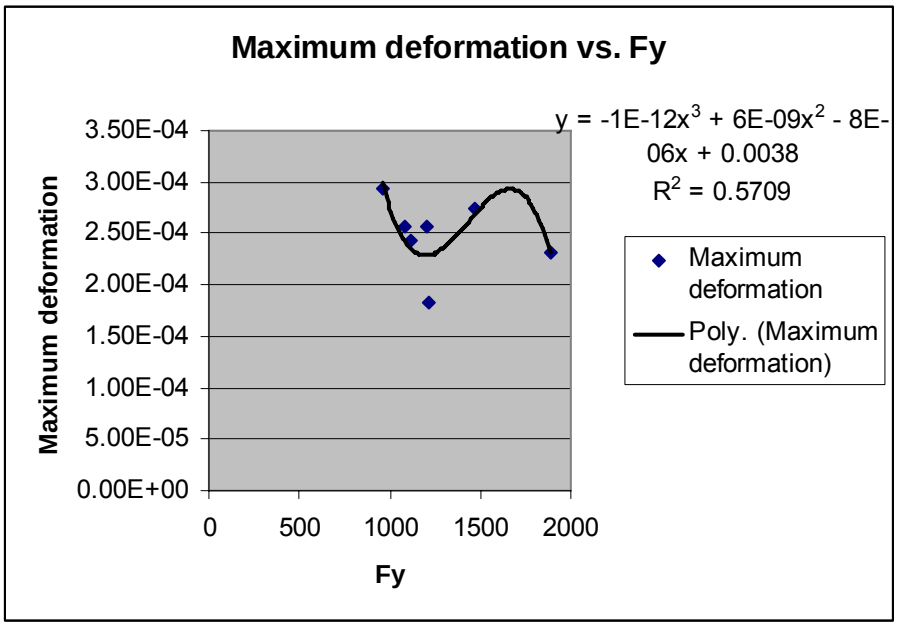

Figure 78 Maximum deformation (based on results of NASTRAN simulation) vs. Fy for uncoated steel tool with smooth probe on Al 6061.

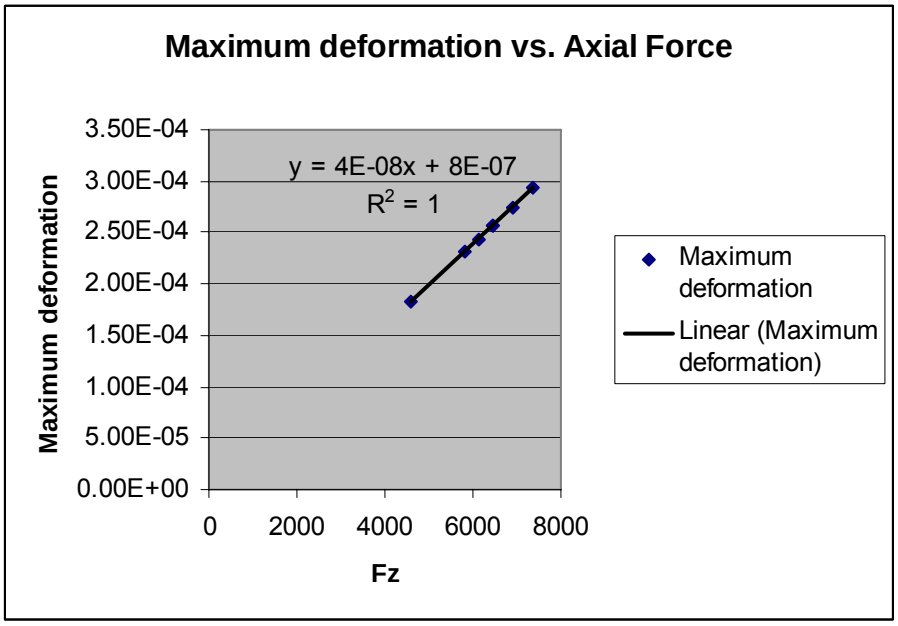

Figure 79 Maximum deformation (based on results of NASTRAN simulation) vs. Fz for uncoated steel tool with smooth probe on Al 6061.

We can similarly apply regression analysis to find correlations between Fx, Fy, Fz and maximum stress. The statistical behavior of force and stress mirrors that of force and deformation discussed above. Maximum stress and Fx and Fy are virtually uncorrelated. Axial force displays a strong linear correlation with maximum stress. Again, this would seem to imply that increasing rotation speed results in decreased stress on the tool.

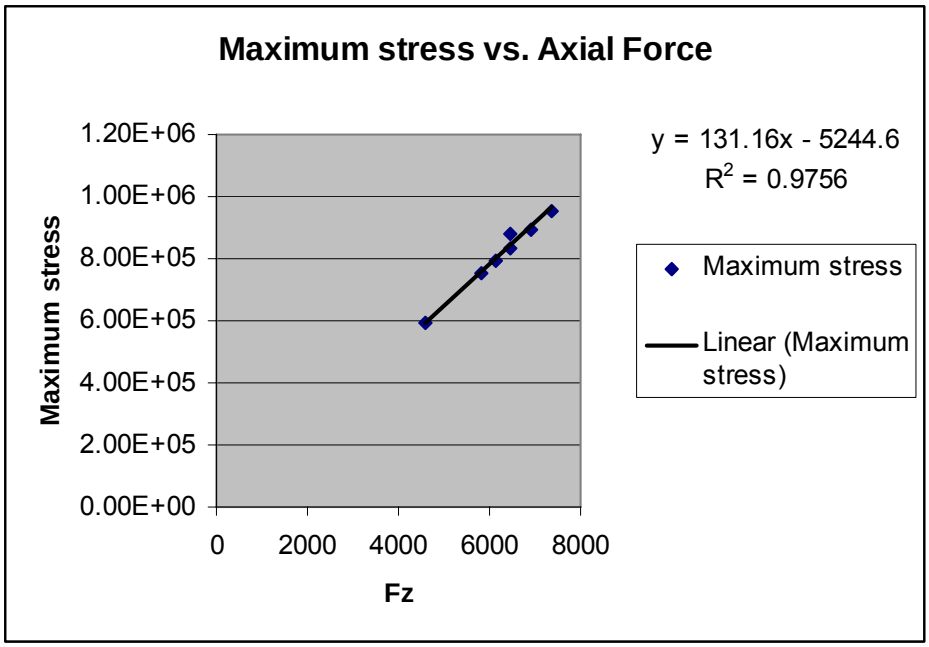

Figure 80 Maximum von Mises stress (based on results of NASTRAN simulation) vs. Fz for uncoated steel tool with smooth probe on Al 6061.

Similar analyses were run for the tool coated with diamond. The results of these simulations are tabulated in Table 24.

Table 24 Maximum stress and deformation predicted by FEA model for coated smooth probe tool on Al 6061.

Spindle	Travel	Fx	Fy	Fz	Maximum stress	Maximum deformation
1500	15	1098.00026	827.7572309	6939.560925	8.87E+05	1.95E-04
1500	15	908.0003	660.4020972	5863.185638	7.50E+05	1.65E-04
1500	15	828.999894	726.542536	6158.208875	7.87E+05	1.73E-04
1600	10	595.597035	792.5639931	6621.829365	8.47E+05	1.86E-04
1900	10	744.346032	741.1925907	4882.803141	6.24E+05	1.37E-04
2000	15	1098.00026	765.6255649	6242.21335	7.98E+05	1.75E-04
2000	16	905.999916	951.0194381	4365.163732	5.58E+05	1.23E-04
2000	20	1001.9997	830.7640242	6624.571927	8.47E+05	1.86E-04
2000	20	1033.00021	898.908422	6051.387276	7.74E+05	1.70E-04
2000	20	889.999952	768.631892	5445.327626	6.96E+05	1.53E-04
2100	10	659.505966	594.9046724	5222.253713	6.68E+05	1.47E-04
2500	15	1171.00029	915.9443271	5742.571181	7.34E+05	1.61E-04
2500	16	601.999974	362.7702005	4200.212867	5.37E+05	1.18E-04
2500	25	495.999978	470.9999953	2753.326655	3.52E+05	7.74E-05
3000	15	1352.00008	978.0766925	5312.470725	6.79E+05	1.49E-04
3000	16	489.999992	286.6084902	3709.999082	4.74E+05	1.04E-04
3000	30	535.000008	454.9659919	2642.070638	3.38E+05	7.43E-05
3000	30	463.999739	450.9574522	2731.654273	3.49E+05	7.68E-05
3000	30	680.999992	596.2659283	2563.150278	3.28E+05	7.20E-05

As in the case of the uncoated smooth probe on Aluminum, maximum deformation and forces in the x and y direction are weakly correlated at best. The same is true for maximum stress versus the longitudinal or transverse force. There model once again

indicate a perfectly linear relationship between maximum deformation and axial force, governed by the equation D = 3E-08Fz + 1E-07, where Fz is axial force in Newtons and D is deformation in inches. The rate of change of deformation with force is the slope of the trendline in Figure 81, 3E-08 in/N. Physically this means that a force increase of 1 N corresponds to an increase in maximum deformation of 3E-08 inches. According to the relationship established by this statistical correlation, a deformation of .001 inches corresponds to a force of 33330 N. This is a significantly larger force value than that for the uncoated tool at .001 inch deformation (approximately 25000 N). Though perhaps an obvious result, the FEA model indicates that it requires more force to deform the coated tool. A graphical comparison of maximum tool deformation as a function of axial force for the coated and uncoated tool appears in Figure 82.

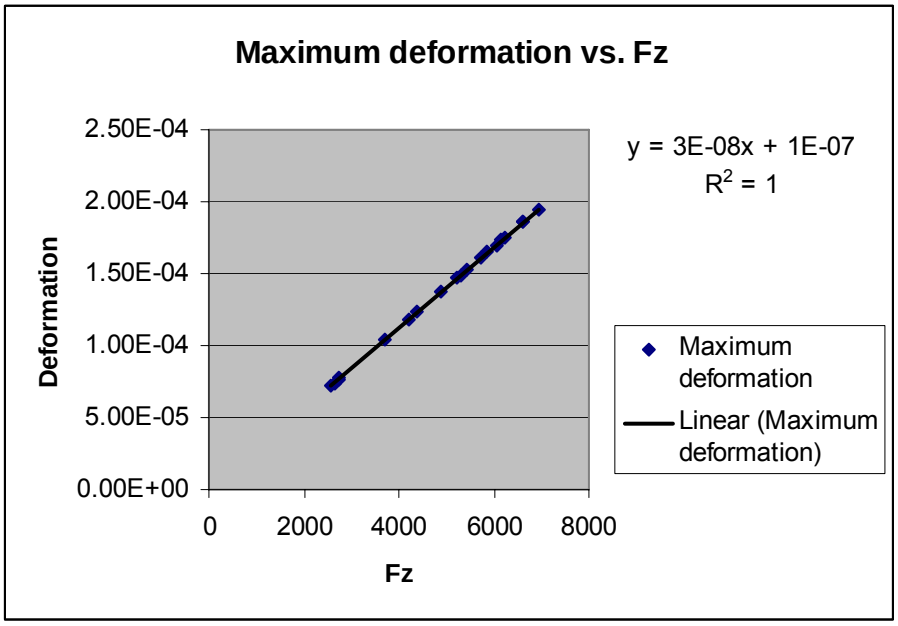

Figure 81 Maximum deformation as a function of axial force for the coated tool (based on FEA simulations).

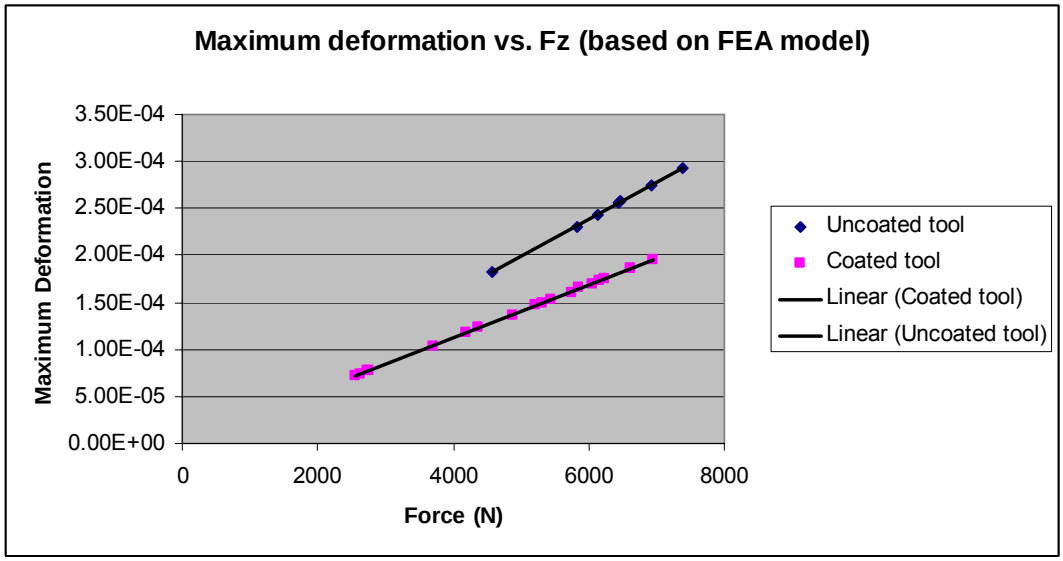

Figure 82 Comparison of maximum deformation results for coated and uncoated tool based on FEA simulation.

Maximum stress as a function of axial force for the coated tool is plotted in Figure 83. Again, the Fx and Fy forces are virtually uncorrelated with axial force. The result of the comparison of the maximum stress functions for the coated and uncoated tool parallels the conclusions drawn about deformation. The reduced axial force on the coated tool translates into slightly smaller maximum stress values. Since lower forces typically coincide with faster rotation speeds, this result implies that stress can be even further reduced by increasing the spindle speed of the coated tool.

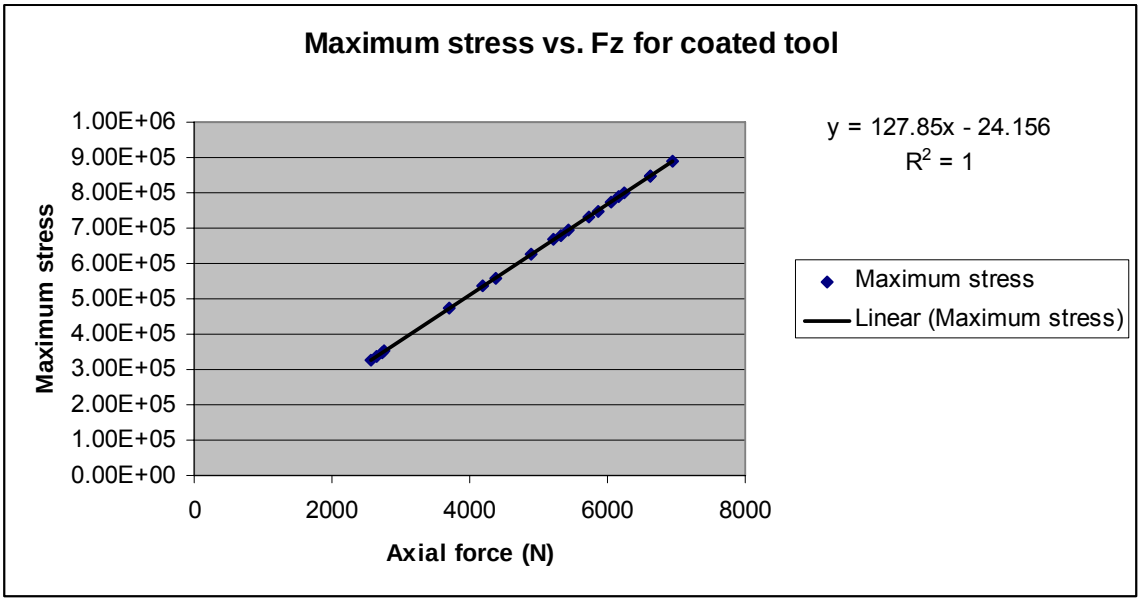

Figure 83 Maximum stress as a function of axial force for the coated tool.

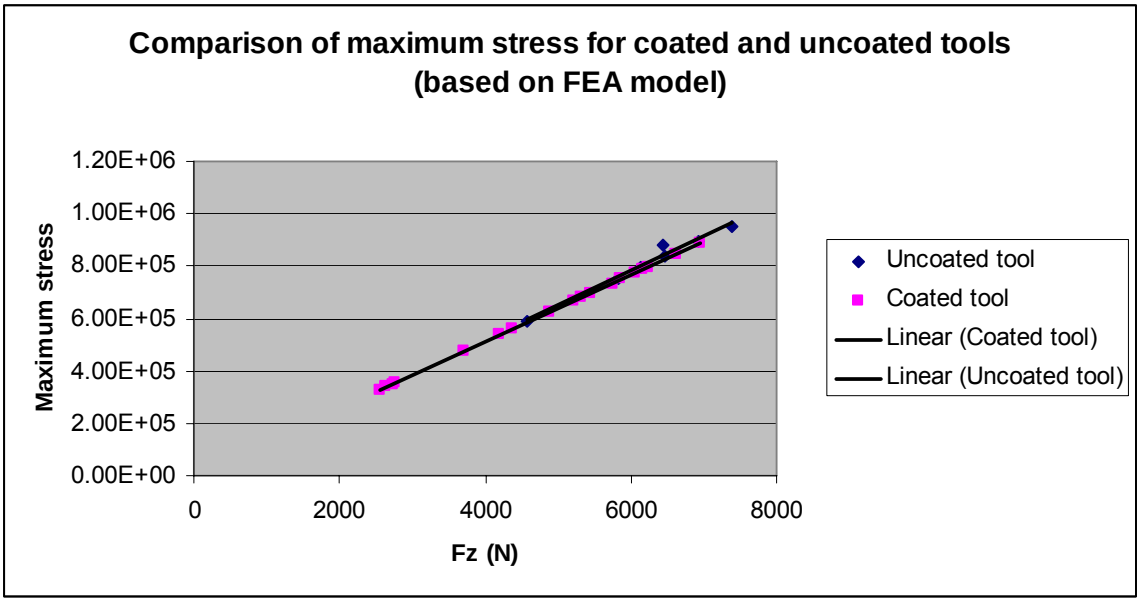

Figure 84 Comparison of maximum stress for coated and uncoated tools based on FEA simulation.

Based on the results of the model, it appears that the diamond coating has the potential to significantly reduce tool deformation. Because the wear for either tool in the welding of unreinforced materials such as Aluminum 6061 is negligible, it is not possible for us to correlate tool wear with the maximum deformation predicted by the model. Though deformation is not necessarily synonymous with wear, it is reasonable to suggest that decreased deformation of the coated tool (as compared to values for the uncoated tool), particularly in the probe region, suggests that the diamond coating may aid in wear resistance.

6.5 Preliminary assessment of thermal effects

We now return to the variation of material properties with temperature. The most rigorous and accurate characterization of thermal effects would perhaps be obtained through the method suggested in the previous section, in which temperature fields output

by FLUENT are used to determine the input of material properties in PATRAN. However, a simpler protocol to analyze the effects of temperature variation on the deformation and maximum stress for the coated and uncoated tool can be implemented in PATRAN using the structure of the existing model. As discussed earlier in the chapter, the modulus of elasticity for a particular material can decrease substantially with increasing temperature. We would expect that such a decrease in elastic modulus would result in increased deformation and maximum stress. In this sense, the results for the smooth probe models presented previously may be underestimations. We can quantify the model's tendency to underpredict by re-running the analyses with the material moduli adjusted to correspond with a typical welding temperature for FSW (for instance, 400 ^{o}C). The variability of the modulus of h13 tool steel was determined using data from reference 4. At 427 ^{o}C, the elastic modulus of tool steel is reduced by approximately twenty percent. The simulations of Figure 23 were run again with this reduced modulus for steel as a material property input. The image of the deformed mesh and stress contours for these simulations appear in the appendix. The function which governs maximum deformation for the high temperature case is plotted in Figure 85. The trendline which was the result of the analysis run using the value for the elastic modulus at room temperature also appears for comparison. The graph makes it apparent that a percent reduction in the modulus to reflect temperature changes translates into an equivalent percent increase in deformation. The slope of the trendline for the data with a modulus at 400 degrees Celsius is also steeper (5E-08 in/N) than that for the modulus at room temperature (3E-08 in/N). Physically, this indicates that for the same amount of force increase, the model which uses the modulus at 400 C as an input will experience a

greater increase in deformation. The results of this simple analysis indicate that the consideration of temperature effects is critical to the exactness of the FEA analysis. Though the major part of an FEA simulation is invested in the construction of a sufficiently refined mesh and the proper application of loads and boundary conditions, materials characterization is just as vital. The variation of the properties of steel with temperature is well understood; more exotic materials, however, may not be characterized with the same degree of accuracy.

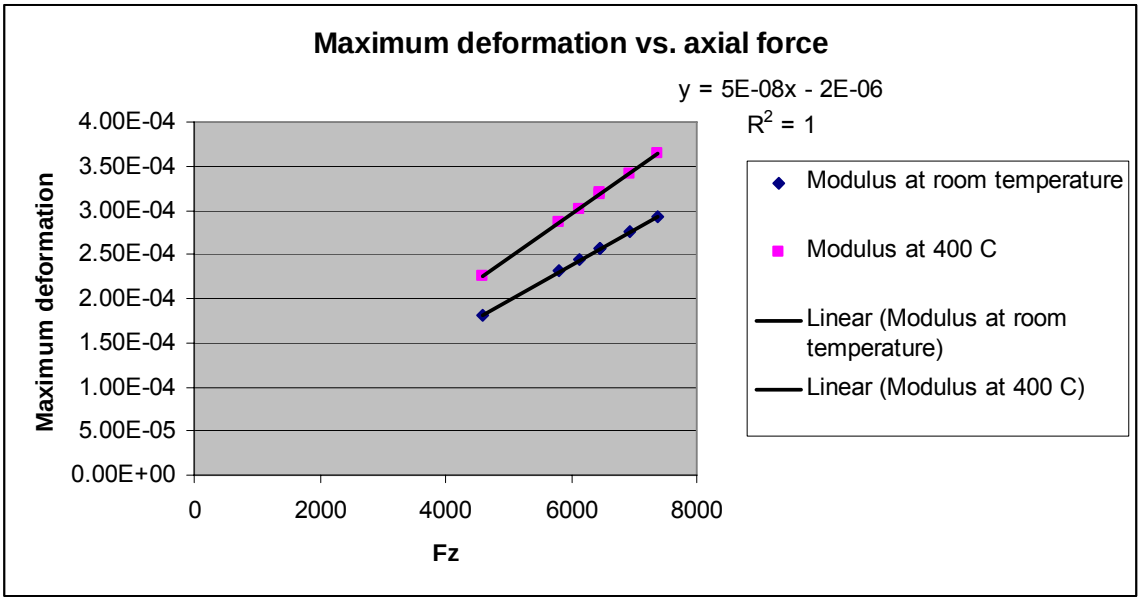

Figure 85 Comparison of maximum deformation for simulations with room temperature modulus and modulus at 400 ^{o}C.

6.6 Conclusions and Recommendations

The major weakness in the Finite Element analysis discussed above is that we have attempted to model a dynamic process through the application of static forces. Though this can give us a welding "snapshot" of the tool deformation and stress for given parameters, it requires experimental data for force input. Since any FSW process is

essentially a fluid flow problem, FLUENT would probably be a better software package for this type of analysis. There is also some question concerning where the forces are applied. The author chose to apply them at the tool's leading edge, but it would also be reasonable to apply then to all nodes at the surface of the pin and shoulder, rather than just a few selected at regular intervals. Additionally, any results produced by this model need to be verified by experimental or analytic methods. At the time of this writing, there does not exist a "catch-all" analytical expression for the FSW process, primarily because it is dependent upon so many variables. If an analytical model is found and used for verification, we must ensure that the tool geometry, tool material, and workpiece material are the same as that described in the FEA model. Due to the lack of verification, this model is only recommended as a means to obtain "ballpark" values for tool deformation and stress for the workpiece/tool material combinations considered above.

APPENDIX A

FORCE PLOTS FOR UNCOATED TOOL

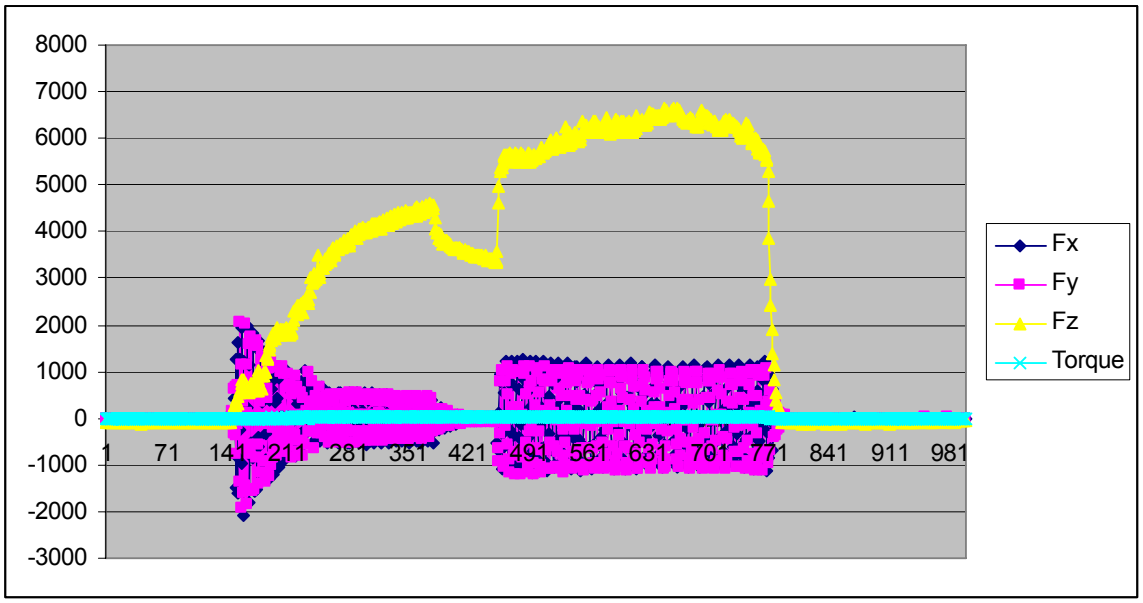

1500 rpm, 16 ipm

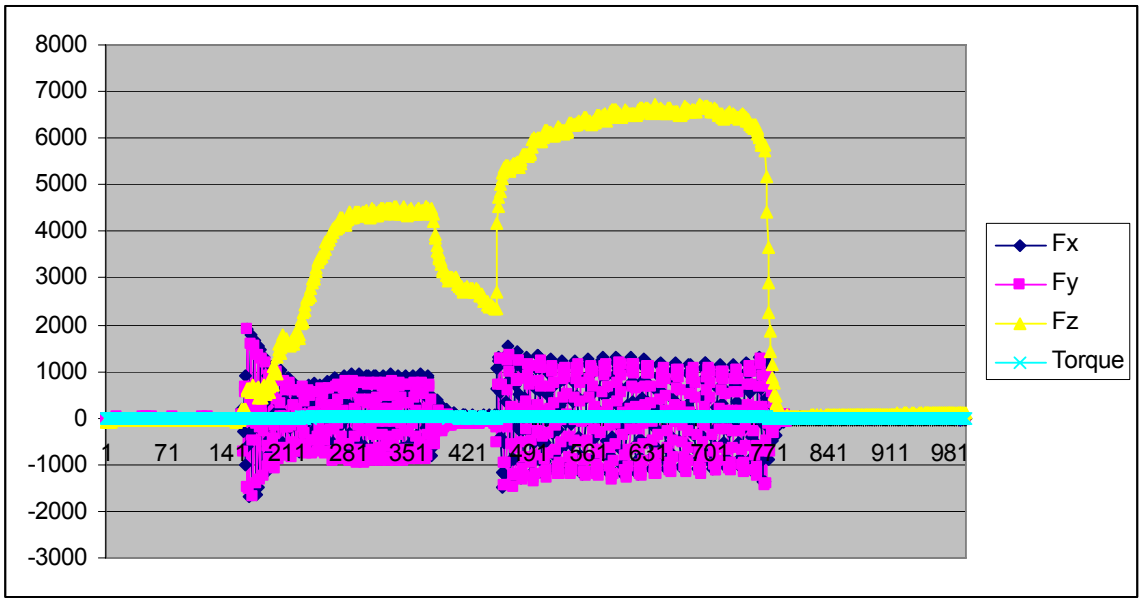

2000 rpm, 16 ipm

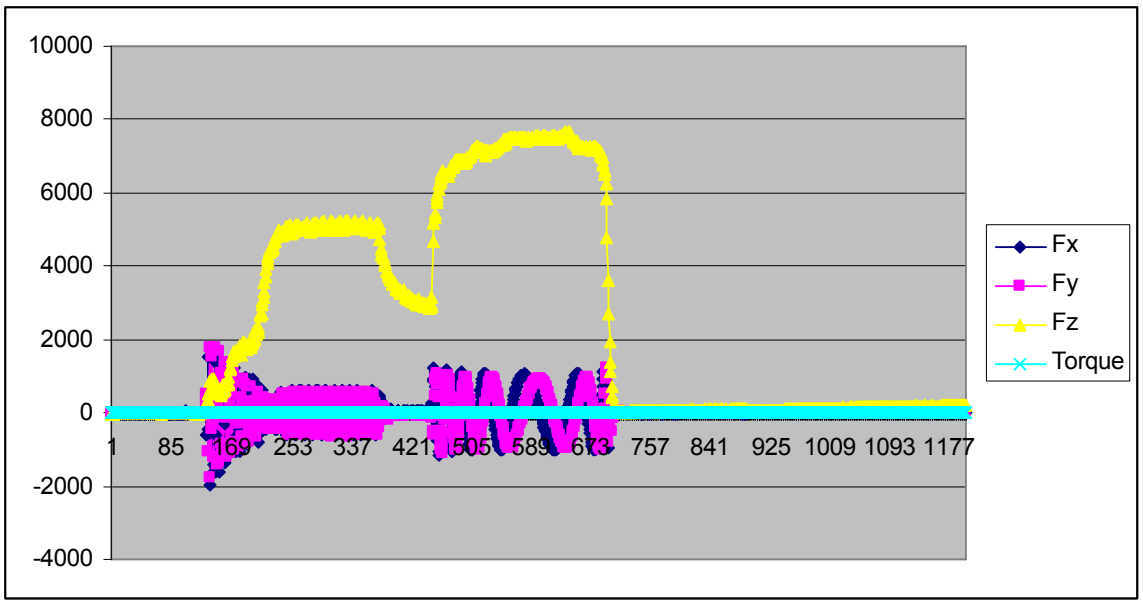

2000 rpm, 20 ipm

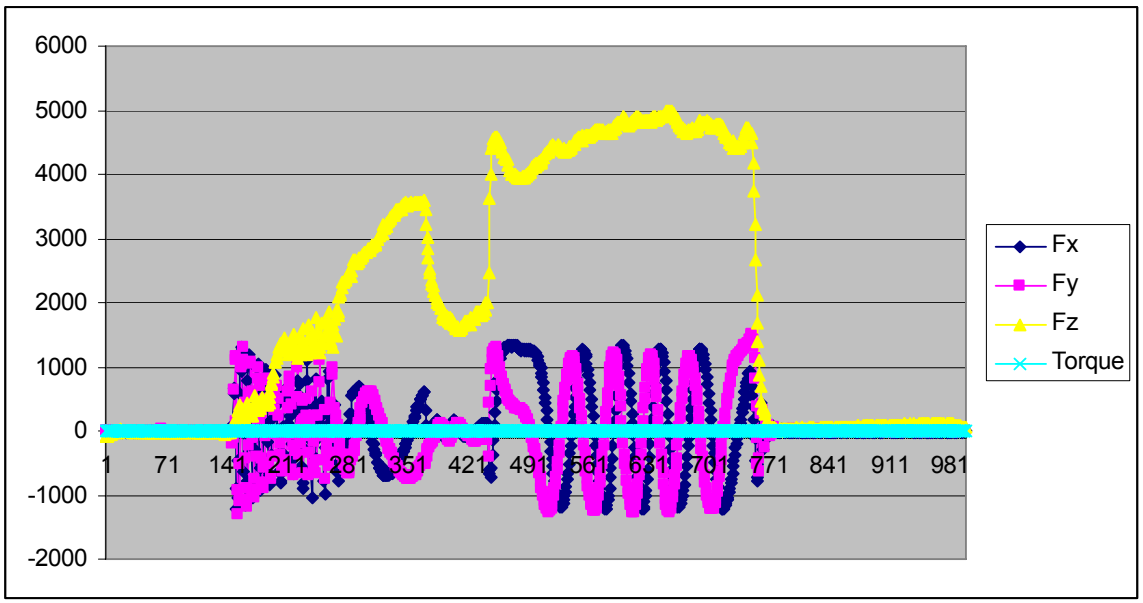

2500 rpm, 16 ipm

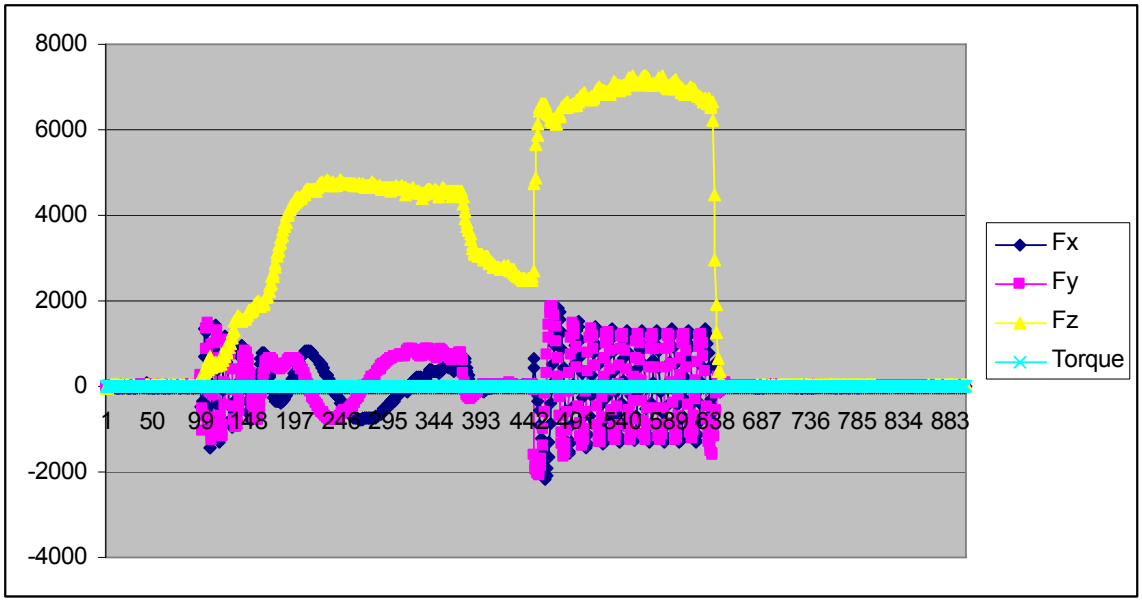

2500 rpm, 25 ipm

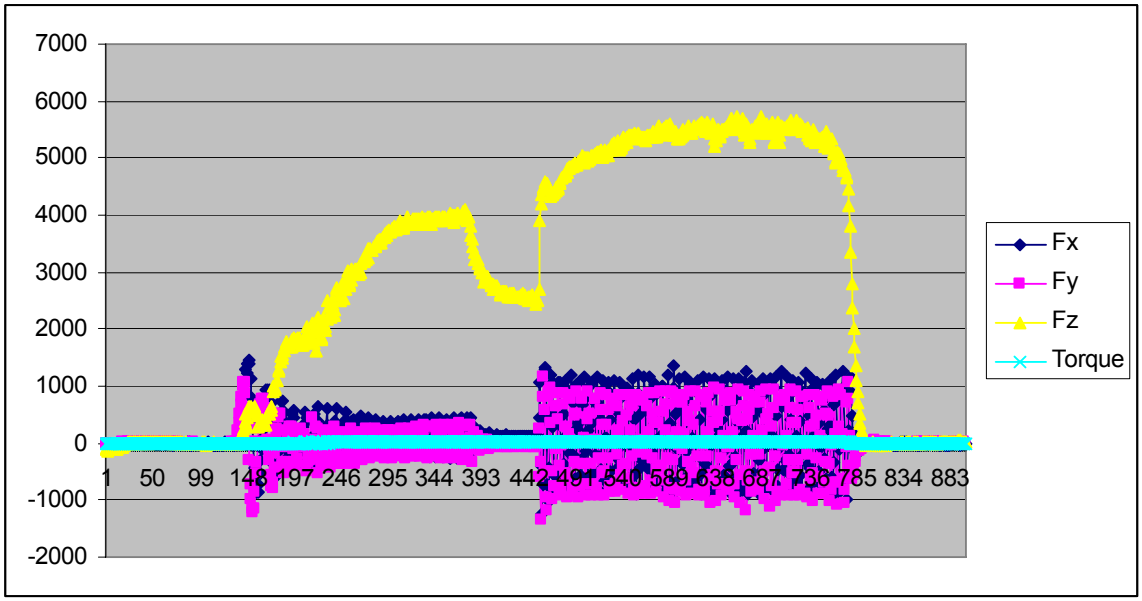

3000 rpm, 16 ipm

APPENDIX B

FORCE PLOTS FOR COATED TOOLS

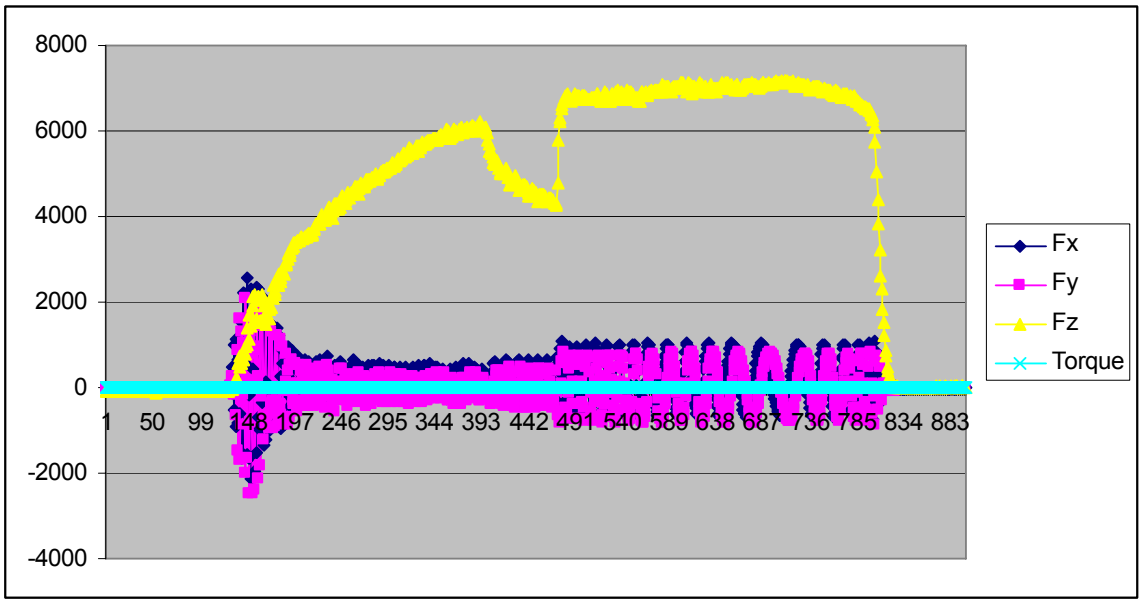

1500 rpm, 16 ipm

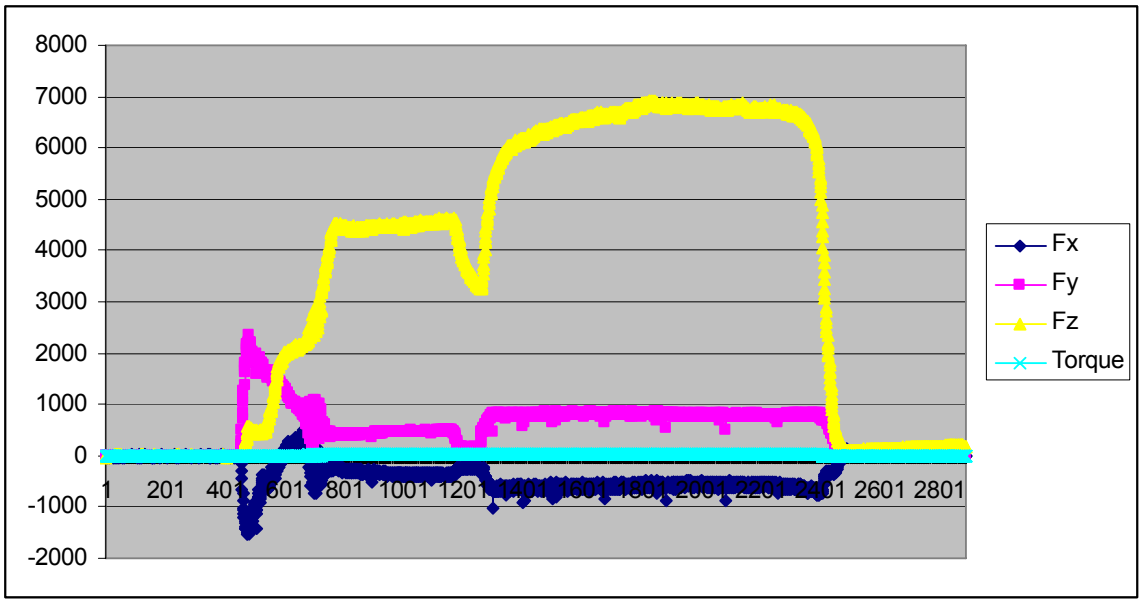

1600 rpm, 10 ipm

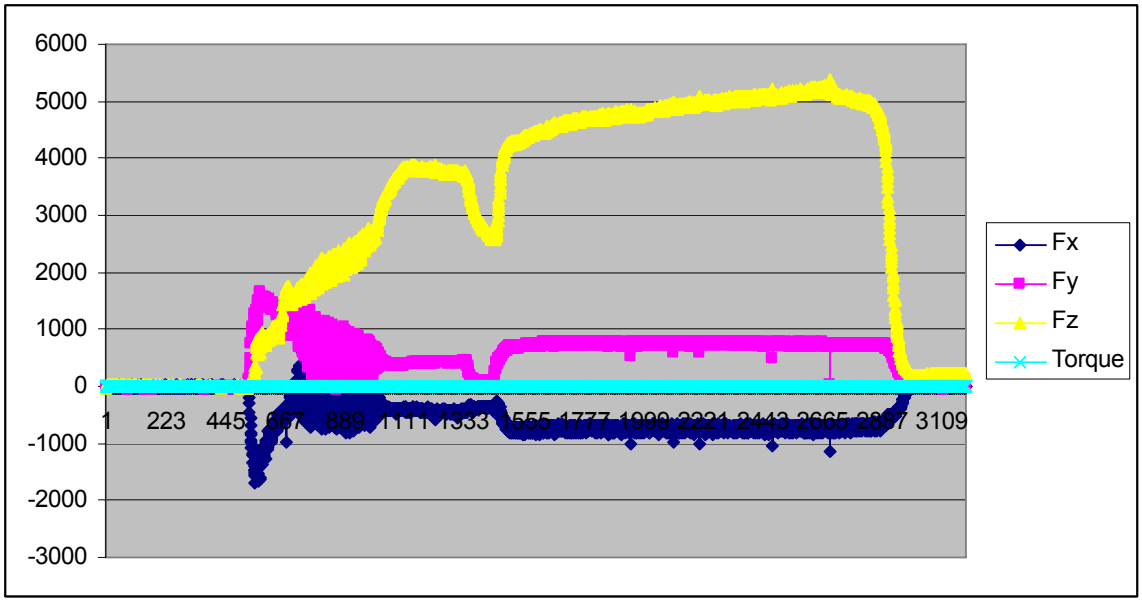

1900 rpm, 10 ipm

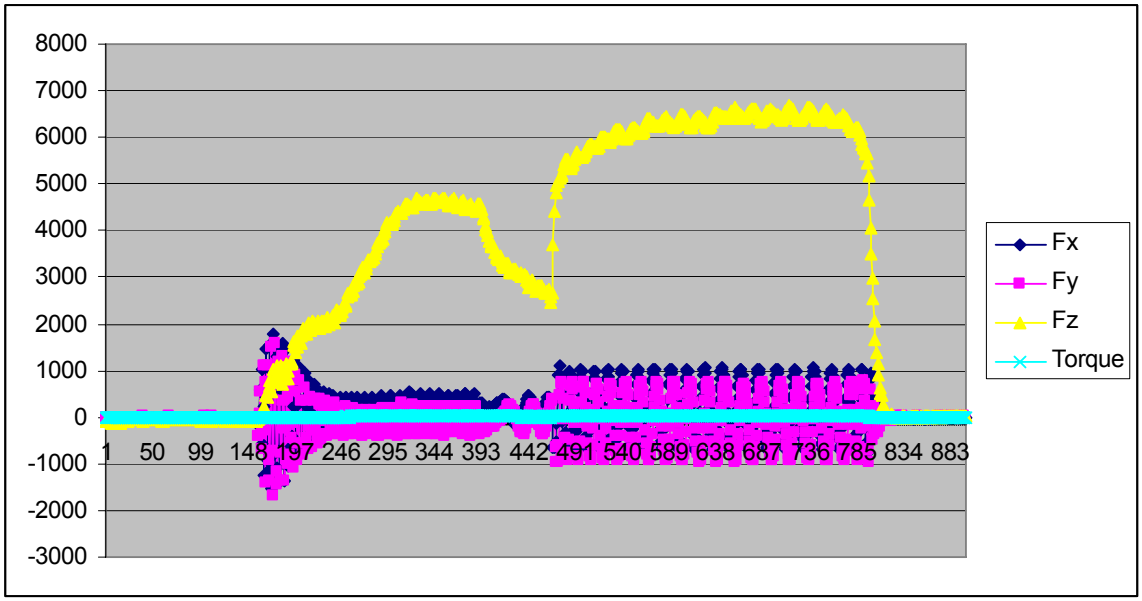

2000 rpm, 16 ipm

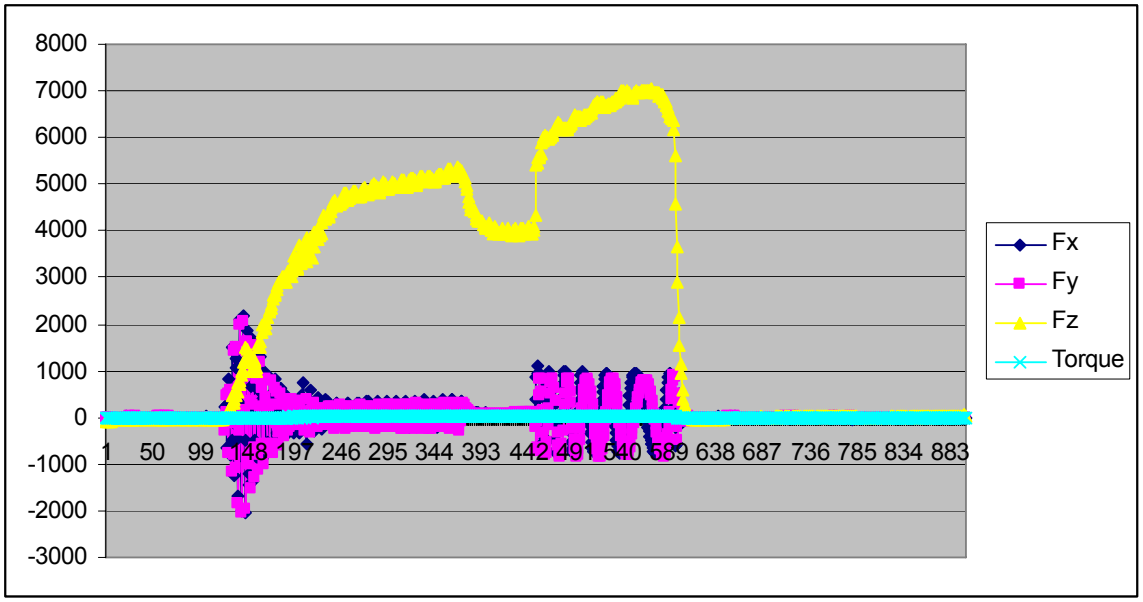

2000 rpm, 20 ipm

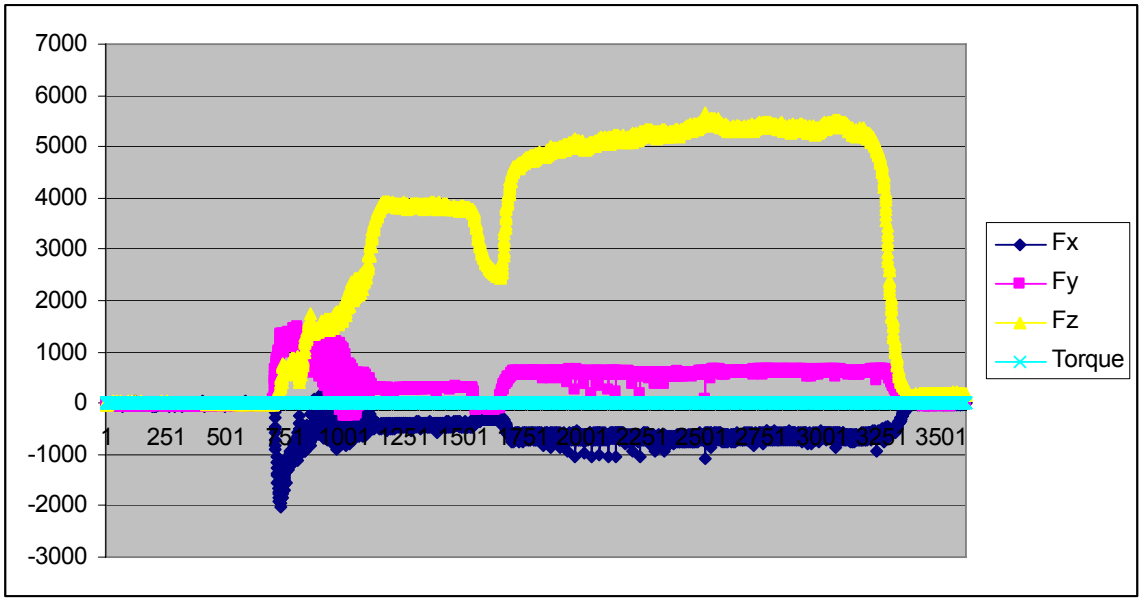

2100 rpm, 10 ipm

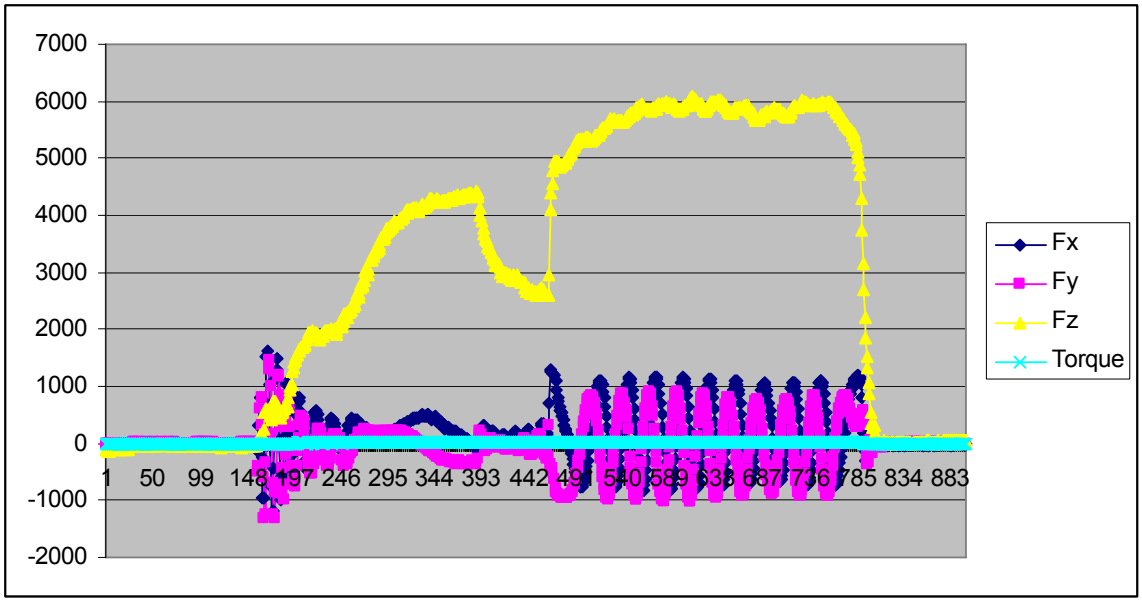

2500 rpm, 16 ipm

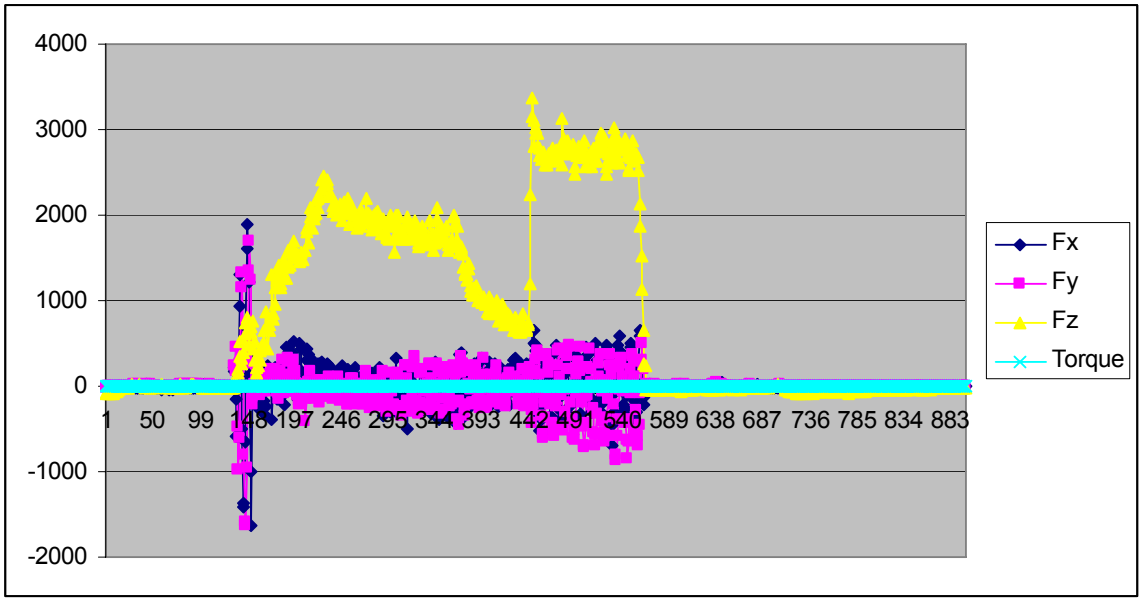

2500 rpm, 25 ipm

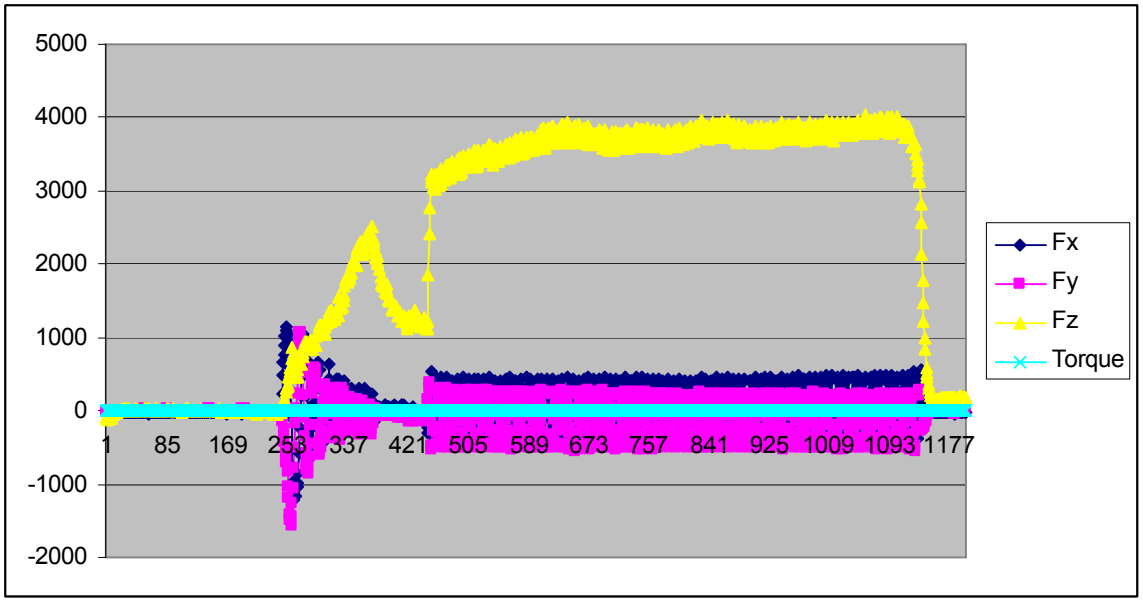

3000 rpm, 16 ipm

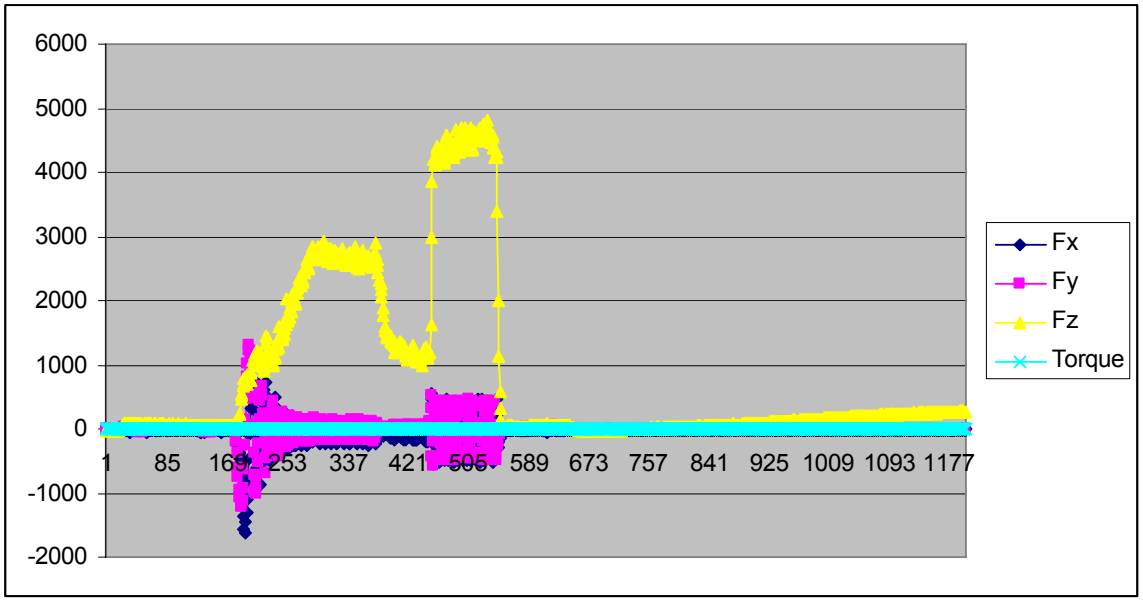

3000 rpm, 30 ipm

APPENDIX C

SURFACE IMAGES OF WELDS ON AL 6061 USING TRIVEX TOOL

1000 rpm, 3 ipm

1000 rpm, 5 ipm

1000 rpm, 7 ipm

1000 rpm, 9 ipm

1000 rpm, 11 ipm

1500 rpm, 5 ipm

1500 rpm, 7 ipm

1500 rpm, 9 ipm

1500 rpm, 11 ipm

1500 rpm, 13 ipm

2000 rpm, 7 ipm

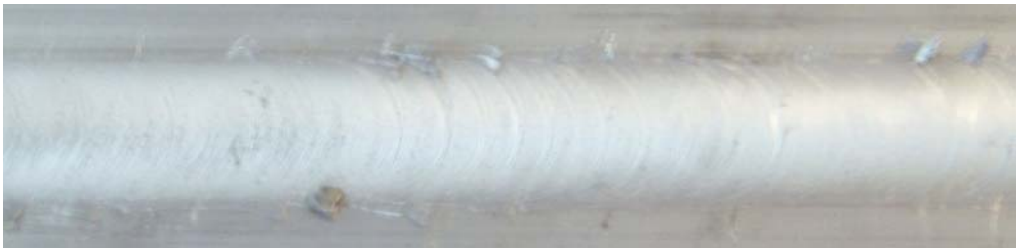

2000 rpm, 9 ipm

2000 rpm, 11 ipm

2000 rpm, 13 ipm

2100 rpm, 9 ipm

2100 rpm, 11 ipm

2100 rpm, 13 ipm

APPENDIX D

BDF FILE FOR FINITE ELEMENT MODEL

```
$ NASTRAN input file created by the MSC MSC.Nastran input file
$ translator ( MD Patran 15.0.022 ) on July      21, 2008 at 15:02:02.
$ Direct Text Input for Nastran System Cell Section
$ Direct Text Input for File Management Section
$ Linear Static Analysis, Database
SOL 101
$ Direct Text Input for Executive Control
CEND
TITLE = MD Nastran job created on 21-Jul-08 at 11:29:29
ECHO = NONE
$ Direct Text Input for Global Case Control Data
SUBCASE 1
$ Subcase name : Default
   SUBTITLE=Default
   SPC = 2
   LOAD = 2
   DISPLACEMENT(SORT1,REAL)=ALL
   SPCFORCES(SORT1,REAL)=ALL
   STRESS(SORT1,REAL,VONMISES,BILIN)=ALL
BEGIN BULK
PARAM    POST    -1
PARAM   PRTMAXIM YES
$ Direct Text Input for Bulk Data
$ Elements and Element Properties for region : moly
PSOLID   1       1       0
$ Pset: "moly" will be imported as: "psolid.1"
CPENTA   265     1       209     211     210     417     419     418
CPENTA   266     1       210     213     212     418     421     420
CPENTA   267     1       212     215     214     420     423     422
CPENTA   268     1       214     217     216     422     425     424
CPENTA   269     1       218     219     216     426     427     424
CPENTA   270     1       218     217     220     426     425     428
CPENTA   271     1       220     222     221     428     430     429
CPENTA   272     1       221     224     223     429     432     431
CPENTA   273     1       223     226     225     431     434     433
CPENTA   274     1       225     228     227     433     436     435
CPENTA   275     1       229     230     227     437     438     435
CPENTA   276     1       229     228     231     437     436     439
CPENTA   277     1       231     233     232     439     441     440
CPENTA   278     1       213     215     212     421     423     420
CPENTA   279     1       232     233     213     440     441     421
CPENTA   280     1       232     213     211     440     421     419
CPENTA   281     1       210     211     213     418     419     421
CPENTA   282     1       220     217     222     428     425     430
CPENTA   283     1       224     221     222     432     429     430
CPENTA   284     1       226     223     224     434     431     432
CPENTA   285     1       228     225     226     436     433     434
CPENTA   286     1       229     227     228     437     435     436
CPENTA   287     1       218     216     217     426     424     425
CPENTA   288     1       214     215     217     422     423     425
CPENTA   289     1       231     228     233     439     436     441
CPENTA   290     1       217     215     234     425     423     442
```

```
CPENTA   291     1       222     217     234     430     425     442
CPENTA   292     1       224     222     234     432     430     442
CPENTA   293     1       234     226     224     442     434     432
CPENTA   294     1       215     233     234     423     441     442
CPENTA   295     1       233     215     213     441     423     421
```

```
.$ Material Record : Molybdenum
$ Description of Material : Date: 21-Jul-08           Time: 11:17:29
MAT1     1      4.6+7           .321
$ Nodes of the Entire Model
GRID*    1                                -1.42376-11     -1.42376-11
*       .65
GRID*    2                                -.0999998       -8.74226-9
*       .65
GRID*    3                                -.0168076       -2.10701-5
*       .65
GRID*    4                                -.0373938       -3.26907-9
*       .65
GRID*    5                                -.062606        -5.47319-9
*       .65
GRID*    6                                -.0831916       -7.27284-9
*       .65
GRID     7              -.070710-.070710.65
GRID     8              -.099369-.011210.65
GRID     9              -.097486-.022279.65
GRID     10             -.094374-.033067.65
GRID     11             -.090074-.043435.65
GRID     12             -.084653-.053232.65
GRID     13             -.078172-.062362.65
GRID     14             -.058825-.058825.65
GRID     15             -.044269-.044269.65
GRID     16             -.026441-.026441.65
GRID     17             -.011885-.011885.65
GRID     18             -.032595-.013220.65
GRID     19             -.054834-.014288.65
GRID     20             -.079248-.014155.65
GRID     21             -.086813-.026108.65
GRID     22             -.085559-.034487.65
GRID     23             -.077077-.040358.65
GRID     24             -.072567-.028396.65
```

```
$ Loads for Load Case : Default
SPCADD   2       1
LOAD     2      1.      1.       1
$ Displacement Constraints of Load Set : fixed
SPC1     1       123456  625     635     646     661     687     713
         739     765     791     1457    1481    1520    1559    1598
         1613    1637    1676    1770    1774    1826    1878    1930
         1982    2034    2086
$ Pressure Loads of Load Set : px
$ Pressure Loads of Load Set : py
$ Pressure Loads of Load Set : pz
PLOAD4   1       793     7732.92                         845
PLOAD4   1       794     7732.92                         864
PLOAD4   1       795     7732.92                         853
PLOAD4   1       796     7732.92                         854
```

```
PLOAD4   1       797    7732.92                          855
PLOAD4   1       798    7732.92                          855
PLOAD4   1       799    7732.92                          870
PLOAD4   1       800    7732.92                          857
PLOAD4   1       801    7732.92                          857
PLOAD4   1       802    7732.92                          858
PLOAD4   1       803    7732.92                          859
PLOAD4   1       804    7732.92                          860
PLOAD4   1       805    7732.92                          834
PLOAD4   1       806    7732.92                          860
PLOAD4   1       807    7732.92                          861
PLOAD4   1       808    7732.92                          862
PLOAD4   1       809    7732.92                          863
PLOAD4   1       810    7732.92                          864
PLOAD4   1       811    7732.92                          864
PLOAD4   1       812    7732.92                          848
PLOAD4   1       813    7732.92                          849
PLOAD4   1       814    7732.92                          850
PLOAD4   1       815    7732.92                          851
PLOAD4   1       816    7732.92                          852
PLOAD4   1       817    7732.92                          835
PLOAD4   1       818    7732.92                          836
PLOAD4   1       819    7732.92                          837
PLOAD4   1       820    7732.92                          838
PLOAD4   1       821    7732.92                          860
PLOAD4   1       822    7732.92                          842
PLOAD4   1       823    7732.92                          843
PLOAD4   1       824    7732.92                          844
PLOAD4   1       825    7732.92                          856
PLOAD4   1       826    7732.92                          867
PLOAD4   1       827    7732.92                          863
PLOAD4   1       828    7732.92                          865
PLOAD4   1       829    7732.92                          869
PLOAD4   1       830    7732.92                          867
PLOAD4   1       831    7732.92                          869
PLOAD4   1       832    7732.92                          869
PLOAD4   1       833    7732.92                          859
PLOAD4   1       834    7732.92                          866
PLOAD4   1       835    7732.92                          860
PLOAD4   1       836    7732.92                          865
PLOAD4   1       837    7732.92                          861
```

APPENDIX E

CONTOUR PLOTS FOR FINITE ELEMENT ANALYSIS

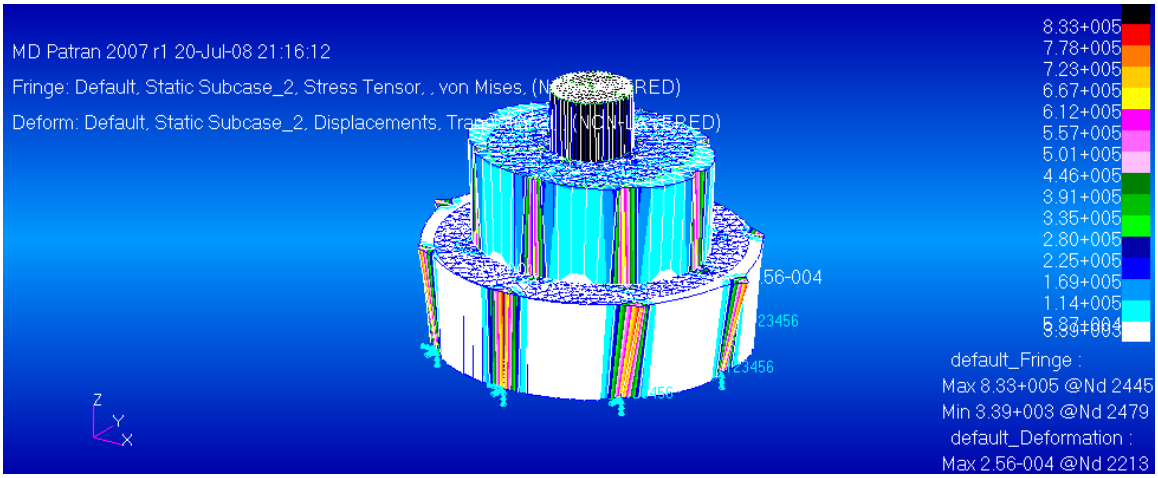

2000 rpm, 16 ipm (uncoated)

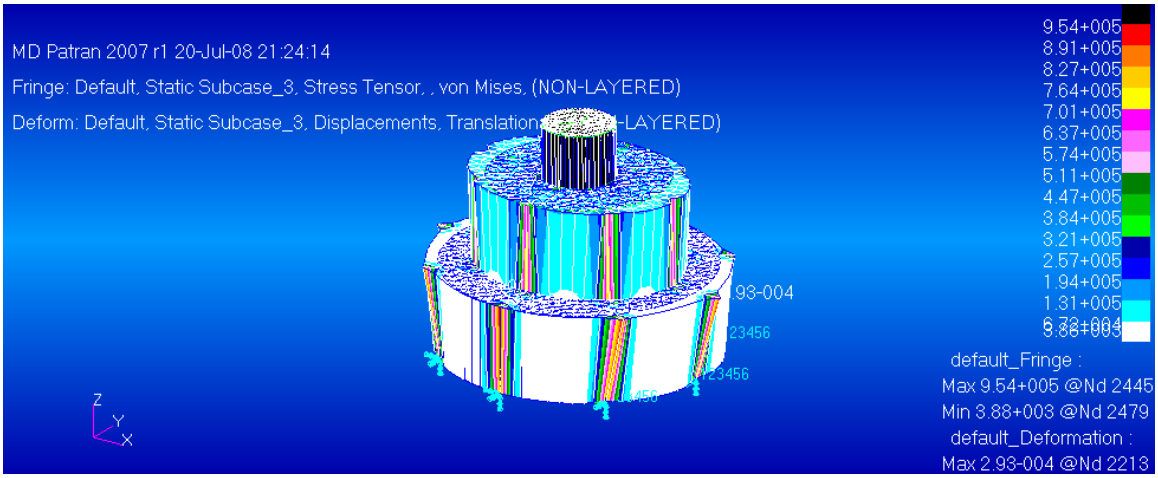

2000 rpm, 20 ipm (uncoated)

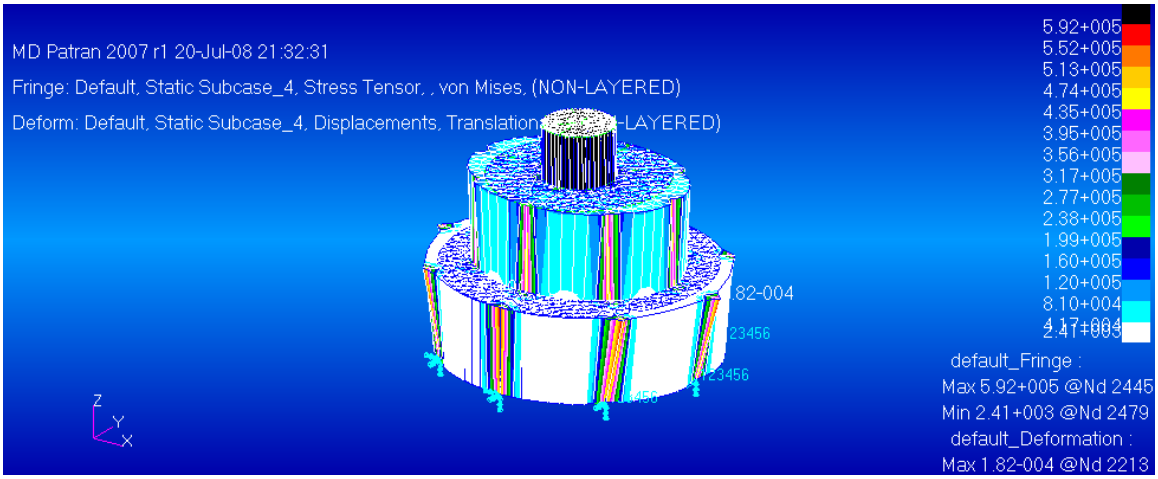

2500 rpm, 16 ipm (uncoated)

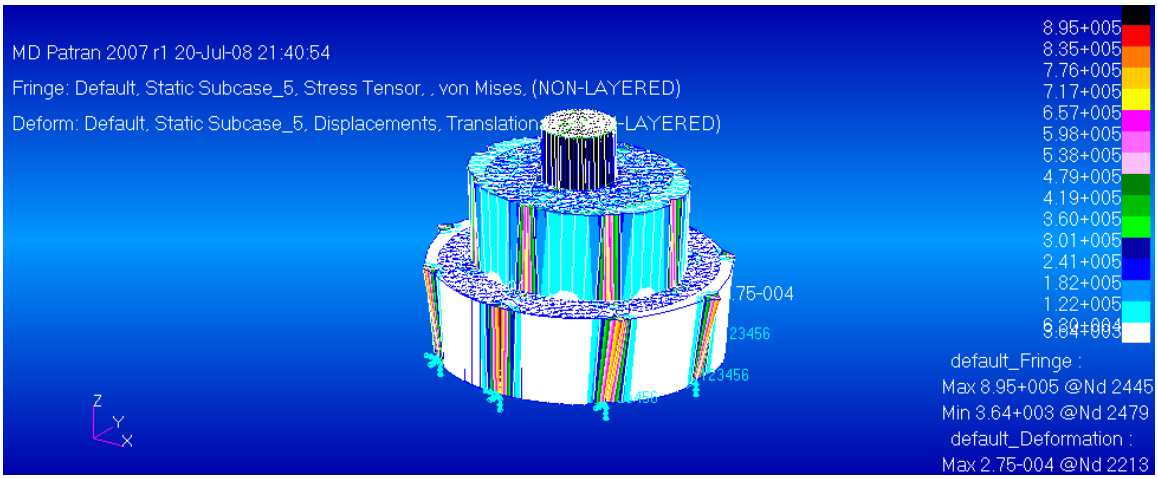

2500 rpm, 25 ipm (uncoated)

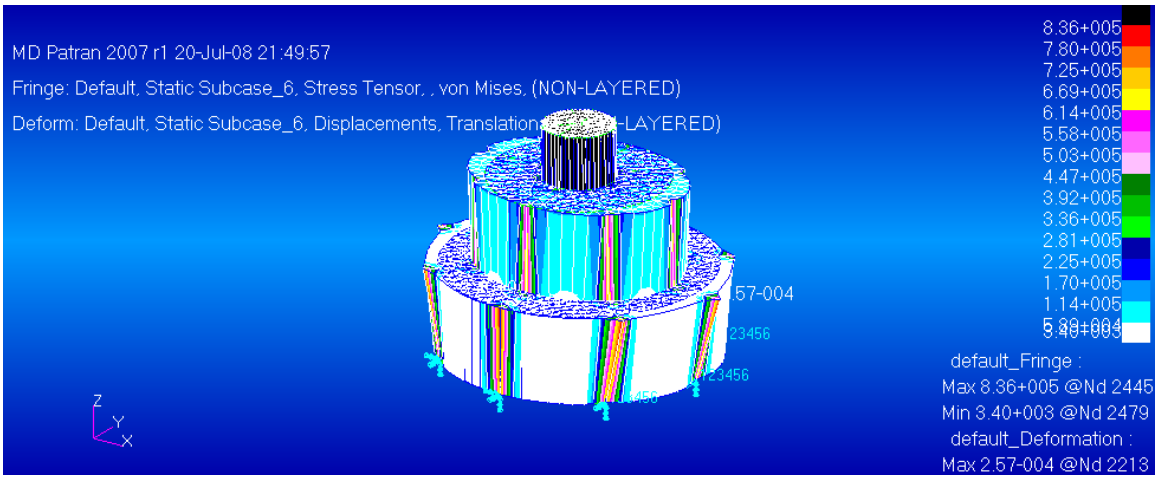

2500 rpm, 25 ipm (uncoated)

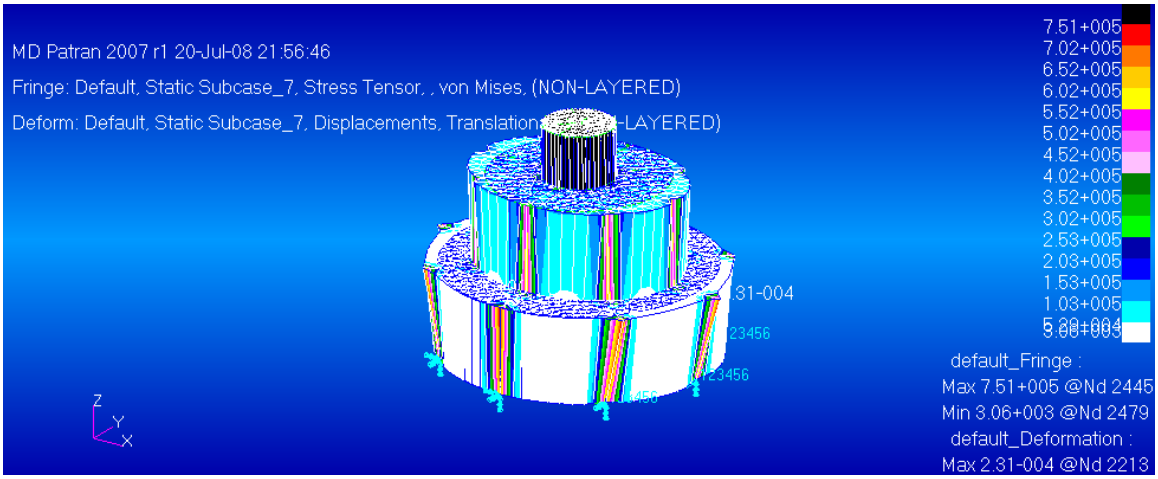

3000 rpm, 16 ipm (uncoated)

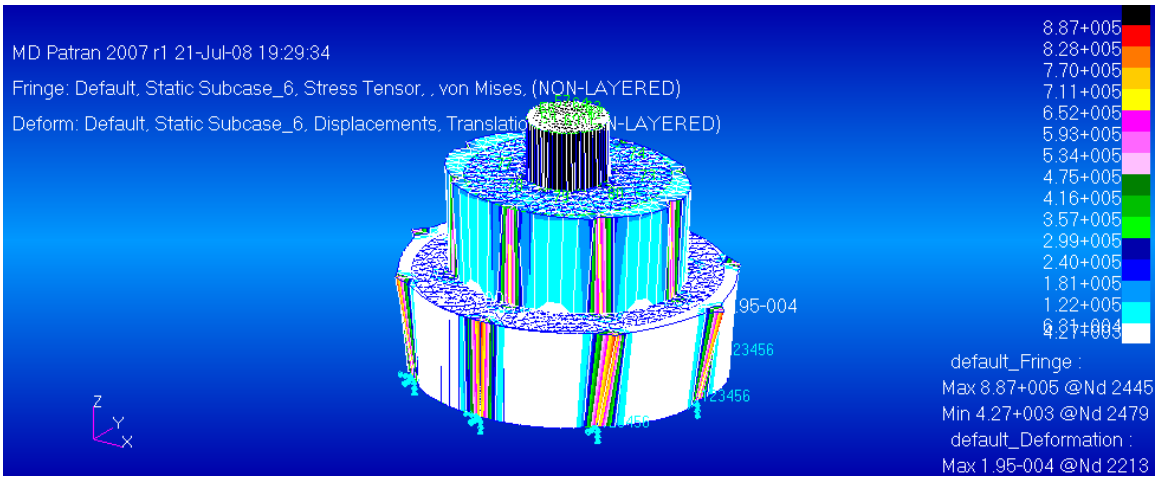

1500 rpm, 15 ipm (coated)

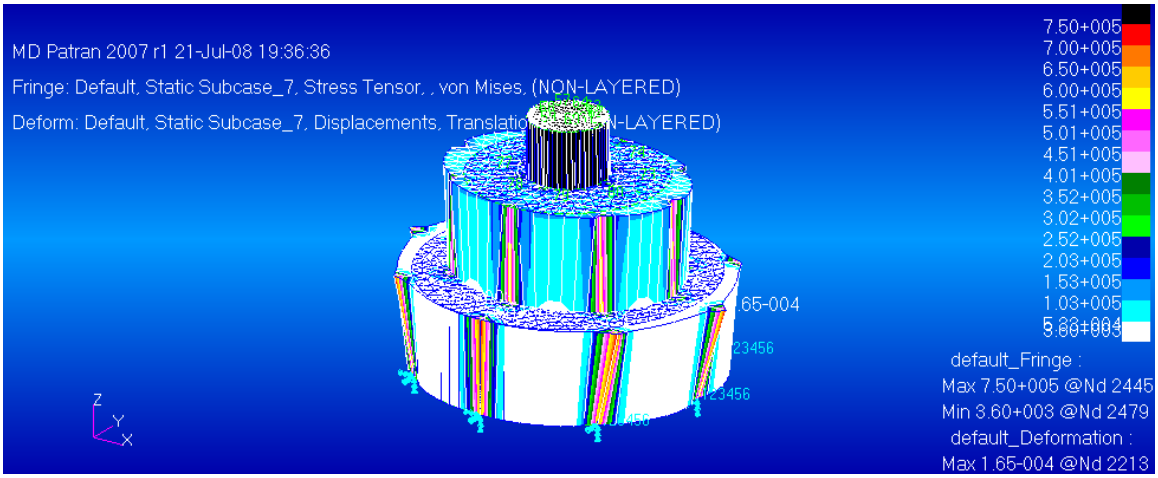

1500 rpm, 15 ipm (coated)

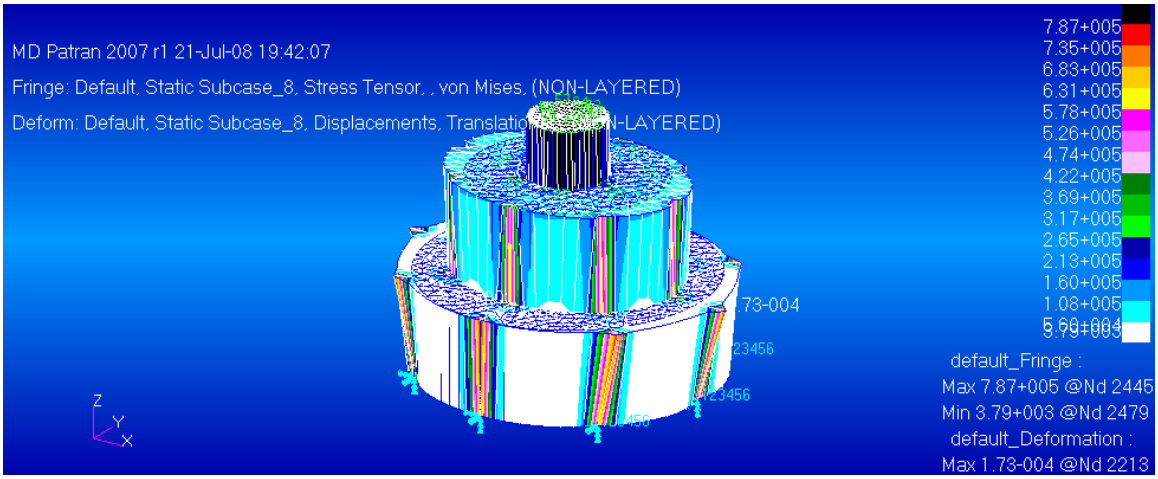

1500 rpm, 15 ipm (coated)

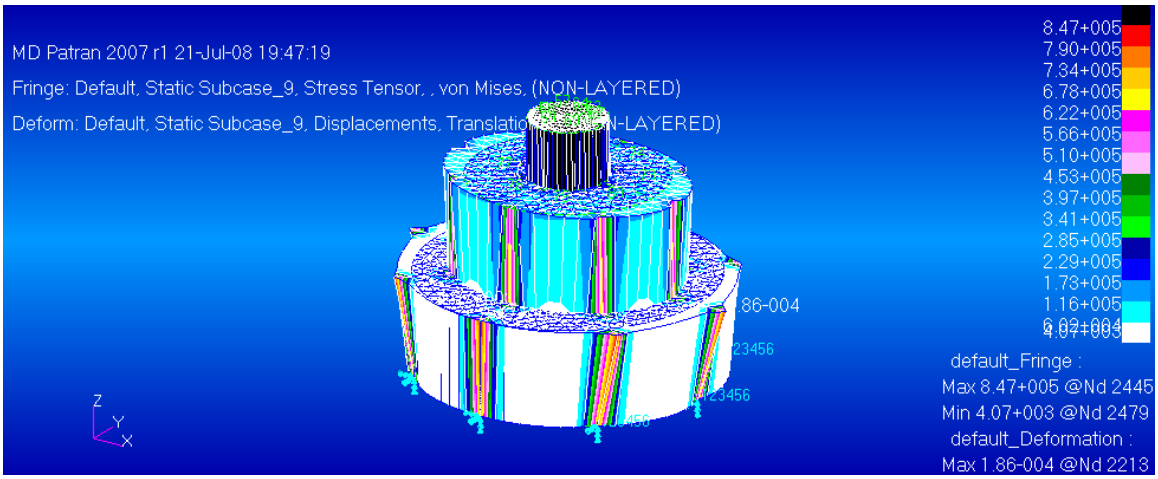

1600 rpm, 10 ipm (coated)

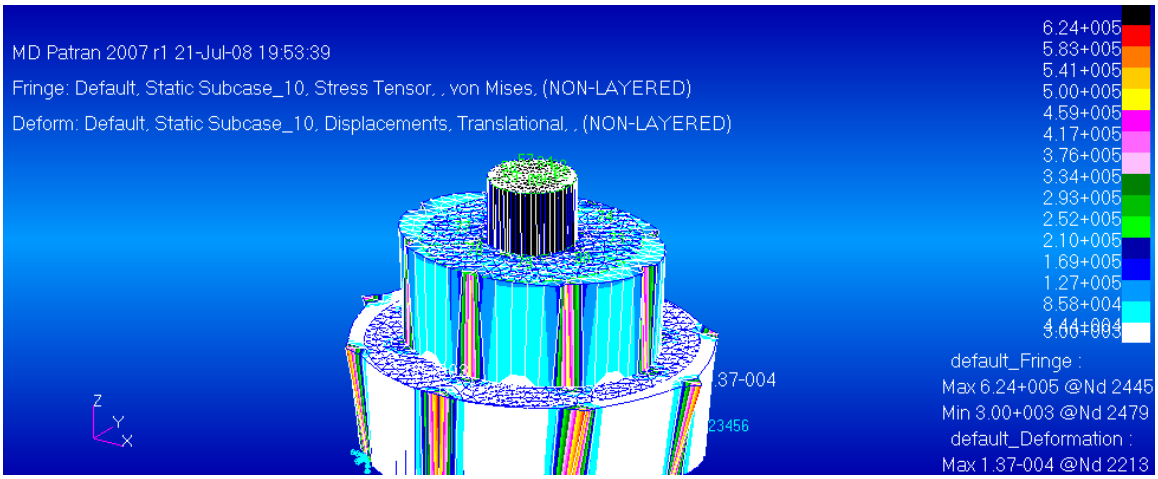

1900 rpm, 10 ipm (coated)

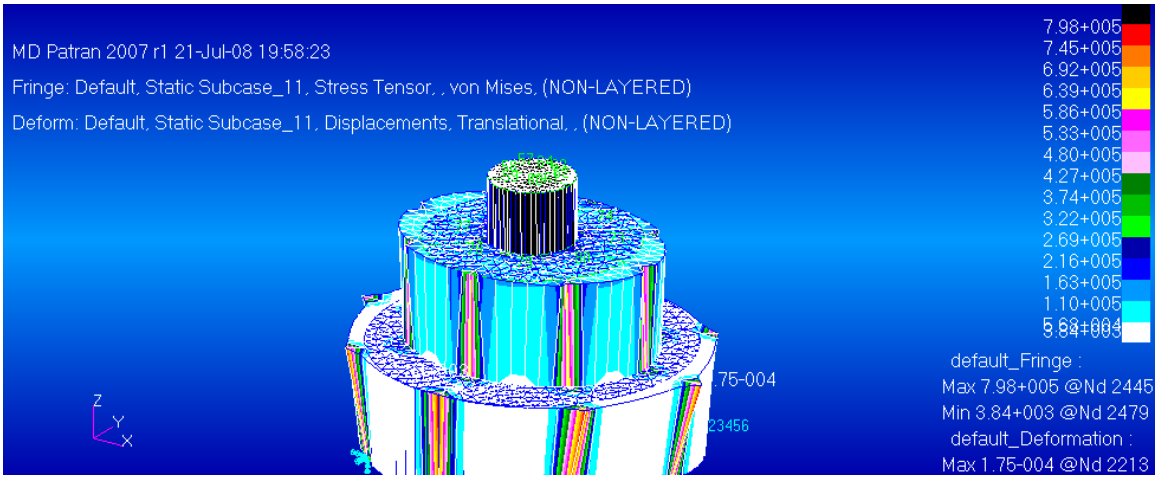

2000 rpm, 15 ipm (coated)

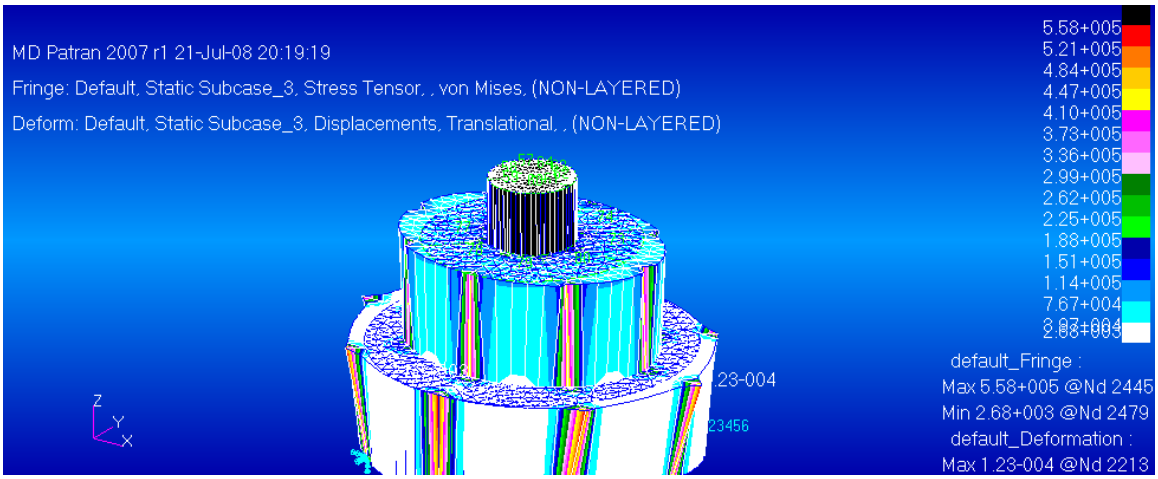

2000 rpm, 16 ipm (coated)

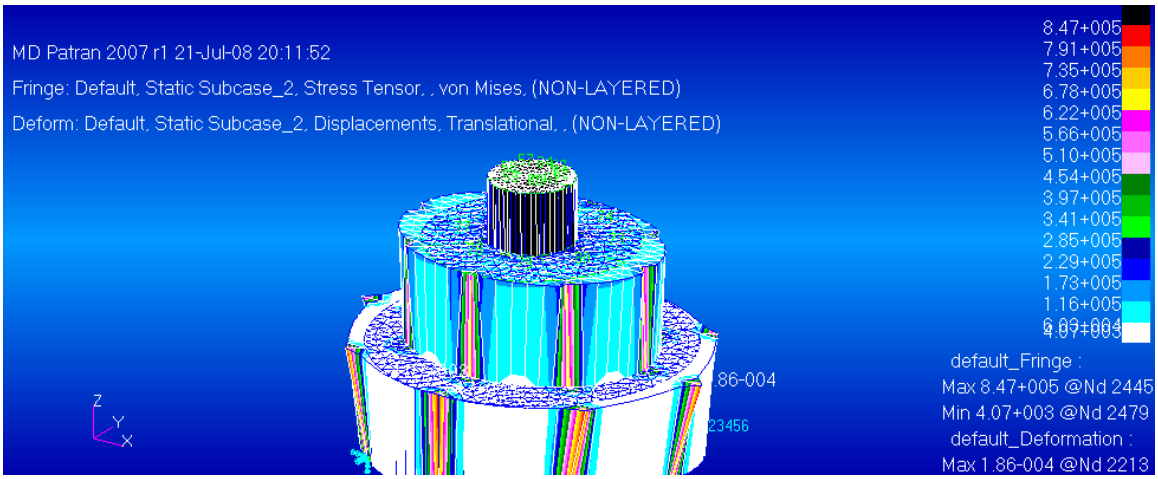

2000 rpm, 20 ipm (coated)

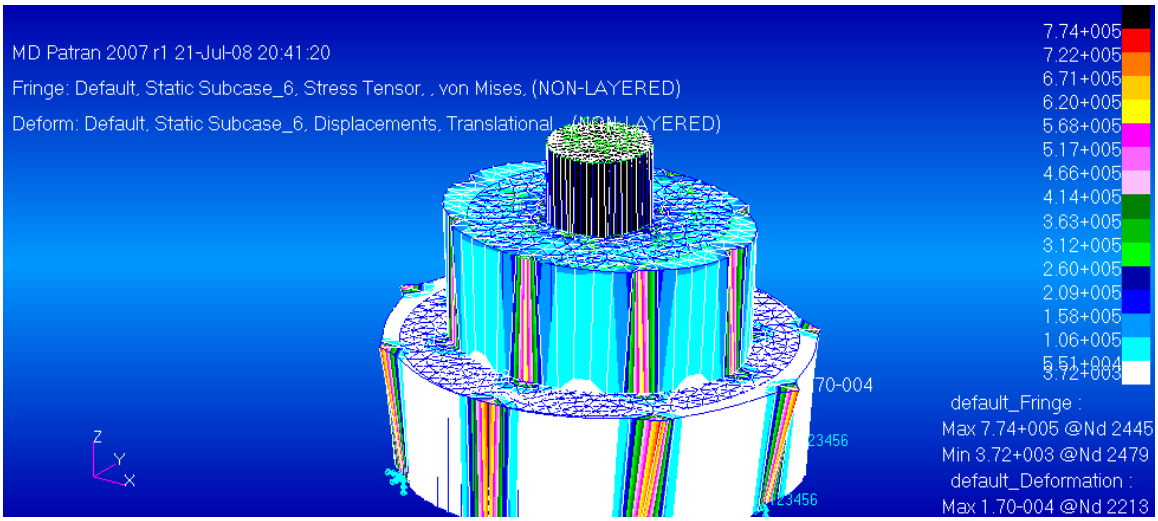

2000 rpm, 20 ipm (coated)

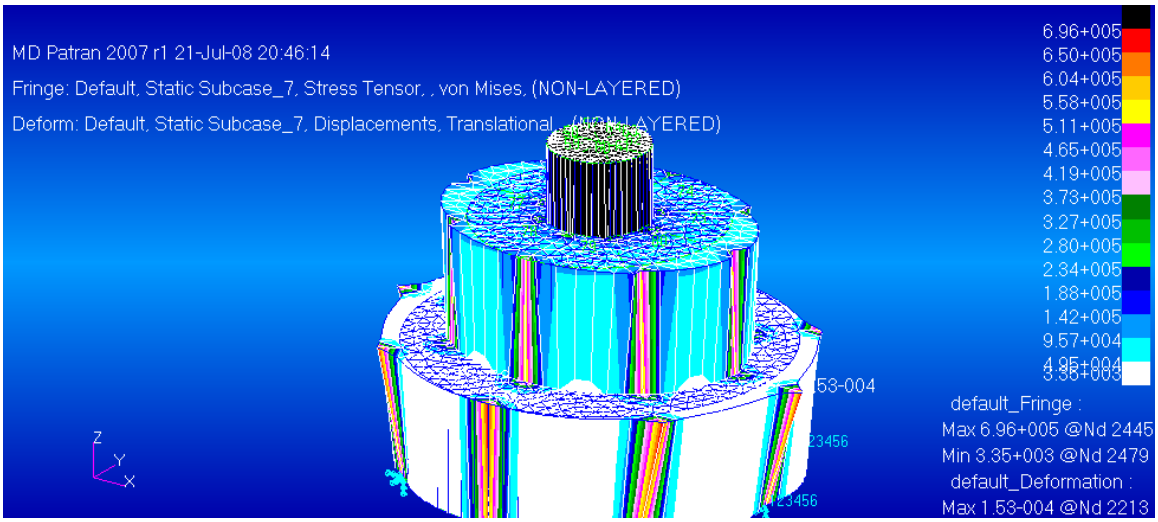

2000 rpm, 20 ipm (coated)

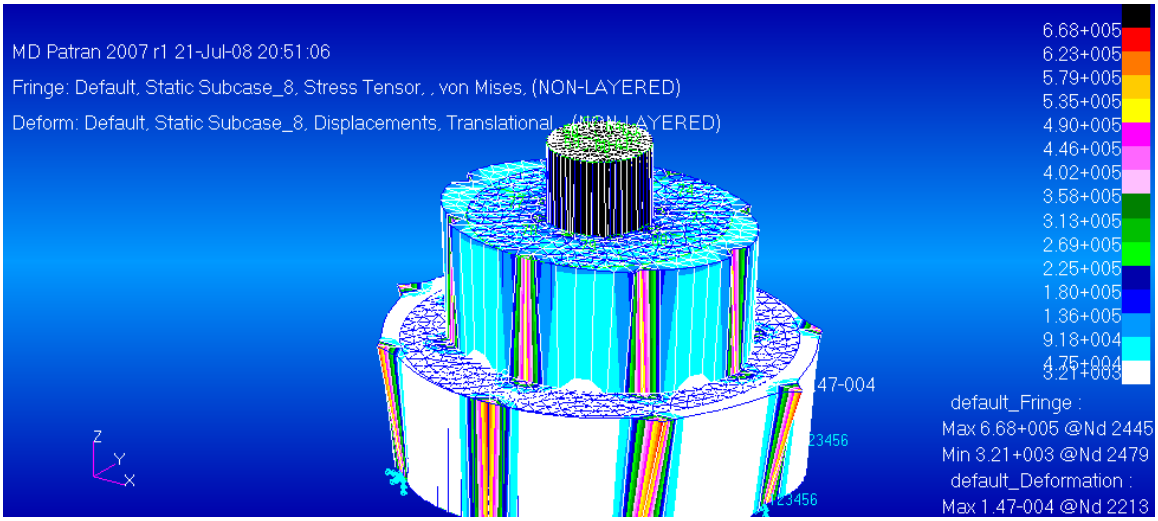

2100 rpm, 10 ipm (coated)

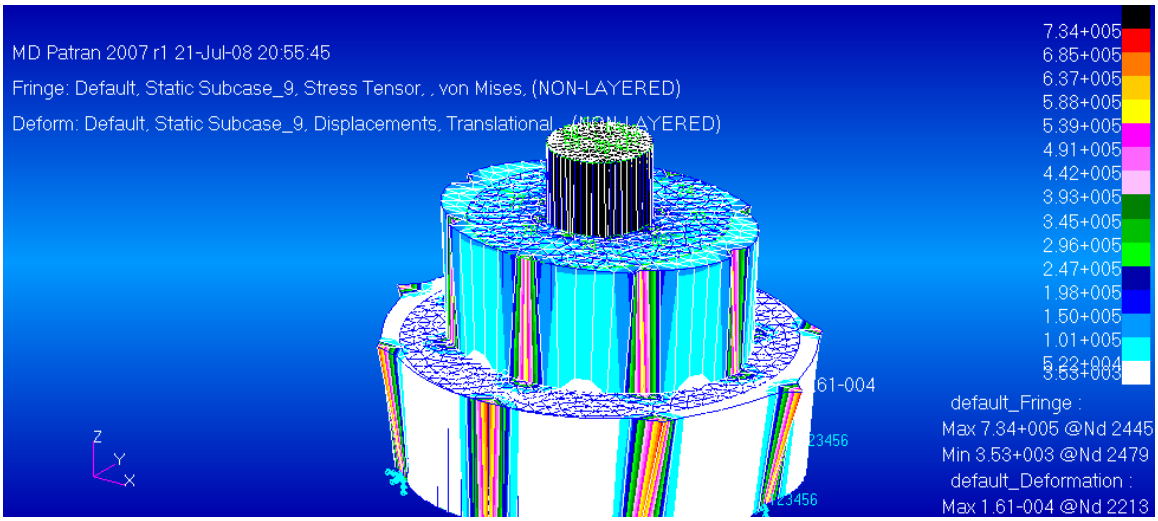

2500 rpm, 15 ipm (coated)

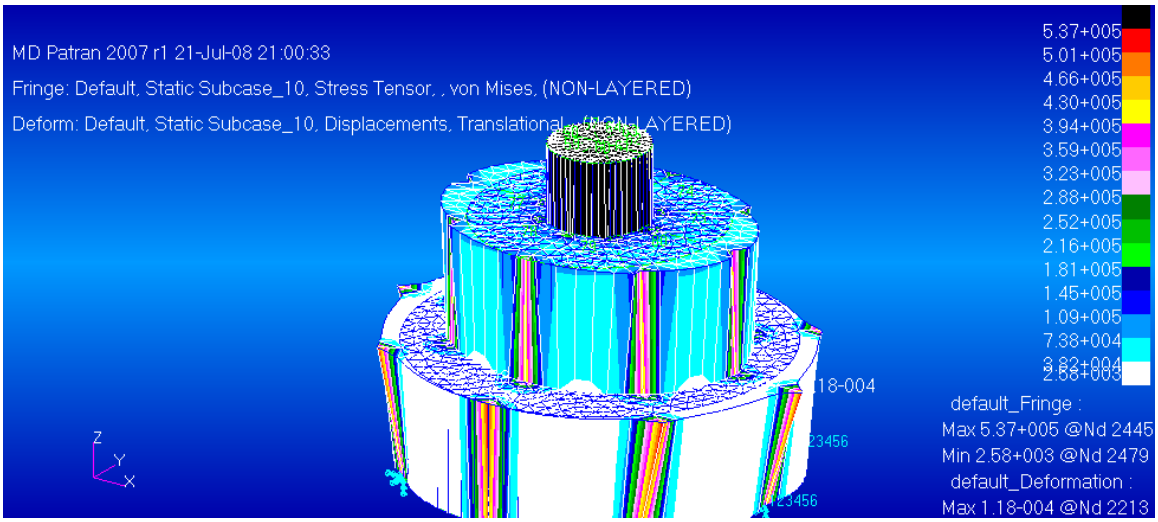

2500 rpm, 16 ipm (coated)

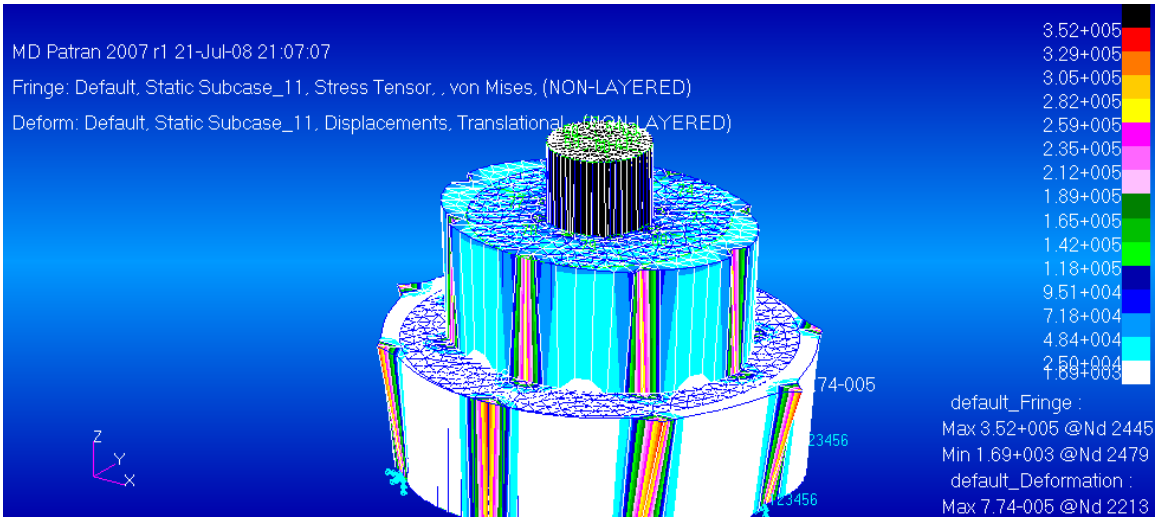

2500 rpm, 25 ipm (coated)

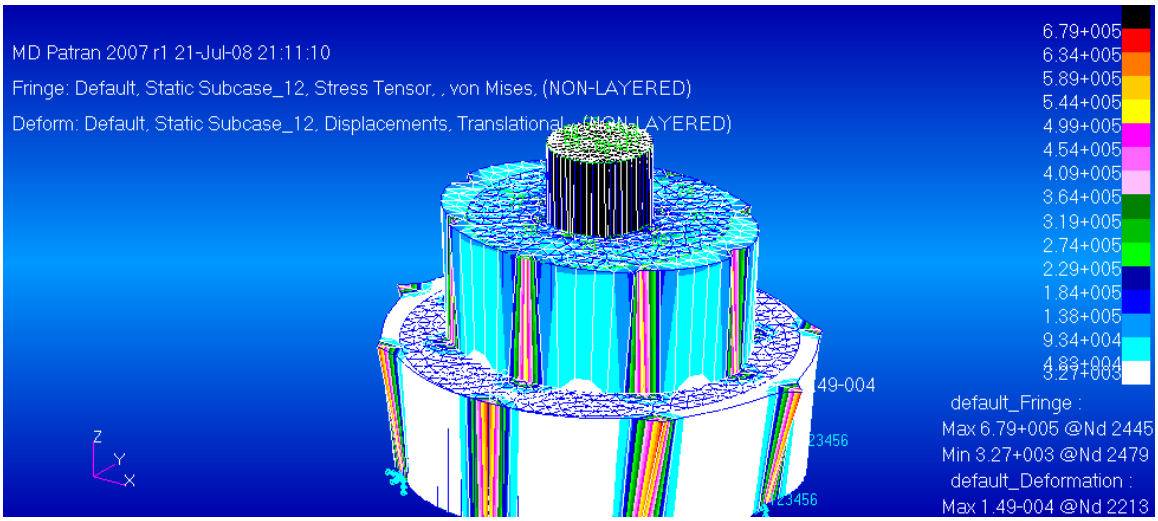

3000 rpm, 15 ipm (coated)

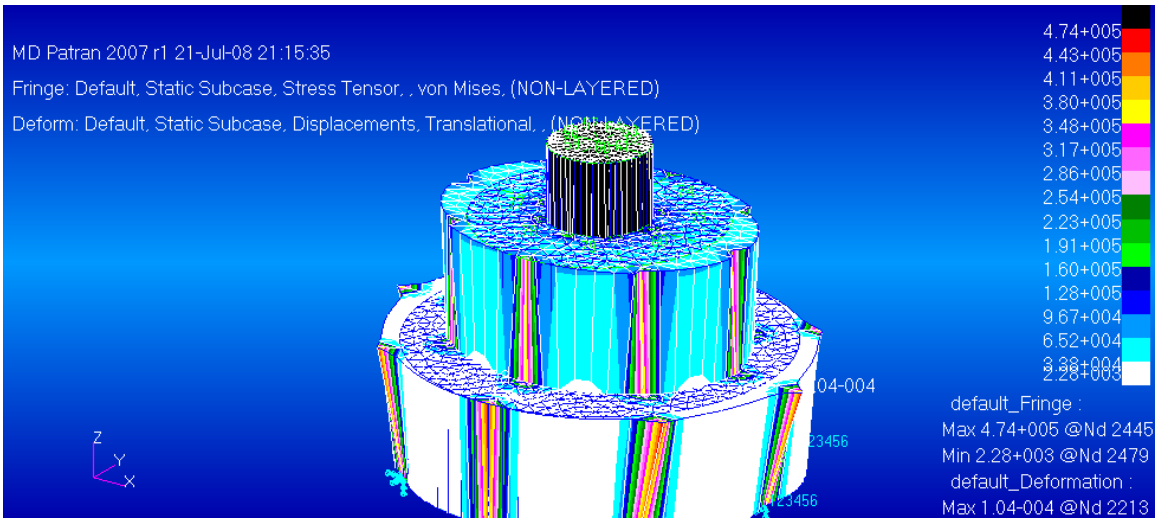

3000 rpm, 16 ipm (coated)

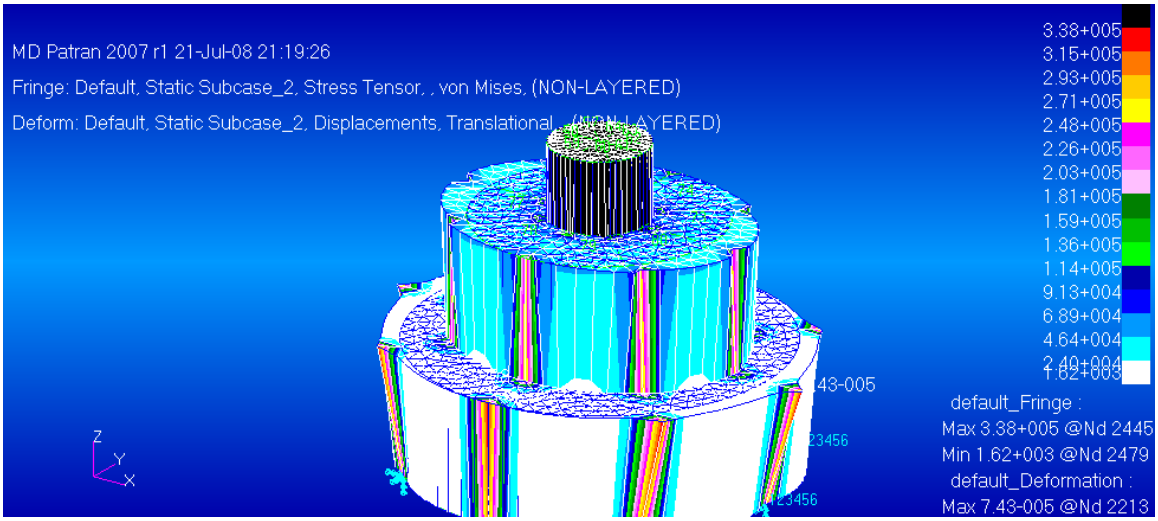

3000 rpm, 30 ipm (coated)

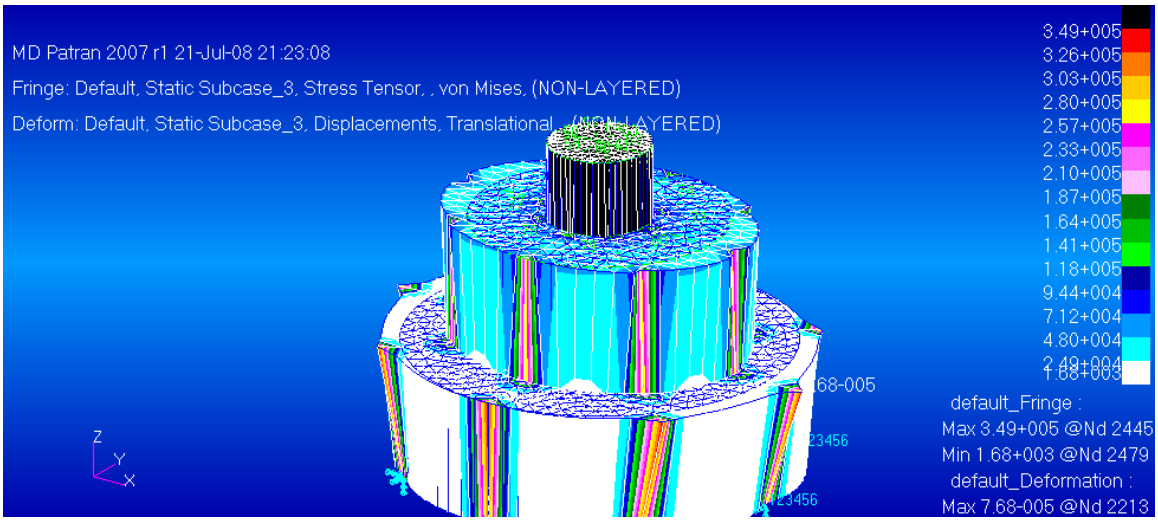

3000 rpm, 30 ipm (coated)

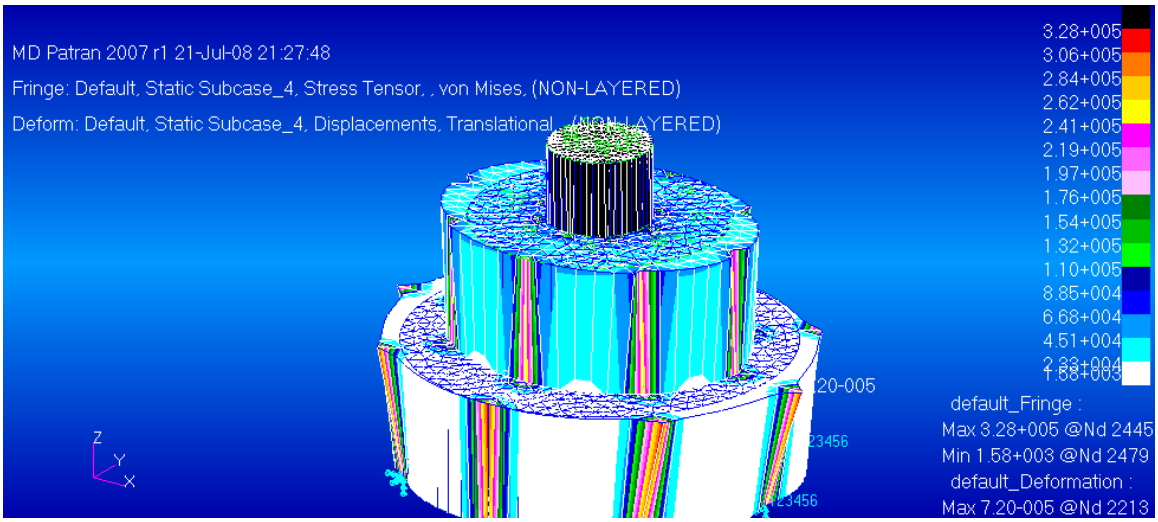

3000 rpm, 30 ipm (coated)

REFERENCES

1. W.M. Thomas, E.D. Nicholas, J.C. Needham, M.G. Murch, P. Templesmith, C.J. Dawes, G.B. Patent Application No. 9125978.8 December 1991.

2. Mishra, R.S. and Z.Y. Ma. "Friction Stir Welding and Processing." Materials Science and Engineering: Research Reports 50 (2005): 1-78.

3. Stahl, Aaron L. "Experimental measurements of longitudinal load distributions on friction stir weld pin tools." Diss. Brigham Young University, n.d.

4. MatWeb Material Property Data. 2008. MatWeb. 9 January 2008 <http://www.matweb.com>.

5. Stellwag, W.L. and T.J. Lienert. EWI. Friction Stir Welding of Aluminum Metal Matrix Composites Progress Report. Columbus: 2001.

6. T.W. Nelson, H. Zhang and T. Haynes. Proceedings of the Second Symposium on Friction Stir Welding. Gothenburg, Sweden: June 2000.

7. Kittel, C. Introduction to Solid State Physics. New York: Wiley, 1986.

8. Kohn, E., W. Ebert and C. Wile. "Electronic devices on CVD diamond." Low-pressure Synthetic Diamond. Manufacturing and Applications B (1998): 384.

9. Davidson, Jim. "Re: Diamond Coating." E-mail to the author. 29 Oct. 2006.

10. Deryagin, B.V. and D.V. Fedosayev. "The Growth of diamond and graphite from the gas phase." Surface and Coatings Technology 38 (1989): 131-248.

11. Liu, Hiumin and David S. Dandy. "Studies on nucleation process in diamond CVD: an overview of recent developments." Diamond and Related Materials 4 (1995): 1173-1188.

12. Davidson, Jim. "Diamond background." E-mail to the author. 11 January 2008.

13. Lienert, Tom. Personal Communication. 9 February 2007.

14. Uzun, Huseyin. "Friction Stir Welding of SiC particulate reinforced AA2124 aluminum alloy matrix composite." Materials and Design 28 (2007): 1440-1446.

15. Storjohann, D., O.M. Barabash, S.S. Babu and S.A. David, et. al. "Fusion and Friction Stir Welding of Aluminum Metal Matrix Composites." Metallurgical and Materials Transactions: A: Physical Metallurgy and Materials Science 36A (2005): 3237-3247.

16. Dahotre, N.B., M.H. McCay, T.D. McCay, S. Gopinathan and L.F. Allard. "Pulse laser processing of a SiC/Al alloy metal matrix composite." Journal of Materials Research 6 (1991): 514-29.

17. Lee, J.A., R.W. Carter and J. Ding. National Aeronautics and Space Administration. Friction Stir Welding of Aluminum Metal Matrix Composites (MSFC Center Director's Discretionary Fund Final Report, Project No. 98-09). Washington: GPO, 1998.

18. Diwan, Ravinder. National Aeronautics and Space Administration. Investigation of Friction Stir Welding of Al Metal Matrix Composite Materials. Huntsville, AL: 2002.

19. Marzoli, L.M., A.V. Strombeck, J.F. Dos Santos, C. Gambaro and L.M. Volpone. "Friction stir welding of an AA6061/Al_2O_3/20p reinforced alloy." Composites Science and Technology 66 (2006): 363-371.

20. Ceschini, L., I. Boromei, G. Minak, A. Morri and F. Tarterini. "Microstructure, tensile and fatigue properties of AA6061/20 vol.% Al_2O_{3p} friction stir welded joints." Composites Part A: Applied Science and Manufacturing 38 (2007): 1200-1210.

21. Cavaliere, P., E. Cerri, L. Marzoli and J. Dos Santos. "Friction stir welding of ceramic particle reinforced Aluminium based metal matrix composites." Applied Composite Materials 11 (2004): 247-258.

22. Feng, A.H., B.L. Xiao, Z.Y. Ma. "Effect of microstructural evolution on mechanical properties of friction stir welded AA2009/SiCp composite." Composites Science and Technology (2008).

23. Humphreys, F.J. and M. Hatherly. Recrystallization and related annealing phenomena. Pergamon, 1996.

24. Klug, H.P. and L.E. Alexander. X-ray diffraction procedures for polycrystalline and amorphous materials. New York: Wiley, 1974.

25. Fernandez, G.J. and L.E. Murr. "Characterization of tool wear and weld optimization in the friction-stir welding of cast aluminum 359+20% SiC metal matrix composite." Materials Characterization 52 (2004): 65-75.

26. Prado, R.A., L.E. Murr, K.F. Soto and J.C. McClure. "Self-optimization in tool wear for friction-stir welding of Al 6061+20% Al_2O_3 MMC." Materials Science and Engineering 349 (2003): 156-165.

27. Crawford, Reginald. "A Mechanistic Study of the Friction Stir Welding Process." Diss. Vanderbilt University, August 2006.

28. Roy, G.G., R. Nandan, and T. DebRoy. "Dimensionless correlation to estimate peak temperature during friction stir welding." Science and Technology of Welding and Joining 11 (2006): 606-608.

29. Lee, S.-Tong, Zhangda Lin, and Xin Jiang. "CVD Diamond Films: nucleation and growth." Materials Science and Engineering 25 (1999): 123-154.

30. Davidson, Jim. Personal Communication. 2 July 2008.

31. Mills, K.C. Recommended Values of Thermophysical Properties for Commercial Alloys, Cambridge, UK: 2002.

32. Davidson, Jim. "Thermal conductivity of diamond." E-mail to the author. 8 July 2008.

33. Shercliff, H.R. and P.A. Colegrove. "Development of Trivex friction stir welding tool part I: two-dimensional flow modelling and experimental validation." Science and Technology of Welding and Joining 9 (2004): 345-351.

34. Logan, Daryl L. A First Course in the Finite Element Method. Toronto: Thomson, 2007.

35. Klein, Claude A. and Gregory F. Cardinale. "Young's Modulus and Poisson's Ratio of CVD Diamond." Proceedings of the SPIE. San Diego, CA: July 1992.